Physics-based satellite-derived bathymetry for nearshore coastal waters in North America

by

Christopher Ilori

MSc (Natural Resources), University of Greenwich, 2012
BSc (Geography), Obafemi Awolowo University, Nigeria, 2005

Thesis Submitted in Partial Fulfillment of the
Requirements for the Degree of
Doctor of Philosophy

in the
Department of Geography
Faculty of Environment

SIMON FRASER UNIVERSITY
Fall 2020

Declaration of Committee

Name:	**Christopher Ilori**
Degree:	**Doctor of Philosophy (Geography)**
Thesis Title:	**Physics-based satellite-derived bathymetry for nearshore coastal waters in North America**
Committee:	**Chair:** Nadine Schuurman Professor, Geography
	Nick Hedley Supervisor Associate Professor, Geography Department of Geography
	Anders Knudby Committee Member Associate Professor, Geography Department of Geography, Environment and Geomatics University of Ottawa
	Nima Pahlevan Committee Member Chief Research Scientist NASA
	Bing Lu Examiner Assistant Professor, Geography Department of Geography
	Tiit Kutser External Examiner Research Professor Optics Department University of Tartu

Abstract

Accurate bathymetric information is fundamental to safe maritime navigation and infrastructure development in the coastal zone, but is expensive to acquire with traditional methods. Satellite-derived bathymetry (SDB) has the potential to produce bathymetric maps at dramatically reduced cost per unit area and physics-based radiative transfer model inversion methods have been developed for this purpose. This thesis demonstrates the potential of physics-based SDB in North American coastal waters. First the utility of Landsat-8 data for SDB in Canadian waters was demonstrated. Given the need for precise atmospheric correction (AC) for deriving robust ocean color products such as bathymetry, the performances of different AC algorithms were then evaluated to determine the most appropriate AC algorithm for deriving ocean colour products such as bathymetry. Subsequently, an approach to minimize AC error was demonstrated for SDB in a coastal environment in Florida Keys, USA. Finally, an ensemble approach based on multiple images, with acquisitions ranging from optimal to sub-optimal conditions, was demonstrated. Based on the findings of this thesis, it was concluded that: (1) Landsat-8 data hold great promise for physics-based SDB in coastal environments, (2) the problem posed by imprecise AC can be minimized by assessing and quantifying bias as a function of environmental factors, and then removing that bias in the atmospherically corrected images, from which bathymetry is estimated, and (3) an ensemble approach to SDB can produce results that are very similar to those obtained with the best individual image, but can be used to reduce time spent on pre-screening and filtering of scenes.

Keywords: satellite-derived bathymetry; physics-based models; atmospheric correction; Landsat 8

Acknowledgements

I would like to first thank my supervisory committee members. It is a great honour to work under your supervision. The suggestions you all provided enriched my research and I have no words to describe how thankful I am. I particularly thank Dr. Anders Knudby for all his understanding, advice, and effort throughout my PhD journey. I cannot express how grateful I am for his patience for my endless questions and his support in trying to make my own steps in the world of remote sensing. A big thank you to Dr. Nima Pahlevan for his support, valuable inputs and constructive feedback. I also thank Prof. Nick Hedley for accepting to be my senior supervisor and overseeing my progress.

I am very grateful to Simon Fraser University and the Department of Geography for nominating me for the Trudeau and Vanier awards, and providing me with the opportunity to obtain several teaching assistantships including graduate fellowships, as well as the opportunity to obtain several scholarships including Simons Foundation Graduate Award, Canadian Pacific/Teck Resources Award for Environmental Innovation (twice), Coastal Zone Award for Graduate Students, Patricia Gallaugher Graduate Award and SFU Big Data Scholarship. I am also indebted to IEEE Ocean Engineering Society and the Society of Photo-Optical Instrumentation Engineers), and the United States Geospatial Intelligence Foundation (USGIF) for offering me the USGIF PhD scholarship twice. Without these supports, it would have been very difficult to survive a graduate school in Vancouver.

Finally, I thank my dear wife, Monisola, and my adorable sons, Eden and Zion, for their understanding, patience and unflinching support. Thank you for putting up with the late nights, the sleepless nights, and the weekends of work.

Table of Contents

List of Tables

List of Figures

Chapter 1. Introduction

1.1. Overview[1]

Nearshore environments provide valuable ecosystem services. They play a crucial role in sustaining global biodiversity and mitigate the impact of storms, floods and wave damage for people living in coastal regions. Understanding the processes and properties of these environment is thus important. For example, bathymetric estimates from satellite data can assist in flood management and planning, resource management and recreation [1]. Likewise, they are valuable for defense purposes such as amphibious operations by the military [2], and useful for humanitarian operations such as rapid, targeted decision during disaster response and recovery. Bathymetric information, in the form of maps of water depth, will be necessary to achieve the United Nations Sustainable Development Goal 14 (i.e., “conserve and sustainably use the oceans, seas and marine resources for sustainable development”) [3]. As part of efforts towards the provision of bathymetric maps, and with the aim of facilitating the comprehensive mapping of the world’s entire seafloor by 2030, the Nippon Foundation and General Bathymetric Chart of the Oceans (GEBCO) both started the Seabed 2030 initiative in 2017 - when only 6% of the world’s ocean bottom had been mapped [4]. This initiative seeks to make a complete, freely available global bathymetric map available to the scientific community and the public in general; and has added about 14.5 million square kilometres of new bathymetric data, mainly derived using traditional acoustic techniques. Through this effort, approximately 20% of the world’s seafloor has now been mapped [5].

The use of optical satellite imagery represents one feasible approach for collecting data necessary to derive bathymetric information, especially in shallow coastal waters where bathymetric mapping with ship-based systems is time-consuming and hazardous. For example, Landsat 8 imagery is free and publicly available, and covers any area outside the poles every 16 days. Combined with its predecessors (Landsat 1-7), the Landsat satellites provide a near-global and more or less continuous record of the satellite imagery for the world’s land and coastal areas from 1972 to the present day. Together with this

---

[1] This section which provides an introduction to the thesis has been kept brief as it has been introduced in greater depth in Chapters 2 and 4.

data source, recent advances in bathymetric data processing methods - such as those that use satellite images to extract bathymetry from (1) ocean wave velocity (wave kinematic bathymetry; WKB) [6], (2) stereo images (satellite-derived photogrammetric bathymetry; SPB) [7] and (3) spectral reflectance of water (satellite-derived bathymetry; SDB) [8,9,10,11]- now offers great promise to fill gaps in existing survey data coverage, thus revolutionizing the way bathymetry is derived. These three approaches to bathymetric surveying can be used collectively or individually to help meet current information needs in shallow coastal waters. For example, the three distinct methods can be integrated in a way that leverage the best features of each to address the shortcomings of the others. For example, areas of high sediment load at the mouths of rivers and lakes are unsuitable for SDB, but are well suited for WKB, as WKB does not require light penetration through water column (which underpins SDB) but relies on optical imaging of wave crests. To this end, the utility of SDB with physics-based models is demonstrated in shallow coastal waters in this thesis.

1.2. Research objective

The aim of this thesis is to explore the application of multispectral remote sensing for satellite-derived bathymetry. Specifically, the study seeks to:

(1) Examine the applicability of physics-based models for SDB in North American waters (Chapter 2).

(2) Evaluate the performances of different AC algorithms to determine which method produces the most robust remote sensing reflectance, the input from which bathymetry is estimated (Chapter 3).

(3) Demonstrate how atmospheric correction biases related to environmental factors can be minimized to improve SDB results (Chapter 4).

1.3. Thesis structure

The rest of this thesis consists of three journal articles that each addresses the objectives outlined in section 1.2. Chapter two, which was published in Canadian Journal of Remote Sensing, evaluates the potentials of Landsat 8 data for physics-based SDB in three shallow water areas in Canada. This paper, which was the first published assessment of physics-based SDB in Canada, highlights the need for precise atmospheric correction for physics-based SDB. Thus, the second paper (Chapter 3), which was published in Remote Sensing, provides an evaluation of four atmospheric correction algorithms (ARCSI: Atmospheric and Radiometric Correction of Satellite Imagery, ACOLITE: Atmospheric Correction for OLI 'lite', SeaDAS: SeaWiFS Data Analysis System and L8SRC: Landsat 8 Surface Reflectance Code) for estimating the remote sensing reflectance, the direct input into the bathymetry algorithm. In this chapter, it was revealed that biases from atmospheric correction may be related to environmental factors that are not considered sufficiently in all atmospheric correction algorithms. The third paper (Chapter 4), currently under review in Remote Sensing, then uses one of the AC algorithms recommended in the second paper to retrieve water depth estimates for an area in the Florida Keys, USA. In doing so, it also demonstrates how atmospheric correction biases related to environmental factors can be minimized to improve SDB results, and tests an ensemble approach that derives water depth based on multiple images from the study area. Chapter 5 concludes by highlighting the contribution of each paper in this thesis.

1.4. References

1. International Hydrographic Organization (IHO). 2005. Manual on Hydrography Publication M-13. Monaco: International Hydrographic Bureau.
2. Elmore, P.A.; Avera, W.E.; Harris, M.M. Use of the AN/AQS-20A tactical mine-hunting system for on-scene bathymetry data. J. Mar. Syst. 2009, 78, S425–S432.
3. United Nations. 2015. Transforming Our World: the 2030 Agenda for Sustainable Development. https://sustainabledevelopment.un.org/post2015/transformingourworld/publication (accessed June 28, 2020).
4. Wölfl, A.C., H. Snaith, S. Amirebrehimi, C.W. Devey, B. Dorschel, V. Ferrini, V.A.I. Huvenne, M. Jakobsson, J. Jencks, G. Johnston, G. Lamarche, L. Mayer, D. Millar, T.H. Pedersen, K. Picard, A. Reitz, T. Schmitt, M. Visbeck, P. Weatherall, R. Wigley. Seafloor mapping – the challenge of a truly global ocean bathymetry Frontiers in Marine Science, 6 (2019), p. 283.

5. SEABED News, 2030. https://seabed2030.gebco.net/news/gebco_2020_release.html. Accessed on (accessed July 1, 2020).
6. R. Abileah, Mapping shallow water depth from satellite, in Proceedings of the ASPRS Annual Conference, Reno, Nevada, 2006.
7. Hodúl, M.; Bird, S.; Knudby, A.; Chénier, R. Satellite derived photogrammetric bathymetry. ISPRS J. Photogramm. Remote Sens. 2018, 142, 268–277.
8. Lyzenga, D.R. 1978. Passive remote sensing techniques for mapping water depth and bottom features. *Applied Optics*, Vol. 17(No. 3): pp. 379–383.
9. Stumpf, R.P., Holderied, K., and Sinclair, M. 2003. Determination of water depth with high-resolution satellite imagery over variable bottom types. *Limnology and Oceanography*, Vol. 48(No. 1): pp. 547–556.
10. Lee, Z.P., Carder, K.L., Mobley, C.D., Steward, R.G., and Patch, J.F. 1998. Hyperspectral remote sensing for shallow waters. I. A semi- analytical model. *Applied Optics*, Vol. 37(No. 27): pp. 6329–6338. Lee Z.P., Carder, K.L., Mobley, C.D., Steward, R.G., and Patch, J.F. 1999. Hyperspectral remote sensing for shallow waters: 2. Deriving bottom depths and water properties by optimization. *Applied Optics*, Vol. 38(No. 18): pp. 3831–3843.
11. Lee Z.P., Carder, K.L., Mobley, C.D., Steward, R.G., and Patch, J.F. 1999. Hyperspectral remote sensing for shallow waters: 2. Deriving bottom depths and water properties by optimization. *Applied Optics*, Vol. 38(No. 18): pp. 3831–3843.

Chapter 2. The potential for Landsat-based Bathymetry in Canada

This chapter has been published in the Canadian Journal of Remote Sensing.

Citation details: Anders Knudby, Shahryar Khalique Ahmad & Christopher Ilori (2016). The Potential for Landsat-Based Bathymetry in Canada, Canadian Journal of Remote Sensing, 42:4, 367-378.

2.1. Abstract

Accurate bathymetric information is fundamental to safe maritime navigation and infrastructure development in the coastal zone, but it is expensive to acquire with traditional methods. Satellite-derived bathymetry has the potential to produce bathymetric maps at dramatically reduced cost per unit area. In this study, we investigate the depths to which Landsat 8 data can be used with a radiative transfer model inversion scheme to produce bathymetric maps for shallow waters in Canada. Simulation results indicate that in relatively clear waters the technique could be effective for mapping of depths up to ~ 4.5 m with ≤ ~1 m error at a 95% confidence level, although depths of up to only ~ 3 m can be similarly mapped in more turbid waters. A case study from turbid Boundary Bay, BC, indicates that imperfect derivation of above-surface remote sensing reflectance leads to greater errors in practice. Radiative transfer model inversion of Landsat 8 data allows coarse identification and preliminary bathymetric mapping of the shallowest waters in Canada, which are, at present, largely unknown outside main traffic corridors.

2.2. Introduction

Knowledge of the depth of nearshore waters is crucial for economic activity in the coastal zone, including infrastructure development, resource extraction, navigation safety, and maritime defense operations. Measurement of water depth and subsequent production of bathymetric charts is, therefore, typically a core governmental responsibility, carried out using ship-based acoustic measurements coupled with differential GPS information. Such measurements have high vertical and horizontal accuracy but are expensive and, therefore, often of very limited extent, which leads to sparse data coverage outside primary shipping corridors. In addition, survey vessel safety concerns dictate that the shallowest areas are often left unsampled. In some regions of the world, including parts of Canada, centuries-old measurements, conducted with lead-lines and georeferenced by using the navigational instruments of the time, still form the basis of current bathymetric charts [1]. In Canada, the length of the coastline, much of which is located in the Arctic Ocean, adds to the challenge of producing accurate and up-to-date bathymetric information for national nearshore waters. In the Canadian Arctic, only 1% of waters have been mapped to modern standards, and resources to expand this coverage are limited [2]. Especially in the context of increased shipping in the Arctic, there is an urgent need for innovative technologies to increase the efficiency and coverage of bathymetric mapping in Canada.

One promising technology is satellite-derived bathymetry (SDB) based on inversion of radiative transfer models (RTMs) using passive optical remote sensing data. Pioneered by Lee et al. (1998, 1999) [3,4], the approach relies on a physics-based RTM to calculate the spectral reflectance of an aquatic environment, with specified optical properties for the water surface, water column, and seafloor at a given water depth, and sun-surface geometry. The model is run in forward mode for a range of parameter combinations and is then inverted by finding the parameter combination that produces the closest match to the spectrum observed in each pixel. In addition to producing an estimate of water depth, this parameter combination also includes values of water optical properties (absorption and backscattering) and seafloor spectral reflectance that may be used to assess water quality and seafloor habitat. A number of existing models [4,5,6,7,8] rely on this general approach but vary in terms of the underlying RTM [9,10], the function used for mapping from parameter to spectral space, the search algorithm used for inversion, and additional algorithms used for postprocessing (e.g., [11]). An extensive multimodel comparison study [12] found that all tested models produced reasonable water depth estimates for depths reaching 10 meters–15 meters at 2 sites in Australia and the Caribbean, and that more complex models required longer processing times and generally produced more accurate water depth estimates. Model differences varied between environments and datasets, and no single model was universally preferable. Although the utility of this approach has, thus, been demonstrated, most results reported in the scientific literature have been produced with airborne hyperspectral data acquired over clear tropical waters. This combination of data and environment represents a best-case scenario, but the potential for RTM-based SDB in more turbid waters, and using freely available multispectral satellite data, remains poorly explored. The use of satellite data necessitates accurate atmospheric correction [13], known to be a challenge for dark targets such as water surfaces [14] where the water-leaving radiance typically contributes less than 10% of the sensed signal [9]. Furthermore, multispectral sensors typically only have a few (3–5) bands in the wavelength region useful for water depth estimation, thus providing fewer parameters and less information for model inversion. Nevertheless, given the free and near-global availability of multispectral satellite data, the depths to which these data can be used to derive accurate bathymetric information is important, including for the less-than-ideal conditions represented by turbid coastal waters in many parts of the world. Simpler SDB approaches, which employ coincident water depth point measurements to calibrate an empirical model that predicts water depth on the basis of 1 or more spectral radiance or reflectance values (e.g., [15,16]), have been demonstrated for turbid waters in the Baltic [17], North America [18], and elsewhere. However, the reliance on coincident calibration data, as well as simplifying assumptions such as homogeneous water optical quality through the image, dramatically reduces the scalability of these methods and, therefore, their potential to contribute to bathymetry mapping at large spatial scales.

In this article, we provide a first assessment of the depth to which bathymetry can reliably be mapped using the RTM inversion approach with Landsat 8 data in Canada. Although Landsat 8 was not designed for bathymetry retrieval, recent studies suggest that its improved radiometric resolution (12-bit) and the addition of a coastal aerosol band allows improved bathymetry estimation compared to its predecessors [19]. We first apply a simulation approach [20] to 3 sites with varying latitude and water optical quality, in which realistic sensor-environment noise is added to forward-modeled reflectance spectra, which are then inverted to assess the influence of noise on water depth retrieval. We then present a field-validated case study from Boundary Bay, a turbid bay in southwestern British Columbia.

2.3. Data and methods

2.3.1. Simulation Experiment

A simulation experiment was used to assess the impact of sensor-environment noise on depth estimation for 3 sites in Canada: Boundary Bay (49º N, 123º W), Hudson Bay (59º N, 94º W), and Baffin Bay (72º N, 74º W). The PlanarRad RTM, a free software for modelling light in natural waters, [10] was used through the PlanarRadPy environment [21] to forward model above-surface remote sensing reflectance, Rrs(0^+), which was then convolved to the spectral response functions for Landsat 8 bands 1–4. The following data were used for the forward modeling:

1. Three seafloor reflectance spectra, representing 100% coverage of sand, *Sarcodiotheca gaudichaudii* (red algae), and *Zostera marina* (seagrass), were sampled in Boundary Bay according to protocols outlined by Roelfsema et al. (2006) [22]. An Ocean Optics Jaz spectrometer in an underwater housing was used to measure 40 samples of each seafloor type. Visual outliers were removed, after which the median spectrum was used to represent each seafloor type. The resulting spectra are shown in Figure 2.1. Seafloor reflectance spectra from Boundary Bay were also used for simulation at the other 2 sites, from which local data were unavailable.

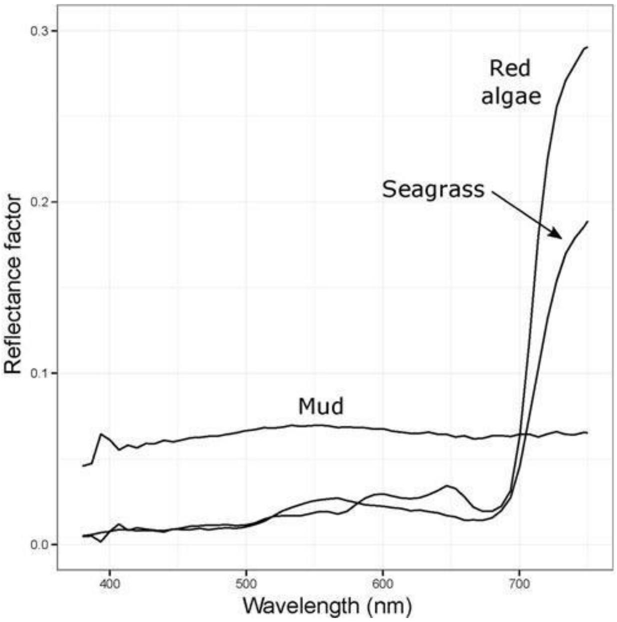

Figure 2.1. Spectra used to describe seafloor reflectance

2. Realistic water optical quality parameters P_{440}, G_{440}, and X_{550} were all assessed for each site, using Level 3 ocean color products [23] from the NPP VIIRS Generalized Inherent Optical Property (GIOP) algorithms [24,25]. Describing absorption at 440 nm due to phytoplankton, P440 was assessed from the "absorption due to phytoplankton at 443 nm" product. Values were converted from 443 to 440 nm for input to PlanarRadPy, using

$$P_{440} = 1.01 * P_{443}, \qquad (2.1)$$

a linear rearrangement of the empirical model from Lee et al. (1998) [3], accurate to within 1% for all relevant values. Describing absorption at 440 nm due to Colored Dissolved Organic Matter (CDOM), G_{440} was assessed by using the "absorption due to gelbstoff and detrital material at 443 nm" product and calculated as

$$G_{440} = a_{CDOM443}/e^{(-S_* (443-440))} \text{ [4]}, \qquad (2.2)$$

where S = 0.14 and $a_{CDOM443}$ is absorption due to CDOM at 443 nm. Describing backscattering at 550 nm due to suspended particulate matter, X_{550} was assessed using the "particulate backscattering at 443 nm" product and calculated as

$$X_{550} = bbp_{443}/(550/443)^{Y} \text{ [4]} \qquad (2.3)$$

where Y = 1 and bbp_{443} is particulate backscattering at 443 nm. Ocean color products from the summers 2014 and 2015 were investigate, and typical values for good (clear) water quality days were identified for each site. To produce a range of realistic values for forward modeling, minimum and maximum values for each parameter were set at 50% and 200% of these typical values (Table 2.1).

Table 2.1. Parameter ranges used for forward modeling of above-surface diffuse surface reflectance.

Site	Min P	Max P	Min G	Max G	Min X	Max X	Min Z	Max Z
Boundary Bay	0.17	0.76	0.35	1.05	0.012	0.005	0.01	10.0
Hudson Bay	0.014	0.058	0.045	0.183	0.001	0.004	0.01	10.0
Baffin Bay	0.020	0.080	0.035	0.150	0.0015	0.006	0.01	10.0

3. Input depths (Z) ranging from 0.01 m to 10.0 m were used for forward modeling, because it was expected that deeper depths would not be detectable in Canadian waters (Table 2.1).
4. Solar zenith and azimuth angles typical for Landsat 8 image acquisitions near the summer solstice were used for Boundary Bay and Hudson Bay. In most parts of Baffin Bay, nearshore areas remain ice covered until later in the summer; as a result, we used typical values for Landsat 8 acquisitions in August for this area.

A lookup table (LUT) containing above-surface remote sensing reflectances for Landsat 8 bands 1–4 was generated by multiple runs of the PlanarRad RTM. In the interest of computational efficiency, an adaptive lookup tree (ALUT) approach was adapted from Hedley et al. (2009) [8] to determine parameter combinations that optimally cover the spectral space and, thus, minimize discretization error during model inversion with an LUT, given a number of model runs. ALUT construction began with model runs using all ($2^4 = 16$) combinations of minimum and maximum parameter values, covering the full parameter space with a 4D voxel. The parameter space was then searched for the most undersampled region, defined as the dimension in the voxel that exhibited the greatest mean Euclidian distance between spectra on opposing sides. The voxel space was then split into equal parts across that dimension by ($2^3 = 8$) additional model runs, using the voxel's mean value for the parameter in question as well as its minimum and maximum values for the other 3 parameters. The resulting 2 voxels were then searched, again to find the most undersampled region, and the voxel in which this region existed was split across the dimension with the greatest mean Euclidian distance between spectra on opposing sides. This procedure was repeated a predefined number of times (we used 1000), until sufficiently dense coverage of spectral space had been achieved. This default ALUT procedure was prone to producing few or no subdivisions of the parameter space at deep depths, as also noted by Hedley et al. (2009) [8]. To achieve more detailed subdivision of the depth (Z) parameter between 5 m and 10 m depths, we multiplied all Euclidian distances along the Z dimension by a weighting factor (we used 0.5) scaled by the mean Z value of the voxel, which resulted in greater depth detail in the 5 m–10 m range. The ALUT algorithm was run separately for each of the 3 seafloor reflectance spectra, and the results combined to produce a single LUT. The ALUT principle, as well as the difference between the default and depth-detailed versions, is illustrated in Figure 2.2.

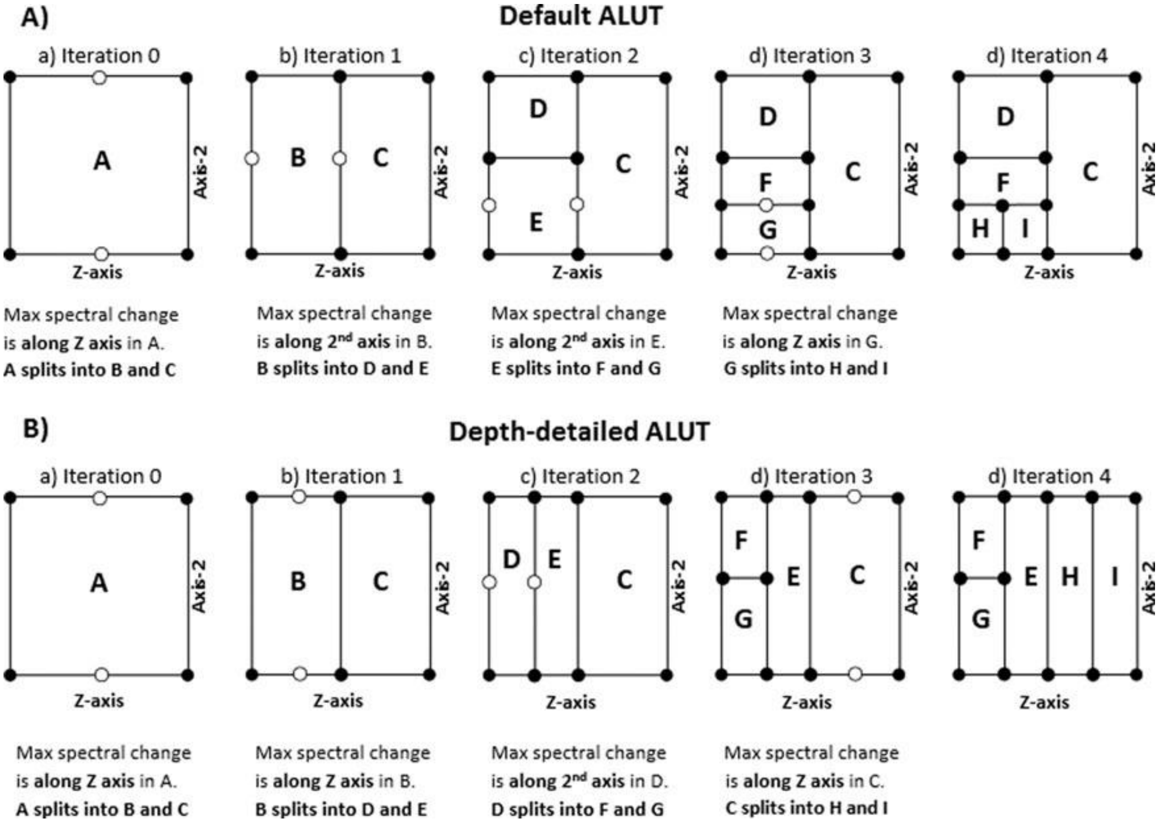

Figure 2.2. **Two-dimensional outline of the ALUT principle, and illustration of the difference between the default (A) and depthdetailed (B) versions. For a given iteration, existing forward-modeled spectra are indicated by black circles and the dimension of maximum spectral difference is indicated by hollow circles. The Z axis covers the range of depths modeled (0.01 m–10 m), and Axis-2 represents any 1 of the water quality parameters P, G, or X. Note that although the voxel is illustrated here in only 2 dimensions, 4 dimensions (Z, P, G, and X) were used in the present study.**

To evaluate the error with which the LUT can theoretically be used to derive water depth from Landsat 8 observations, the separability between forward-modeled spectra must at a minimum be related to the effect that sensor-environment noise has on the Landsat 8 measurements. To that end, the sensor environment noise equivalent perturbation of above-water diffuse reflectance, NEΔR(0^+), was evaluated by calculating the band-wise standard deviation over several homogenous deep water areas from which subsurface upward radiance could be assumed homogeneous [7,26]. For each site, 3 cloud-free Landsat 8 scenes acquired at a time with calm sea surface, clear water, and negligible sun glint were identified, de-glinted [27], and then carefully examined to produce per-band noise estimates; NEΔR(0^+) values were converted to above-surface remote sensing reflectance as per Hedley et al. (2009) [8], using the relation Rrs(0^+) =

$0.54R(0^+)/kQ$, [4] where $R(0^+)$ is the above-surface diffuse reflectance, k is a factor used to convert above-surface to below-surface diffuse reflectance, and Q = 4 is the ratio of upwelling irradiance to upwelling radiance below the water surface [28]. Whereas Hedley et al. (2009) [8] used a fixed k = 0.7 for this conversion, we noted substantial band-to-band variation in modeled k values from the PlanarRad results. Therefore, we used band-specific k values, ranging from 0.96 to 1.82, calculated as the average k value from all PlanarRad runs and resulting in the $NE\Delta R(0^+)$ values listed in Table 2.2; $NE\Delta R(0^+)$ values from each band were assumed to be normally distributed with a mean of zero and the standard deviation listed in Table 2.2. To evaluate the influence of sensor-environment noise on depth retrieval, for each forward modeled spectrum, 20 randomly sampled $NE\Delta R(0^+)$ values were added to each band to produce 20 noise-perturbed spectra, which were then inverted using the LUT Model inversion was done by using the binary space partitioning tree approach outlined by Hedley et al. (2009) [8], in which principal component analysis was used recursively to split the LUT into smaller and spectrally more homogeneous LUTs, many of which can be ignored during the search for the best spectral match for each pixel. The full LUT was initially split using a dividing plane arranged normal to the first principal component and passing through the mean value of all spectra in the LUT. Spectra on either side of the dividing plane were then aggregated into 2 new LUTs, and new splits based on new dividing planes effected for each new LUT. This process continued until a stopping criterion was met (we used LUT size ≤ 20 spectra). This recursive partitioning created a tree structure, in which each node consisted of a dividing plane with an LUT on either side, and the terminal nodes (leaves) consisted of small LUTs. For each LUT in the tree, the Euclidian distance to the dividing plane for the point closest to the plane was also calculated. During model inversion, this tree structure was searched by determining on which side of each dividing plane the spectrum to match was located, proceeding down the associated branch until either a terminal node was reached or the spectrum to match was closer to the dividing plane than any of the points in the LUT. At that point, the search would step up 1 level in the tree and conduct an exhaustive search for the best spectral match. The water depth value associated with the best spectral match was then extracted and compared to the depth used to forward model that (noise-perturbed) spectrum [20]. An overview of the data and processing used in the simulation experiment is provided in Figure 2.3.

Table 2.2. NEΔRrs(0+) values (sr−1) for deep-water homogenous areas in Landsat 8 scenes. As expected, values are higher than those previously reported for CASI-2 hyperspectral imagery [7].

Site	Band 1	Band 2	Band 3	Band 4
Boundary Bay	0.000533	0.000579	0.000886	0.000452
Hudson Bay	0.000592	0.000558	0.000436	0.000252
Baffin Bay	0.000567	0.000538	0.000802	0.000334

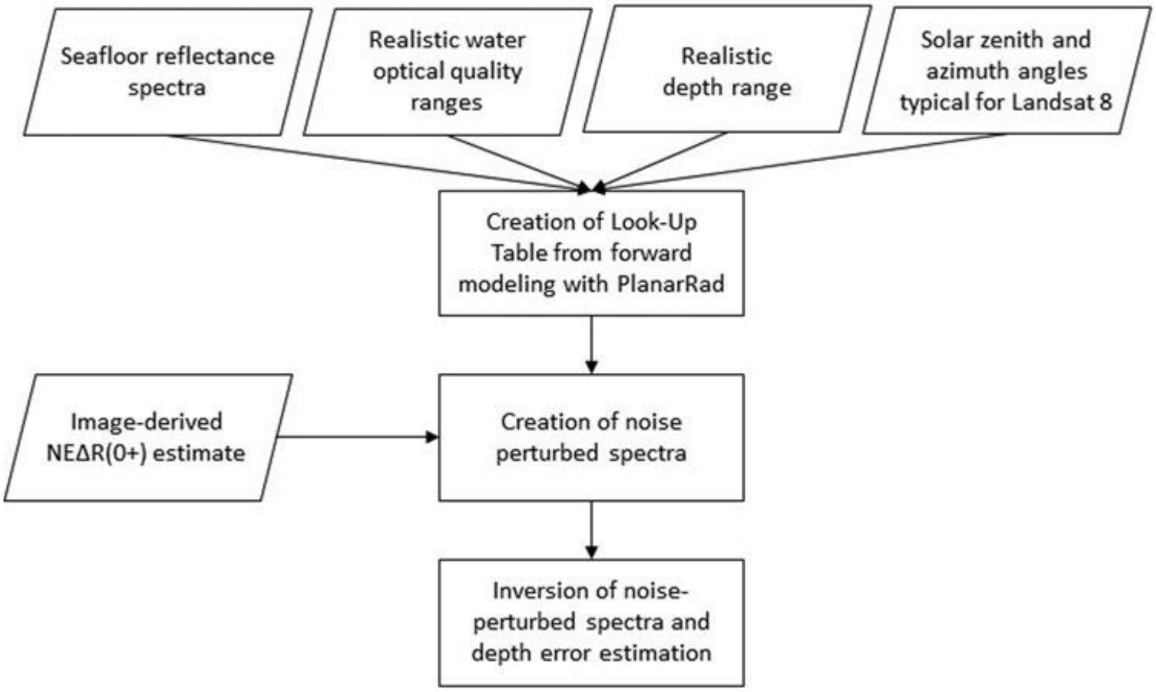

Figure 2.3. Flowchart outlining the simulation experiment.

Example application

To provide a field test of the SDB-RTM approach in Canadian waters, we applied it to a Landsat 8 image acquired June 14, 2015, for the Boundary Bay site (Figure 2.5). Forward modeling was conducted using the ALUT approach described previously, using the parameter ranges listed in Table 2.1 as well as the solar zenith angle (29.16^0) and solar azimuth angle (145.06^0) derived from the image metadata. Two approaches were tested for calibrating the Landsat data to above-surface diffuse reflectance. Initially, the L1T product was atmospherically corrected with the Py6S interface [28] to the 6S code [29] through ARCSI [30], using aerosol optical density and water vapor density measurements, from the AeroNet station on nearby Saturna Island, for parametrization of aerosol optical thickness and atmospheric water vapor content. As a simplified approach, the Landsat 8 Climate Data Record (CDR) Surface Reflectance product [31] was also tested. Although results were similar to within ~ 5% for most areas, the Landsat CDR product had visible artefacts near the water's edge (see Figure 2.4), occasionally leading to large overestimation of depths. Only those results based on the AeroNet-calibrated 6S correction were, therefore, used for further processing. After atmospheric correction, the image was de-glinted [27] and converted to above-surface remote sensing reflectance as described, and LUT inversion was carried out using the binary space partitioning tree approach to extract per-pixel depth estimates.

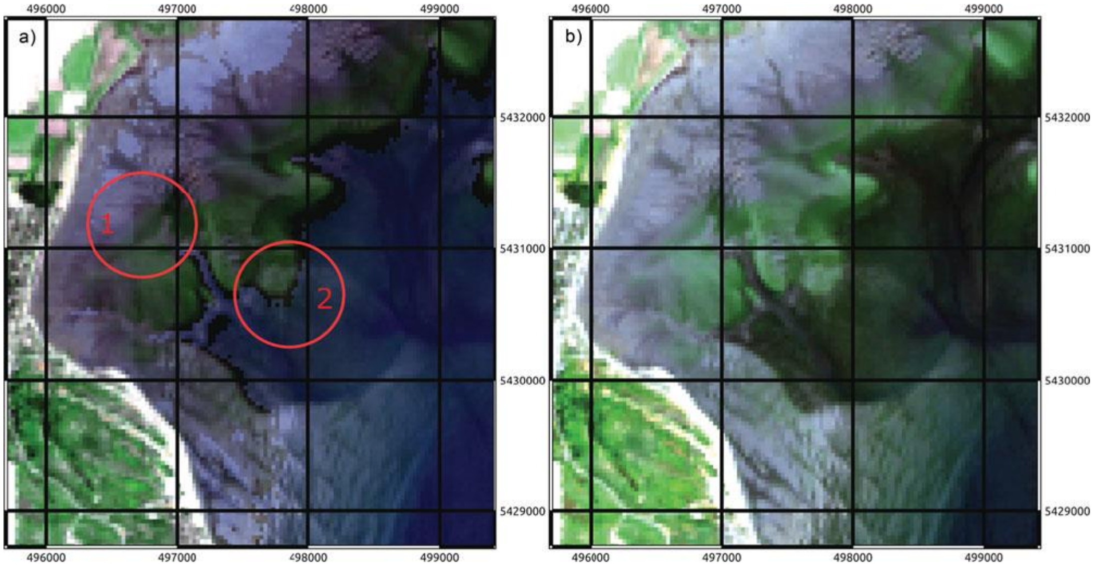

Figure 2.4. **Comparison of (a) Landsat CDR surface reflectance, and (b) surface reflectance calculated with 6S, using the AeroNet station at Saturna Island for parametrization of aerosol optical thickness and atmospheric water vapour content (right). Red circles indicate what looks like a tiling artefact, and a dark band, not present in the original data, around the edge of the seagrass beds.**

To assess the accuracy of the resulting depth estimates, 53 field validation data points were collected on August 23, 2015, from the northeastern part of the bay (Figure 2.5). Depths were measured from kayak using a lead-line, and georeferenced with a Garmin eTrex GPS. A substantial tidal range exists in the area (~ 2.0 m on both the days of image and field data acquisition). As a result, all field data were converted to water depth at the time of image acquisition, using tidal stage estimates for nearby Tsawwassen (produced by XTide; [32]), and field observations with negative water depths at the time of image acquisition were removed from the subsequent analysis.

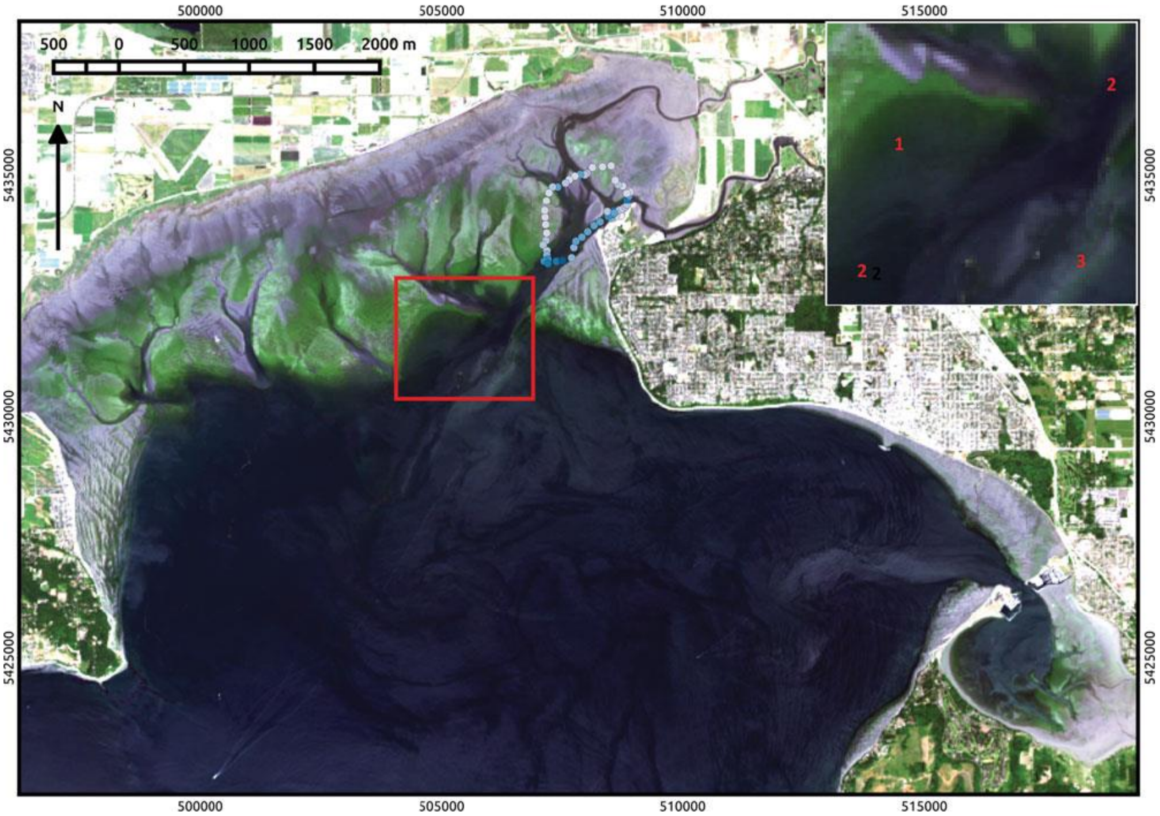

Figure 2.5. **Landsat 8 image from Boundary Bay, June 14, 2015. Locations of field observations shown in pale blue circles. The inset in the top right corner is a zoomed-in version of the area in the red box, for improved comparison with the depth estimates (Figure 2.7). Red numbers indicate, respectively, (1) a shallow seagrass slope, (2) the location of 2 relatively deep channels, and (3) a shallow sand bank at the southern edge of the channel emerging from the Nicomekl River.**

2.4. Results

The simulation results are shown in Figure 2.6 in which original depths used to forward model spectral reflectance are compared to the corresponding predicted depths derived from LUT inversion with noise-perturbed spectra. The shaded regions illustrate the loess-smoothed range between the 2.5 and 97.5 percentiles of predicted depths for a given original depth. The simulation results suggest that, with error-free estimates of per-pixel above-surface reflectance, water depths could be mapped to within 1 m until ~ 4.5 m depth and within 2 m until ~10 m depth, at a 95% confidence level, for the relatively clear waters in Hudson Bay and Baffin Bay. The poorer optical water quality in Boundary Bay increases prediction error such that water depths could similarly be mapped to within

1 m until ~ 3 m depth, and occasional input depths in the 2 m–3 m range are predicted at 10 m. Errors increase predictably at deeper depths for all sites. Note that depth predictions are limited to ≤ 10 m because this was the deepest modeled depth.

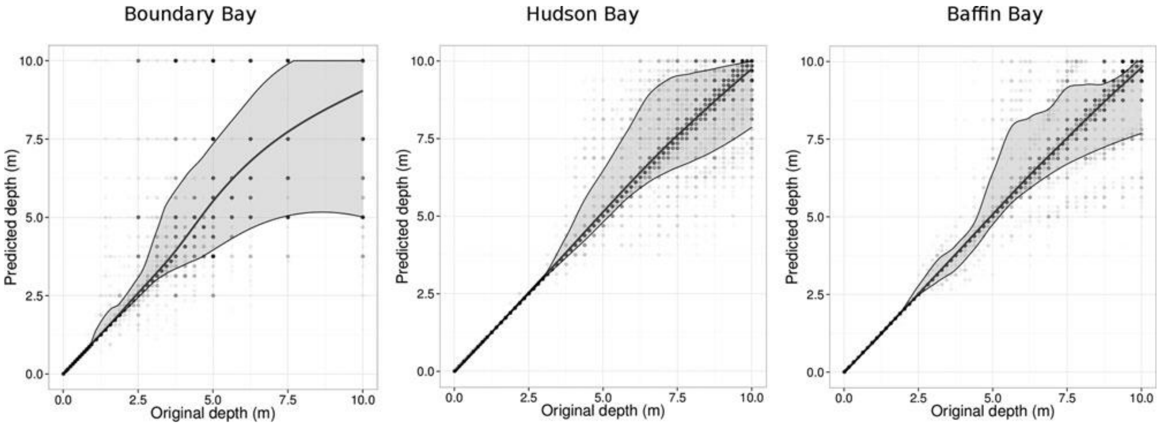

Figure 2.6. Simulation results from all 3 sites. Input depths are shown on the X axis, and depths predicted from inversion of noiseperturbed forward modeled spectra are shown on the Y axis. Overlapping points are shown in darker shades. The shaded region illustrates the loess-smoothed range between the 2.5 and 97.5 percentiles of predicted depths for a given input depth.

A comparison between the Landsat image (Figure 2.5) and the depth estimates produced from it (Figure 2.7) illustrate that shallow seafloor topography is well resolved, including the shallow seagrass slope on the left side of the inset, the locations of the deeper parts of channels, and the shallow sand bank in the bottom right of the inset (see red numbers in Figure 2.5.). Tidal channels are correctly mapped as becoming shallower toward their northern beginnings, and the central part of the bay is also correctly mapped as being deep. Note, however, that the central part of the image is optically deep, meaning that the seafloor-reflected contribution to the sensed signal is negligible. Although the area is, thus, correctly identified as “not shallow,” the actual depth cannot be estimated. The comparison between field-measured and predicted depths is shown in Figure 2.8. Of the 10 validation points in the 0 m–2 m depth range, 7 have predicted depths between 0 m and 2 m and the other 3 are predicted between ~3.75 m and 5 m. Validation points at deeper depths are consistently and sometimes severely overestimated.

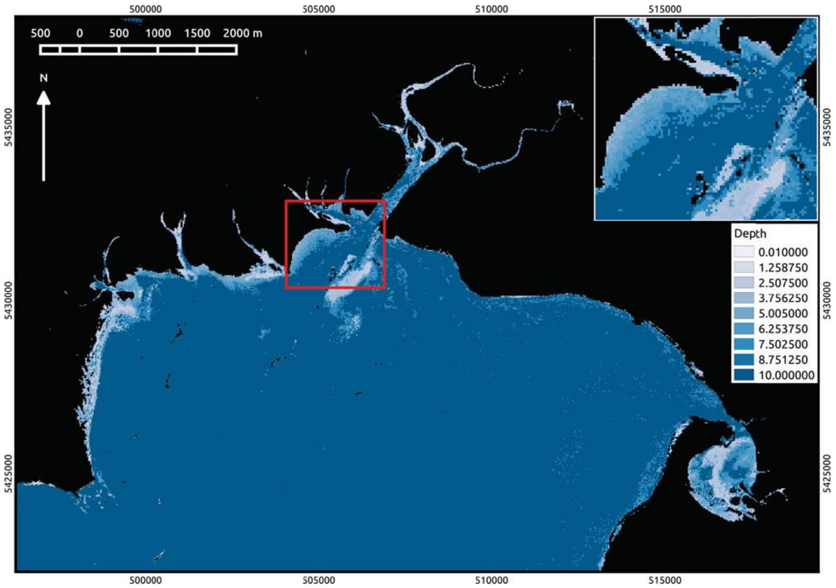

Figure 2.7. **Depth estimates for Boundary Bay. Land and other pixels with Landsat 8 band 7 diffuse reflectance > 0.10 masked in black. The inset in the top right corner is a zoomed-in version of the area in the red box, for improved comparison with the true-color composite (Figure 2.5).**

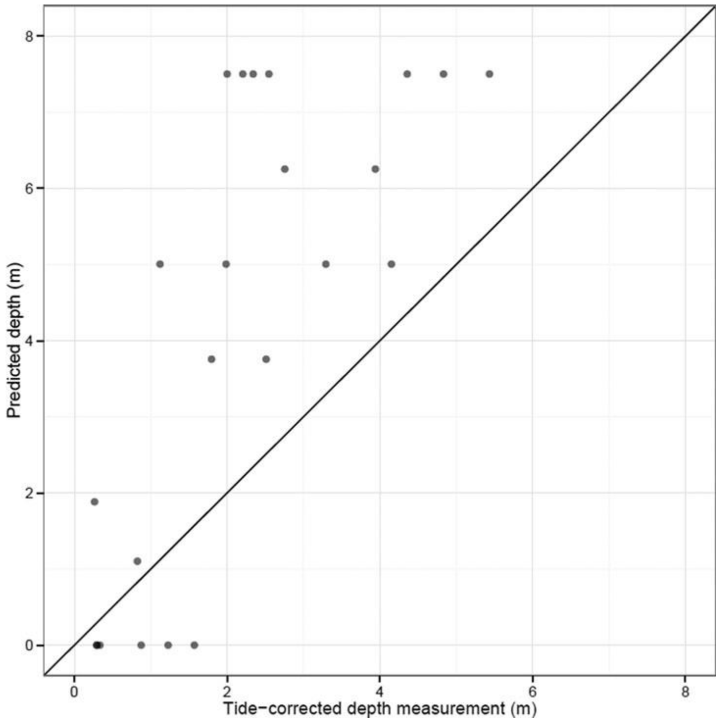

Figure 2.8. **Measured and predicted water depths from Boundary Bay, BC. Locations with water depths measured (and tide-corrected) between 0 and 2 meters are typically predicted within that range. Depths deeper than 2 meters are typically predicted in the 3.5 meter–7.5 meter range and are systematically overestimated.**

2.5. Discussion

The simulation results (Figure 2.6) are encouraging, especially for the Hudson Bay and Baffin Bay sites, where water optical quality was relatively good and sensor-environment noise reflectance equivalent NEΔR(0^+) was lower than we had expected, given the high solar zenith angles at these locations. As a result, the simulation suggests that water depths can be mapped to ~ 4.5 m with ≤ 1 m error at a 95% confidence level at these locations. Due to the poorer water optical quality in Boundary Bay, the simulation suggests that water depths can be mapped to only ~ 3 m here, with less than ≤ 1 m error at a 95% confidence level. The ~ 1 m error at a 95% confidence interval is the depth accuracy limit for an Order 2 hydrographic survey in Canada [33] and is, therefore, a relevant benchmark for satellite-derived bathymetry in Canada. Note that noise perturbation of the input spectra leads to greater overestimation than underestimation of depths, because change of $R_{rs}(0^+)$ per unit of depth decreases with increasing water depth.

It is also important to note that the simulations assume error-free per-pixel estimates of above-surface remote sensing reflectance, and that imperfect atmospheric and sun-glint correction as well as imperfect conversion from diffuse reflectance to remote sensing reflectance is likely to lead to larger actual errors. Atmospheric correction remains an issue for multispectral (and hyperspectral) data over water, and the effects on RTM inversion methods can be severe [13]. The Landsat 8 surface reflectance product has not yet been validated, and although the Landsat 5 and 7 equivalents have undergone extensive evaluation for terrestrial areas [34,35], 1 study that has specifically assessed Landsat-based surface reflectance estimates produced for water pixels showed that, although 6S outperforms other algorithms, errors are still in the order of 0.01 – 0.02 (absolute, diffuse reflectance) for Landsat 7 ETM+ bands 1–4 [14]. Given that shallow-water above-surface diffuse reflectance values around 0.03–0.05 are common for the blue/green bands and lower for the red and near-infrared bands, relative errors in that range are substantial. Because atmospheric correction for Landsat is scene based, differences in atmospheric conditions within a scene could partly be to blame [36], and per-pixel radiometric matching to more refined and better validated surface reflectance products [37,38] might represent a straightforward solution. Conversion from above-surface diffuse reflectance, which is the standard output from atmospheric correction algorithms for multispectral satellite data, to above-surface remote sensing reflectance is not straightforward, either. There is substantial difference between our band-specific k values and the fixed k value used by Hedley et al. (2009) [8], and Vahtmae and Kutser (2013) [13] used an alternative, more direct conversion of $R_{rs}(0^+) = R(0^+) / Q$, setting $Q = \pi$, while we used Q = 4. Field testing and comparison of these procedures for a range of water quality and water surface conditions is needed to evaluate their relative appropriateness.

However, the NEΔ$R(0^+)$ values we used were based on investigation of only 3 scenes, and it is reasonable to expect that real errors might be lower for some scenes, e.g., with unusually homogeneous atmospheric and sea surface conditions. Similarly, the P, G, and X values used for the simulations include some values twice as high as those typically found in the VIIRS products. For a given scene acquired on a day with exceptional water quality, actual P, G, and X values would be substantially lower, leading to improved depth estimation. It is also important to note that the 3 sites were not preselected based on high water quality; areas with better/worse optical water quality and, thus, more/less amenable to satellite-derived bathymetry are likely to exist across Canada.

A comparison between the results of the simulations and the application to the Landsat 8 image from Boundary Bay illustrates primarily the effect of imperfect estimation of above-surface remote sensing reflectance from the Landsat data. Although severe overestimation at shallow depths is very rare in the simulation results, one site with a field-measured depth of ~ 1 m had a predicted depth of 5 m, and several sites in the ~ 2 m range of measured depths had predicted depths of up to 7.5 m (Figure 2.8). Given the water optical quality in Boundary Bay, reflectance spectra may differ very little between 2 m and 7.5 m, and imperfect $R_{rs}(0^+)$ calibration of the input image can result in large depth estimation errors. However, it should also be noted that the tidal correction of the field validation data was subject to uncertainty due to the geographical context of the measurement sites. Field validation points were all measured at the extreme northeastern end of Boundary Bay, whereas the tidal correction was based on Tsawwassen, which is located only a few kilometers away but on the other side of the Point Roberts peninsula. More importantly, the estuaries of the Serpentine and Nicomekl rivers provide a direct water input to the northeastern part of the bay, thus modifying tidal influences on water depths. The deeper field validation points, which are systematically overestimated, were indeed measured in the combined subtidal channel of these rivers (Figure 2.5). Although the magnitude of these influences is unknown, they suggest that the consistent discrepancy between predicted and observed depths for the deeper points may at least partly reflect an underestimation of the tide-corrected depth measurements. In addition, 5 sites with field-measured depths between 0.2 m and 2.0 m had predicted depths of 0.01 m (Figure 2.8). Four of these sites are located over dense seagrass beds, where the long blades of *Zostera marina* were observed floating at or near the surface even at measured depths above 3 m. The high near-infrared reflectance of these floating seagrass blades is a likely cause for the underestimation of depths in these areas. Such complex 3-dimensional seafloor structure is not modeled by PlanarRad and would require improved functionality in the RTM used, as shown by Hedley et al. (2016) [39].

Nevertheless, despite the poor fit shown in Figure 2.8., the RTM inversion is generally successful at separating depths measured below and above 2 m, and the resulting depth map is generally successful at resolving shallow seafloor topography. The combination of useful and problematic results points to the necessity of per-pixel quality control, to allow users to identify areas in the map where estimated depths are relatively accurate and develop an appropriate level of confidence in the results. Brando et al. (2009) [7] developed a quality control procedure that includes per-pixel estimation of optical closure (fit between closest modeled and observed spectra) and substrate detectability (contribution of seafloor-reflected radiation to the sensed signal), and demonstrated that depth estimations were more precise in areas with good optical closure and high substrate detectability. In our case, such quality control would correctly flag the deep central part of Boundary Bay as having negligible substrate detectability and unreliable depth estimates while indicating higher reliability at shallower depths. A sediment plume seen extending south from the shallow sand bank just below the red box in Figure 2.7 is mapped as shallow water because the sediment creates a “false bottom” and represents a situation in which a different kind of quality control (e.g., using multiple images; [18]), would be needed to correctly flag depth estimates from this area as unreliable.

Although the field test results from Boundary Bay suggest that only crude separation between shallow and deep water can be reliably mapped here, as is the case for other sediment and CDOM-rich environments [17], it is important to keep in mind that water optical quality is better in most other parts of Canada and that only a single image acquired on a day with exceptional water quality is necessary to achieve deeper and more reliable depth estimation. In addition, there is potential to refine the data processing structure outlined previously in ways that may further improve the results. For example, the effect of errors in absolute radiometric calibration of the input image might be mitigated by modifying the measure of fit used for spectral matching during model inversion - we used the Euclidian distance, as is commonly done, but in the presence of spectrally correlated atmospheric correction errors, a measure of spectral shape, e.g., spectral angle, could be useful in addition or instead of the Euclidian distance [13]. Our work also used only pure seafloor spectra, whereas, in reality, all pixels in our study area contain a mix of sand and seagrass with varying but small amounts of red algae. Mixed seafloor spectra could thus be introduced [8,40] to improve the spectral matching. Another promising avenue for improvement is to exploit spatial autocorrelation in water optical quality instead of relying on per-pixel estimates. One such approach has been developed by Jay and Guillaume (2014) [11] in the form of a localized maximum likelihood estimation of both depth and water quality parameters, which showed substantial improvement over the per-pixel approach. There is also potential to substantially improve processing speed by using Lee et al.’s (1998) [3] semi-analytical model instead of conducting the PlanarRad model runs, although this model has some discrepancy with Planar-Rad outputs for bright substrates in shallow areas [20]. Finally, the availability of new free data sources might improve the precision of RTM inversion results. Sentinel-2 has a band specification similar to that of Landsat 8 but with different spatial resolution, and EnMAP will produce hyperspectral data with 30 m spatial resolution. Both have the potential to produce results superior to those possible with Landsat 8 data.

2.6. Conclusion

Through radiative transfer simulations and a field test in Boundary Bay, BC, we demonstrated that Landsat 8 has potential for mapping shallow bathymetry in Canada with a radiative transfer model inversion scheme. The field test demonstrated that reasonable separation between shallow (<2 m) and deeper (>2 m) water can be achieved even in the Bay’s relatively turbid waters, and the simulations suggest that better results can be expected for clearer waters elsewhere. Occasional severe over-estimation of water depth points to the need for per-pixel quality control, to allow users to develop appropriate confidence in the results. Given the extent of Canada’s coastline and the lack of bathymetric information for most of it, the ability to use free Landsat data to detect areas submerged in a few meters of water, without the need for coincident field measurements, has the potential to dramatically improve our knowledge of shallow seafloor topography in Canada.

2.7. References

1. CHS 2016. "Charts available through the online catalogue of the Canadian Hydrographic Service, Ottawa." Accessed January 13, 2016, http://www.charts.gc.ca/charts-cartes/paper-papier/index- eng.asp?step 1&by Catalogue List.
2. Auditor General 2014. *Marine Navigation in the Canadian Arctic*. Auditor General of Canada, Ottawa. Accessed October 17, 2015, http://www.oag-bvg.gc.ca/internet/English/att e 39878.html.
3. Lee, Z.P., Carder, K.L., Mobley, C.D., Steward, R.G., and Patch, J.F. 1998. "Hyperspectral remote sensing for shallow waters. I. A semi- analytical model." *Applied Optics*, Vol. 37(No. 27): pp. 6329–6338. Lee Z.P., Carder, K.L., Mobley, C.D., Steward, R.G., and Patch, J.F. 1999. "Hyperspectral remote sensing for shallow waters: 2. Deriving bottom depths and water properties by optimization." *Applied Optics*, Vol. 38(No. 18): pp. 3831–3843.
4. Lee Z.P., Carder, K.L., Mobley, C.D., Steward, R.G., and Patch, J.F. 1999. "Hyperspectral remote sensing for shallow waters: 2. Deriving bottom depths and water properties by optimization." *Applied Optics*, Vol. 38(No. 18): pp. 3831–3843.
5. CD Mobley, LK Sundman, CO Davis, JH Bowles, TV Downes, et al. 2005. Interpretation of hyperspectral remote-sensing imagery by spectrum matching and look-up tables Applied Optics 44 (17), 3576-3592.
6. Klonowski, W. M., Fearns, P. R. C. S., and Lynch, M. J. 2007. "Retrieving key benthic cover types and bathymetry from hyperspectral imagery." *Journal of Applied Remote Sensing*, Vol. 1(No. 011505).
7. Brando, V.E., Anstee, J.M., Wettle, M., Dekker, A.G., Phinn, S.R., and Roelfsema, C. 2009. "A physics based retrieval and quality assessment of bathymetry from suboptimal hyperspectral data." *Remote Sensing of Environment*, Vol. 113(No. 4): pp. 755–770.
8. Hedley, J., Roelfsema, C., and Phinn, S.R. 2009. "Efficient radiative transfer model inversion for remote sensing applications." *Remote Sensing of Environment*, Vol.

113(No. 11): pp. 2527–2532.

9. Mobley, C.D. 1994. *Light and Water*. San Diego, CA: Academic Press. Mobley, C.D., Sundman, L., Davis, C.O., Bowles, J.H., Downes, T. V., Leathers, R. A., Montes, M.J., et al. 2005. “Interpretation of hyperspectral remote-sensing imagery by spectrum matching and look-up tables.” *Applied Optics*, Vol. 44(No. 17): pp. 3576–3592. NASA 2010. *Ocean Level-3 Standard Mapped Image Products*. Report. Accessed April 23, 2015, http://oceancolor.gsfc.nasa.gov/cmsdocs/ technical documents/ocean level-3 smi products.pdf.
10. Hedley, J. 2008. “A three-dimensional radiative transfer model for shallow water environments.” *Optics Express*, Vol. 16(No. 26): pp. 21887–21902.
11. Jay, S., and Guillaume, M. 2014. “A novel maximum likelihood based method for mapping depth and water quality from hyperspectral remote-sensing data.” *Remote Sensing of Environment*, Vol. 147: pp. 121–132.
12. Dekker, A.G., Phinn, S.R., Anstee, J., Bissett, P., Brando, V.E., Casey, B., Fearns, P., Hedley, J., Klonowski, W., Lee, Z.P., Lynch, M., Lyons, M., Mobley, C., and Roelfsema, C. 2011. “Intercomparison of shallow water bathymetry, hydro-optics, and benthos mapping techniques in Australian and Caribbean coastal environments.” *Limnology and Oceanography: Methods*, Vol. 9: pp. 396–425.
13. Vahtmäe, E., and Kutser, T. 2013. “Classifying the Baltic Sea shallow water habitats using image-based and spectral library methods.” *Remote Sensing*, Vol. 5(No. 5): pp. 2451–2474.
14. Nazeer, M., Nichol, J.E., and Yung, Y.-K. 2014. “Evaluation of atmospheric correction models and Landsat surface reflectance product in an urban coastal environment.” *International Journal of Remote Sensing*, Vol. 35(No. 16): pp. 6271–6291.
15. Lyzenga, D.R. 1978. “Passive remote sensing techniques for mapping water depth and bottom features.” *Applied Optics*, Vol. 17(No. 3): pp. 379–383.
16. Stumpf, R.P., Holderied, K., and Sinclair, M. 2003. “Determination of water depth with high-resolution satellite imagery over variable bottom types.” *Limnology and Oceanography*, Vol. 48(No. 1): pp. 547–556.
17. Vahtmäe, E., and Kutser, T. 2007. “Mapping bottom type and water depth in shallow coastal waters with satellite remote sensing.” *Journal of Coastal Research*, Vol. 50 (SI): pp. 185–189.

18. Pe’eri, S., Smith, S., Snyder, L., and Madore, B. 2014. “Satellite- derived bathymetry using multiple images: the Alaska north slope case study.” Paper presented at the Proceedings of the 2014 Canadian Hydrographic Conference, St. John’s, NL, Canada, April 14–17, 2014.
19. Hulslander, D. 2013. “A quantitative comparison of traditional and image-derived bathymetry from Landsats 5, 7, and 8.” Abstract EP13A-0836, presented at the Fall Meeting of the American Geo- physical Union, San Francisco, California, USA, December 9–13, 2013.
20. Hedley, J., Roelfsema, C., Koetz, B., and Phinn, S.R. 2012. “Capability of the Sentinel 2 mission for tropical coral reef mapping and coral bleaching detection.” *Remote Sensing of Environment, Vol. 120(SI): pp. 145-155.*
21. Marrable, D. 2015. *PlanarRadPy, Open Source Batch Processing Software for PlanarRad*. Accessed August 02, 2015, https://github.com/marrabld/planarradpy.
22. Roelfsema, C., Phinn, S.R., Dennison, W.C., Dekker, A.G., and Brando, V.E. 2006. “Monitoring toxic cyanobacteria *Lyngbya majuscula* (Gomont) in Moreton Bay, Australia by integrating satellite image data and field mapping.” *Harmful Algae*, Vol. 5(No. 1): pp. 45–56.
23. NASA 2010. *Ocean Level-3 Standard Mapped Image Products*. Report. Accessed April 23, 2015, http://oceancolor.gsfc.nasa.gov/cmsdocs/technical documents/ocean level-3 smi products.pdf.
24. Franz, B.A., and Werdell, P.J. 2010. “A generalized framework for modeling of inherent optical properties in ocean remote sensing applications.” Paper presented at the Proceedings of the Ocean Optics Conference, Anchorage, Alaska, USA, September 27–October 1, 2010.
25. Maritorena S., Siegel, D.A., and Peterson A. 2002. “Optimization of a semi-analytical ocean color model for global scale applications.” *Applied Optics*, Vol. 41(No. 15): pp. 2705–2714.
26. Wettle, M., Brando, V.E., and Dekker, A G. 2004. “A methodology for retrieval of environmental noise equivalent spectra applied to four Hyperion scenes of the same tropical coral reef.” *Remote Sensing of Environment*, Vol. 93(No. 1–2): pp. 188–197.
27. Hedley, J., Harborne, A.J., and Mumby, P.J. 2005. “Simple and robust removal of sun glint for mapping shallow-water benthos.” *International Journal of Remote Sensing*, Vol. 26(No. 10): pp. 2107–2012.

28. Wilson, R.T. 2012. “Py6S: A Python interface to the 6S radiative transfer model” *Computers and Geosciences*, Vol. 51: pp. 166–171.
29. Vermote, E., Tanré, D., Deuze, J., Herman, M., and Morcette, J. 1997. “Second simulation of the satellite signal in the solar spectrum, 6S: an overview.” *IEEE Transactions on Geoscience and Remote Sensing*, Vol. 35(No. 3): pp. 675–686.
30. Clewley, D., Bunting, P.J., Shepherd, J., and Moghaddam, M. 2014. “A python-based open source system for geographic object-based image analysis (GEOBIA) utilizing raster attribute tables.” *Remote Sensing*, Vol. 6(No. 7): pp. 6111–6135.
31. USGS 2015. *Product Guide – Provisional Landsat 8 Surface Reflectance Product*. Report. Accessed October 15, 2015, http://landsat.usgs.gov/documents/provisional l8sr product guide.pdf.
32. CHS 2013. “*Standards for hydrographic surveys*.” Canadian Hydrographic Service, Ottawa. Accessed October 25, 2015, http://www.charts.gc.ca/data-gestion/hydrographic/standards- normes-eng.pdf.
33. Flater, D. 1994. “XTide, open source tidal prediction software.” Accessed August 25, 2015, http://www.flaterco.com/xtide/.
34. Maiersperger, T.K., Scaramuzza, P.L., Leigh, L., Shrestha, S., Gallo, K.P., Jenkerson, C.B., and Dwyer, J.L. 2014. “Characterizing LEDAPS surface reflectance products by comparisons with AERONET, field spectrometer, and MODIS data.” *Remote Sensing of Environment*, Vol. 136: pp. 1–13.
35. Claverie, M., Vermote, E.F., Franch, B., and Masek, J.G. 2015. “Evaluation of the Landsat 5 TM and Landsat 7 ETM+ surface reflectance products.” *Remote Sensing of Environment*, Vol. 169(No. 1): pp. 390–403.
36. Wilson, R.T. 2012. “Py6S: A Python interface to the 6S radiative transfer model” *Computers and Geosciences*, Vol. 51: pp. 166–171.
37. Ohlendorf, S., Müller, A., Heege, T., Cerdeira-Estrada, S., and Kobryn, H.T. 2011. “Bathymetry mapping and sea floor classification using multispectral satellite data and standardized physics-based data processing.” Paper presented at the Proceedings of SPIE Remote Sensing of the Ocean, Sea Ice, Coastal Waters, and Large Water Regions, Prague, Czech Republic, September 21–22, 2011.
38. Cerdeira-Estrada, S., Heege, T., Kolb, M., Ohlendorf, S., Uribe, A., Müller, A., Garza, R., Ressl, R., Aguirre, R., Mariño, I., Silva, R., and Martell, R. 2012. “Benthic habitat and bathymetry mapping of shallow waters in Puerto Morelos reefs using remote sensing with a physics based data processing.” Paper

presented at the Proceedings of the International Geoscience and Remote Sensing Symposium, Munich, Germany, July 22–27, 2012.

39. Hedley, J., Russell, B., Randolph, K., Dierssen, H. 2016. “A physics- based method for the remote sensing of seagrasses.” *Remote Sensing of Environment*, Vol. 174: pp. 134–147.
40. Goodman, J., and Ustin, S. 2007. “Classification of benthic composition in a coral reef environment using spectral unmixing.” *Journal of Applied Remote Sensing*, Vol. 1(No. 011501).

Chapter 3. Analyzing Performances of Different Atmospheric Correction Techniques for Landsat 8: Application for Coastal Remote Sensing

This chapter has been published in Remote Sensing.

Citation details: Christopher O. Ilori, Nima Pahlevan and Anders Knudby (2019): Analyzing Performances of Different Atmospheric Correction Techniques for Landsat 8: Application for Coastal Remote Sensing. Remote Sensing. 11(4), 469.

3.1. Abstract

Ocean colour (OC) remote sensing is important for monitoring marine ecosystems. However, inverting the OC signal from the top-of-atmosphere (TOA) radiance measured by satellite sensors remains a challenge as the retrieval accuracy is highly dependent on the performance of the atmospheric correction as well as sensor calibration. In this study, the performances of four atmospheric correction (AC) algorithms, ARCSI, ACOLITE, LaSRC, and SeaDAS, implemented for Landsat-8 Operational Land Imager (OLI) data, were evaluated. The OLI-derived remote sensing reflectance (R_{rs}) products (also known as Level-2 products) were tested against near-simultaneous in-situ data acquired from the OC component of the Aerosol Robotic Network (AERONET-OC). Analyses of the match-ups revealed that generic atmospheric correction methods (i.e., ARCSI and LaSRC), which perform reasonably well over land, provide inaccurate Level-2 products over coastal waters, in particular in the blue bands. Between water-specific AC methods (i.e., SeaDAS and ACOLITE), SeaDAS was found to perform better over complex waters with RMSE varying from 0.0013 to 0.0005 sr^{-1} for the 443 and 655 nm channels, respectively. Analyses of differences in spectral bands between satellite and in-situ measurements highlight the need for spectral adjustment for validation purposes, particularly in the green and red bands. Of the four AC algorithms, SeaDAS is the most sensitive to spectral band differences, with the largest difference (improvement) in the 655 nm channel. An assessment of the effects of dominant environmental variables revealed AC retrieval errors are influenced by solar zenith angle and wind speed for some methods and bands. Recognizing that the AERONET-OC sites are not representative of all inland waters, extensive research and analyses are required to further evaluate the performance of

various AC methods for medium resolution imagers like Landsat 8 and Sentinel-2 under a broad range of aquatic/atmospheric conditions.

Keywords: atmospheric correction; remote sensing reflectance; Landsat 8; band adjustment; validation; AERONET-OC.

3.2. Introduction

Ocean colour remote sensing provides information on in-water optical properties indicating the concentrations of water constituents like chlorophyll-a. In optically shallow waters, depth and seafloor spectral reflectance may also be estimated using remotely sensed images. Information about near-surface, in-water optical properties, in the form of water quality maps, can provide advance warning of algal bloom development [1] and potentially lead to early mitigation efforts to reduce health risks and financial losses. Bathymetric maps, derived from water depth estimates, can be used to produce or update navigational charts [2], reducing the risk of ship groundings. Benthic habitat maps, inferred from seafloor spectral reflectance, can be used to track changes in the distribution of seafloor habitats [3,4]. However, extracting ocean colour products such as chlorophyll-a, water depth and bottom types from remotely sensed images is difficult because, over blue ocean waters, of the total signal that reaches the TOA (Top of Atmosphere), only ~10% typically comes from within the water column [5]. In addition to the radiation leaving the water column (L_w), the TOA radiance measured by satellite sensors includes contributions from scattering and absorption in the atmosphere and reflection at the sea surface [6]. It is important to estimate and remove the contribution from these other sources, in order to estimate L_w, which is readily normalized by the total downwelling irradiance just above the sea surface to yield R_{rs}.

Atmospheric effects are removed through atmospheric correction (AC) [7], but residual errors in AC can introduce large uncertainties in R_{rs} estimates, resulting in erroneous retrieval of OC products such as apparent optical properties of water [8]. In open ocean waters, where phytoplankton governs the optical regime, it can be conveniently assumed that there is no water-leaving radiance in the near-infrared (NIR) region such that any measured TOA radiance in this spectral band is attributed to atmospheric path radiance and reflectance from the water surface. While this assumption is valid for open-ocean (Case 1) waters, in shallow or optically complex (Case 2) waters that are, in general, characterized by a combination of constituents, such as phytoplankton, coloured dissolved organic matters and suspended particulate matters, R_{rs}(NIR) may be significantly greater than zero. This is because bottom reflectance (which can come from highly reflective near-surface vegetation) and backscattering by suspended materials can produce reflectance [9]. This can lead to over-correction of atmospheric and surface reflectance effects, leading to underestimation and even negative L_{w} estimated within the shorter wavelengths used to derive OC products [9,10]. To account for the non-negligible R_{rs}(NIR), algorithms that work for Case 2 waters have been developed (e.g., [10-12]) and tested (e.g., [13,14]). With these efforts, it is now possible to retrieve L_{w} over coastal waters. However, the low spatial resolution of traditional ocean colour sensors inhibits the detection of detailed features that are not easily discernible in low resolution satellite images. The recent availability of higher-resolution satellite sensors, e.g. Landsat 8 Operational Land Imager (OLI) and Sentinel-2 Multispectral Instrument (MSI), with adequate spectral and radiometric characteristics for ocean colour applications has the potential to greatly improve coastal ocean colour applications, including water quality [15,16], bathymetry, and seafloor habitat mapping [17].

Optimizing the utility of the OLI sensor for aquatic science and applications requires validating R_{rs} products to better understand its potential and limitations. A few recent studies have started investigating the quality of OLI-derived R_{rs} for coastal applications. For example, Pahlevan et al. (2017a) [15] used the AC scheme in the SeaWiFS Data Analysis System (SeaDAS) software package to determine the best Landsat 8 band combinations that can minimize error in R_{rs} retrieval over different coastal water types at selected AERONET-Ocean Colour (OC) sites. Using newly computed calibration gains, they revealed that OLI-derived R_{rs} estimates are as good as those from other ocean colour sensors. Likewise, the work of Franz et al. (2015) [18] illustrated the importance of OLI data for water-related studies. By employing the AC process in the SeaDAS Level-2 processing algorithm (l2gen), they assessed the quality of OLI-derived R_{rs} and subsequently retrieved chlorophyll-a concentration over the Chesapeake Bay, USA. In agreement with Pahlevan et al. (2017a) [15], they found that with a precise AC procedure the high radiometric quality and improved imaging capabilities of OLI hold great promise for satellite-based coastal monitoring. Doxani et al. (2018) [19] tested a wide range of AC algorithms over different land cover types, highlighting the strengths and limitations of each algorithm. More recently, Wei et al. (2018) [20] also assessed four AC algorithms with a focus over water bodies, revealing that the NIR-SWIR approach implemented in SeaDAS produced the most robust R_{rs} estimates from Landsat 8. However, none of these studies examined the effects of environmental variables (such as wind speed) on the retrieval accuracy of AC algorithms.

With the proliferation of OC products usage among the science community, and the need for robust R_{rs} products, it is important to understand the potential of AC algorithms. Most of the ocean colour community has for years been using water-based AC methods for a wide range of applications from coastal to inland waters, so it is important that the effects of relevant environmental variables on the R_{rs} retrieval accuracy of these AC algorithms is examined. Such knowledge may assist in the choice of AC algorithm for a given set of environmental conditions, and/or improved R_{rs} retrieval under a wider range of conditions. Equally, it is important that other users interested in studying inland waters (e.g., biogeochemists, aquatic biologists) fully understand the accuracy of non-water based AC processors, in particular, the land surface reflectance product, which is commonly used.

Here we pursued an approach similar to Pahlevan et al. (2017a) [15], but expanded it by evaluating the performances of four different AC algorithms to determine which method produces the most robust R_{rs} products in shallow coastal waters. Also, like Doxani et al. (2018) [19], we tested both land-based and water-based algorithms at multiple sites, but covered more sites over a longer time period to better capture space-time dynamics related to water optical properties. Using 54 in-situ measurements from 14 AERONET-OC sites, we (1) tested the following algorithms for atmospheric correction of Landsat 8 images: a) Atmospheric and Radiometric Correction of Satellite Imagery (ARCSI) [21], b) the Atmospheric Correction for OLI 'lite' (ACOLITE) [22], c) NASA's standard algorithm as implemented in the SeaWiFS Data Analysis System (SeaDAS) [8] and, d) the United States Geological Survey's standard land-based AC used to produce the Landsat 8 Surface Reflectance (LSR) Climate Data Record (Landsat CDR), herein referred to as LaSRC [23], (2) analysed the differences in spectral bands between satellite and in-situ measurements, and (3) examined the effects of three key environmental variables on the R_{rs} retrieval accuracy of water-based AC algorithms. To our knowledge, this is the first inter-comparison exercise that tested AC algorithms using representative data from many coastal sites with varying atmospheric conditions and optical properties, combining the three approaches mentioned above in a single study.

3.3. Materials and Methods

3.3.1. Landsat 8 OLI data

OLI measures TOA radiance in the visible, NIR and short-wave infrared (SWIR) bands, at a spatial resolution of 30 m. Compared to its predecessors, OLI includes a new coastal/aerosol band (435-451 nm) in addition to the traditional blue (452-512 nm), green (533-590 nm) and red (636-673 nm) bands. The addition of a new band, together with an enhanced spectral coverage and radiometric resolution, enables improved observation of water bodies from space and the ability to estimate the concentration of atmospheric aerosols for AC [16,24,25] (note that aerosol estimation for AC by the coastal band is done over land). Compared to data from existing global ocean colour missions, the higher spatial resolution has the potential to make important contributions to ocean colour remote sensing, such as separating and mapping in-water constituents in coastal waters [16,25]. Although OLI signal-to-noise ratios (SNRs) (Table 3.1) are generally lower than those of heritage ocean colour sensors such as SeaWiFS or MODISA (MODIS onboard the Aqua platform), the relatively high visible band SNRs (particularly in the coastal/aerosol and blue bands) and the improved SNR across all bands compared to past Landsat missions improves OLI’s ability to measure subtle variability in surface conditions and ultimately make OLI data a new and valuable data source for ocean colour studies [16,18].

Table 3.1. Comparison of the band centers and the signal-to-noise ratios of MODIS and Landsat 8 OLI at specified levels of typical spectral radiance.

			Band centres (nm)				
MODIS	443	488	555	645	858	1640	2130
SeaWiFS	443	490	555	670	865	NA	NA
OLI	443	482	56	655	865	1609	2201
			Signal-to-noise ratio (SNR)				
MODIS	838	802	228	128	201	275	110
SeaWiFS	950	1000	850	500	350	NA	NA
OLI	344	478	279	144	67	30	14
			L typ (w m-2 μ-1 sr-)				
MODIS	4.9	32.1	29	21.8	24.7	7.3	1.0
SeaWiFS	70.2	53.1	33.9	8.3	4.5	NA	NA
OLI	69.8	55.3	27.5	13.4	4.06	0.353	0.0467

3.3.2. AERONET-OC data

To validate the performance of the AC processors applied to the OLI data, we acquired 122 cloud-screened and fully quality-controlled Level 2.0 AERONET-OC in-situ measurements of normalized water-leaving radiance (nLw) for 14 AERONET-OC sites, including 12 coastal sites (Galata Platform, Gloria, GOT Seaprism, Gustav Dalen Tower, Helsinki Lighthouse, Long Island Sound Coastal Observatory (LISCO), Martha's Vineyard Coastal Observatory (MVCO) , Thornton C-Power, USC Seaprism, Venise, WaveCIS Site CSI-6, Zeebrugge-MOW1) and two lake sites (Lake Erie, Palgrunden) (Figure 3.1). AERONET-OC, managed by NASA’s Goddard Space Flight Center (GSFC) [26], is a sub-network of the AERONET federated instrument [27,28]. Although OLI and AERONET-OC have somewhat different spectral bands, a set of comparable bands centred at 441 nm, 491 nm, 551 nm, and 667 nm can be used for cross-comparison purposes. Thus, AERONET-OC data were collected in four spectral bands centered at 441, 491, 551, and 667 nm, for comparison with OLI’s four visible bands, centered at 443, 483, 561 and 655 nm. Note that there is a slight difference, i.e., ±1 to ±3 nm, in all four bands for some sites. As Rrs is not directly available from the AERONET-OC sites, the normalized water-leaving radiances (nLw, W m-2 sr-1) were divided by the top-of-the atmosphere (TOA) solar irradiance (F0) [29] to obtain Rrs.

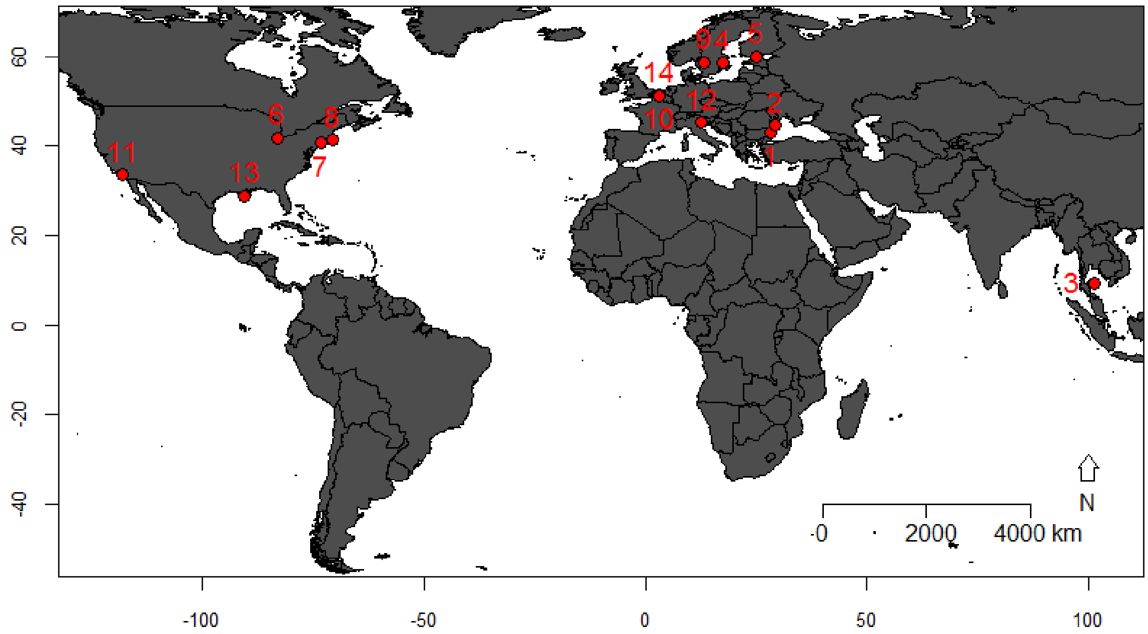

Figure 3.1. **Map showing the 14 validation sites from AERONET-OC station (1: Galata, 2: Gloria, 3: GOT Seaprism, 4: Gustav Dalen Tower, 5: Helsinki, 6: Lake Erie, 7: LISCO, 8: MVCO, 9: Palgrunden, 10: Thornton C-Power; 11: USC Seaprism, 12: Venise, 13: WaveCIS Site CSI, 14 Zeebrugge-MOW1).**

3.4. Match-up exercise

To obtain the in situ R_{rs} data needed to test AC procedures for OLI, we performed a match-up exercise between the AERONET-OC measurements and OLI data as follows: (i) Using the OLI metadata database file provided by USGS, python code was created to automatically retrieve all Landsat 8 OLI scenes and the contemporaneous AERONET-OC data (from AERONET-OC website) that are within a ± 30-minute time window of Landsat 8 overpass times, for the April 2013 - May 2017 timeframe (note that a strict time window of ± 30-minute, which greatly reduces the number of match-up pairs, was used to limit the influence of variability from processes such as high tides, rapid current and particulate dynamics in water masses, thus improving the quality of match-ups). This yielded a text file containing a total of 122 match-ups with coincident satellite and in-situ data, for 14 AERONET-OC sites (Figure 3.2), as well as information on aerosol optical thickness, SZA and wind speed for each match-up. All corresponding OLI scenes were subsequently bulk-downloaded using Landsat-util, a tool to automatically find and download multiple Landsat 8 scenes. Some of the 122 OLI data visibly contained a non-negligible amount of specular reflection off the sea surface (sunglint). As not all AC algorithms have the capacity for sunglint correction, to obtain realistic and comparable R_{rs} across all AC methods, scenes with visible specular reflection were excluded. All images were subsequently processed by each AC algorithm (as described in Section 2.4.2). (ii) Following the approach of Bailey and Werdell (2006) [30], a regional subset of Landsat 8 data was generated for each image from all AC algorithms that were employed in this study, by obtaining a 7x7 pixel box centred on the location of the AERONET-OC site. To avoid errors introduced by the presence of the AERONET-OC measurement platforms themselves, the centre 3x3 pixel window was excluded. (iii) Valid satellite match-ups were retrieved in the 7x7 box by enforcing the SeaDAS exclusion flags, which include flags for land, clouds, cloud-shadow, ice, stray light, low nL_w (555), high viewing zenith angle ($> 60^{o}$), high sunglint and high TOA radiance. To ensure a fair comparison, it should be noted that only the common match-ups from all AC algorithms were used for further analysis (a total of 248 match-ups were produced by all AC algorithms: ACOLITE: 56, ARCSI: 69, LaSRC: 69, SeaDAS: 54). To ensure an unbiased intercomparison, we included pixels with negative (Supplemental Data 3E) and zero R_{rs} retrievals from all methods. (iv) We then obtained the per-band median R_{rs} values of the unflagged pixels for final validation with in situ data. The median AERONET-OC measurements collected within the ± 30-minute window of Landsat 8 overpass were utilized to represent in situ match-ups.

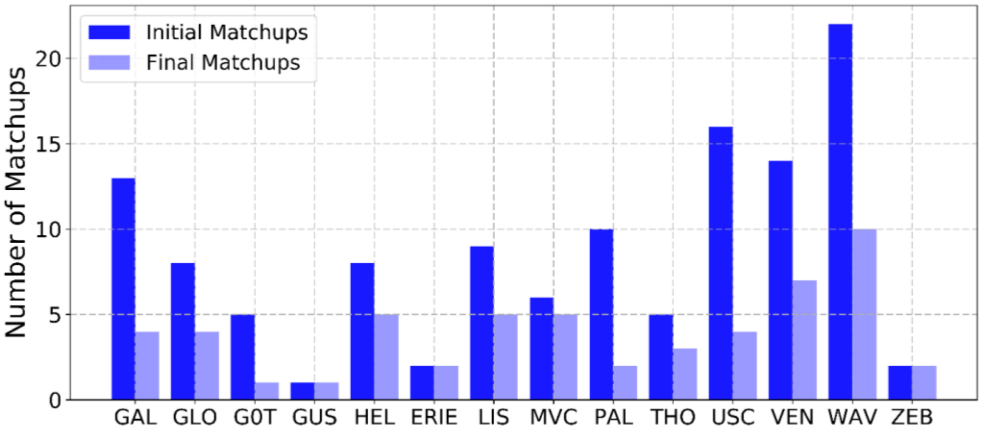

Figure 3.2. **Number of match-ups between Landsat 8 OLI scenes and AERONET-OC site measurements within ± 30-minute window of Landsat-8 overpass. GAL: Galata, GLO: Gloria, GOT: Got Seaprism, GUS: Gustav Dalen Tower, HEL: Helsinki, ERIE: Lake Erie, LIS: LISCO, MVC: MVCO, PAL: Palgrunden, THO: Thornton C-Power, USC: USC Seaprism, VEN: Venise, WAV: WaveCIS Site CSI, ZEB: Zeebrugge-MOW1). Dark blue represents the total number of initial match-ups within a ± 30-minute time window of Landsat 8 overpass times for each site. Light blue represents the total number of final match-ups used for analysis after excluding scenes with sunglint and performing the match-up exercise.**

3.5. Data processing

3.5.1. Description of atmospheric correction (AC) algorithms

Atmospheric correction of the OLI data was carried out using four algorithms: ARCSI, ACOLITE (version 20170113.0), SeaDAS (version 7.4) and LaSRC. Note that LaSRC is a product which has already been processed to surface reflectance by the United States Geological Survey (USGS). Both ACOLITE and SeaDAS have been specifically designed for AC over water surfaces, whereas ARCSI and LaSRC have not; we therefore refer to the latter two as land-based methods. The output of the water-based methods is R_{rs}, which is directly comparable to the in-situ data from AERONET (after conversion: $R_{\mathrm{rs}} = \mathrm{n}L_w / \mathrm{F}_0$), while the output of the land-based methods is in units of above-surface diffuse reflectance $\mathrm{R}(0^+)$, which we converted to R_{rs} using:

$$R_{rs} = R(0^+)/\pi, \tag{3.1}$$

ARCSI is an open-source software program developed at Aberystwyth University [21]. It is a relatively new AC algorithm with functionalities to process multispectral images from both commercial and publicly available sensors and also to obtain processed data for direct use in remote sensing analyses [31]. It is a command line tool where Py6S [32] can be implemented to correct multispectral images to above-surface diffuse reflectance using the 6S model [33], which simulates ground and atmospheric radiation under a variety of conditions. Within the 6S method, input parameters such as Aerosol Optical Thickness (AOT), vertical column water vapour and ozone concentration are automatically used by the 6S method to characterize the state of the atmosphere.

ACOLITE is a binary distribution of Landsat 8 OLI and Sentinel-2 MSI processing developed by the Royal Belgian Institute of Natural Sciences [22,34]. It is an image-based AC algorithm that estimates L_w by correcting for molecular and aerosol scattering in the atmosphere using the Gordon and Wang (1994a) approach [5]. Molecular reflectance correction, based on viewing and illumination geometries, is performed with a 6SV-based look-up table [33] . Unlike SeaDAS, which uses 12 aerosol models for aerosol estimation [5,35], aerosol reflectance is estimated by determining aerosol type from the ratio of reflectances in two SWIR bands over water pixels where reflectance can be assumed zero, an approach similar to Ruddick et al. (2000) [36]. Based on this assumption, it also retrieves water-leaving reflectances in both the visible and NIR bands together with other parameters of interest in marine and inland waters. ACOLITE is primarily designed for processing Landsat 8 OLI data for aquatic remote sensing applications, but has recently been modified and updated to include processing of Sentinel-2 MSI data [37].

LaSRC is a Level-2 data set produced and released as provisional products by the USGS since January 2015, primarily to support terrestrial remote sensing applications. Unlike the precursor algorithm (LEDAPS) used for previous Landsat satellites (Landsat 4-5 TM and Landsat 7 ETM+), which used the 6S model, LaSRC is generated using a dedicated Landsat Surface Reflectance code [24]. Data are available as standalone climate data records (CDRs) which represent specific geophysical and biophysical properties of the land surface [23]. AC is mainly based on the MODIS collection 6 AC algorithm, which uses a radiative transfer model for the inversion of atmospheric parameters such as aerosol and water vapour [24]. It should be noted that surface reflectance is provided in seven spectral bands (the first seven OLI bands) only for scenes with solar zenith angle less than 76°, and that bands 443 and 482 nm are not suitable for analysis as they are ‘consumed’ for aerosol inversion tests within the LaSRC. Although still provisional and under continuous improvement, LaSRC has been validated and assessed for land applications [38-41], and has a dedicated aerosol retrieval algorithm for pixels over water [23](19)(19).

SeaDAS, which uses two NIR bands for aerosol estimation, contains an AC scheme originally designed for open ocean water based on the assumption of negligible L_w in the NIR bands. This approach, which is NASA’s operational AC algorithm [5], includes an l2gen (Level 2 generator) to retrieve R_{rs} and other optical and geophysical water and atmospheric properties. Following some improvements on how to estimate aerosol contributions (e.g., [12,42,43]) the l2gen processor in SeaDAS can now be used for deriving R_{rs} in both moderately and highly turbid coastal waters [14]. Following the release of SeaDAS Version 7.2, Landsat 8 OLI data can be processed with the l2gen processor [18].

3.5.2. Atmospheric correction procedure and validation

To derive R_{rs}, all four AC algorithms were parameterized using their default processing options. In addition, the following processing was implemented. In SeaDAS, out-of-band correction options was set to zero (outband_opt=0), i.e., R_{rs} was reported at full bandpass, without correction to the nominal band center, and no sunglint correction was implemented (glint_opt = 0) since there is no such correction option in other algorithms. In ARCSI, the ‘clear water’ option was used for the reflectance of a ground target as processing requires an option from ‘green vegetation’, ‘clear water’, ‘sand’ or ‘lake water’. Also, AOT and other atmospheric parameters were automatically identified and estimated by ARCSI during batch processing. To derive AOT for each scene, realistic minimum and maximum values of 0.001 and 0.9, respectively, were manually specified. Finally, to allow for consistency among all methods, we assumed a perfect sensor calibration by applying unity gains for vicarious calibration across all bands for all processors. For SeaDAS, aerosol correction was implemented following the Gordon and Wang (1994a) approach [5], with the NIR/SWIR correction option (865–1609 nm band combination), as suggested in Pahlevan et al. (2017a) [15] and Mobley et al. (2016) [7]. ACOLITE aerosol correction was implemented using the default SWIR option (1609 and 2201 nm band combination) which computes Rayleigh-corrected reflectance from the SWIR bands for moderate and turbid waters. Each AC algorithm was applied to the final

54 Landsat 8 OLI scenes, representing a wide variety of coastal and atmospheric conditions (Supplemental Data 3B). When comparing their performance, we consider AERONET-OC data as reference with negligible uncertainties. Note that uncertainties in the AERONET-OC in situ measurements are ~5% in the blue to green bands and ~8% in the red band [26]. As noted in Pahlevan et al. (2017b) [44] and Mélin and Sclep (2015) [45], compensating for discrepancies arising from the differences in nominal band centre wavelengths is crucial for obtaining a robust match-up analysis across all spectral bands (in particular for OLI's relatively broad spectral bands). To this end, we carried out a spectral band adjustment using the deep neural network approach as described in Pahlevan et al. (2017b) [44] and compared R_{rs} derived with and without band adjustments.

The algorithm performance was compared using six metrics including:

$$\mathrm{RMSE} = \sqrt{\frac{1}{n}\sum_{i=1}^{n}\left(x^{mea} - x^{est}\right)^2}\,, \tag{3.2}$$

$$\text{mean bias} = \frac{\sum_{i=1}^{n}\left(x^{mea} - x^{est}\right)}{n}\,, \tag{3.3}$$

$$\text{spectral angle} = \cos^{-1}\left(\frac{\sum_{i=1}^{n} x^{mea}.x^{est}}{\sqrt{\sum_{i=1}^{n} x^{mea^2}}\sqrt{\sum_{i=1}^{n} x^{est^2}}}\right), \tag{3.4}$$

as well as the coefficient of determination (R^2), slope, and intercept of the line fitted using least-squares regression between in-situ and satellite R_{rs} estimates. x^{mea} and x^{est} are AERONET-OC and satellite-derived R_{rs} data, respectively. The spectral angle, which is insensitive to spectra amplitude, is used to quantify the similarity between satellite and in situ R_{rs} spectra. Values close to 0 indicate high similarity.

3.6. Results and Discussion

3.6.1. Validation of AC algorithms

Scatter plots showing the estimated (OLI) and observed (AERONET-OC) R_{rs} values for each match-up are presented in Figure 3.3, and summary statistics are tabulated in Table 3.2. There are clear differences between the water-based and land-based AC algorithms, with SeaDAS and ACOLITE outperforming ARCSI and LaSRC in all metrics for all bands, with only one exception (slope for R_{rs}(482)). Between the two water-based methods, SeaDAS outperforms ACOLITE in every metric for all bands, with the exception of slopes for R_{rs}(482), R_{rs}(561), and R_{rs}(655). SeaDAS has spectral angels and RMSEs close to zero (spectral angles between 0.31 and 0.16 and RMSEs between 0.0013 and 0.0005 across all four wavelengths) demonstrating a high degree of similarity between in-situ and OLI-estimated R_{rs} with OLI data processed through SeaDAS (Table 3.2). A comparison of RMSE results of the per-band difference with and without band adjustments (Supplemental Data 3A) shows that SeaDAS was the AC method most sensitive to spectral band differences, with the largest improvement of band adjustment occurring in the 655 nm channel. Spectral Angle values obtained for all algorithms showed that SeaDAS and ACOLITE have the highest similarity with in-situ RrsRemote Sens. spectra (ARCSI: 0.46, ACOLITE: 0.27, LaSRC: 0.53 and SeaDAS: 0.20)

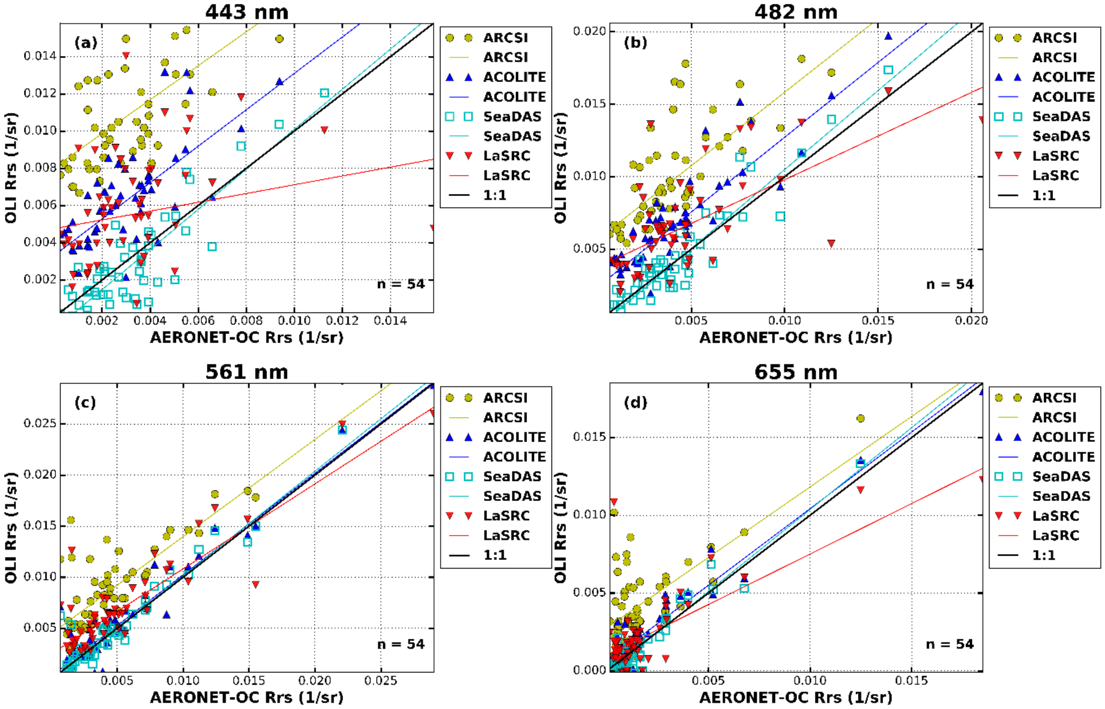

Figure 3.3. **Scatterplots of the relationship between in-situ measurements (x-axis) and OLI estimates (y-axis) for each OLI band acquired over 14 AERONET-OC sites. Regression lines are shown in colours, while the thick dotted black lines are 1:1 lines.**

Table 3.2. Statistical results for the retrieved R_{rs} obtained for all processors with and without band adjustment (values in parenthesis represent results without band adjustment). Best metrics are highlighted in bold letters. After band adjustment linear fit, which was employed to reveal the relationship between in-situ and modelled R_{rs}, improves with increasing wavelength for both ACOLITE and SeaDAS, with R^2 values of 0.70/0.84, 0.85/0.92, 0.92/0.95 and 0.93/0.97 for bands 1 through 4 for ACOLITE/SeaDAS, respectively. A similar trend is seen for ARCSI and LaSRC for the first three bands.

	R^2	Slope	RMSE (1/sr)	Intercept	p-values
			Rrs 443		
ARCSI	0.43 (0.41)	0.91 (0.89)	0.0085 (0.0085)	0.0080 (0.0084)	8.92e-08
ACOLITE	0.70 (0.68)	**0.97 (0.97)**	0.0039 (0.0039)	0.0036 (0.0037)	4.16e-15
LaSRC	0.05 (0.05)	0.23 (0.25)	0.0042 (0.0042)	0.0050 (0.0050)	0.11
SeaDAS	**0.84 (0.84)**	1.08 (1.08)	**0.0013 (0.0013)**	**-0.0006 (-0.0006)**	**2.36e-22**
			Rrs 482		
ARCSI	0.68 (0.63)	**1.01 (0.92)**	0.0065 (0.0063)	0.0060 (0.0061)	2.00e-13
ACOLITE	0.85 (0.79)	1.03 (0.94)	0.0032 (0.0031)	0.0027 (0.0029)	1.99e-14
LaSRC	0.44 (0.43)	0.60 (0.56)	0.0035 (0.0035)	0.0041 (0.0041)	3.77e-08
SeaDAS	**0.92 (0.87)**	1.09 (1.00)	**0.0012 (0.0015)**	**-0.0002 (0.00009)**	**5.44e-30**
			Rrs 561		
ARCSI	0.77 (0.77)	0.95 (0.97)	0.0051 (0.0048)	0.0046 (0.0042)	5.27e-18
ACOLITE	0.92 (0.87)	**1.00 (0.98)**	0.0016 (0.0019)	0.0005 (0.0002)	1.38e-29
LaSRC	0.80 (0.78)	0.83 (0.83)	0.0030 (0.0029)	0.0027 (0.0025)	9.48e-20
SeaDAS	**0.95 (0.92)**	1.03 (1.21)	**0.0012 (0.0011)**	**0.00005 (-0.0003)**	**1.13e-34**
			Rrs 665		
ARCSI	0.64 (0.63)	0.91 (1.06)	0.0033 (0.0034)	0.0028 (0.0026)	4.49e-13
ACOLITE	0.93 (0.89)	0.98 (1.13)	0.0010 (0.0013)	0.0006 (0.0005)	1.91e-31
LaSRC	0.52 (0.50)	0.65 (0.75)	0.0022 (0.0021)	0.0011 (0.0010)	8.39e-10
SeaDAS	**0.97 (0.92)**	**1.01 (1.21)**	**0.0005 (0.0011)**	**-0.0001 (-0.0003)**	**4.00e-40**

The overall performance of SeaDAS reveals that the NIR-SWIR aerosol correction option can yield satisfactory results in low-to-moderately turbid waters. A possible reason for this is that the aerosol correction scheme, constructed following Ahmad et al. (2010) [42], was based on aerosol data obtained mainly from AERONET-OC sites [45]. Comparison of R^2 values among all methods shows that the lowest and most diverse values are in the 443 nm wavelength, with values between 0.05 and 0.84. For LaSRC in particular, the regression line for the comparison in the 443 nm wavelength deviates very much from the 1:1 line, yielding a poor R^2 and slope (Figure 3.3). This poor correlation and low RMSE (R^2: 0.05, slope: 0.23) is mostly a result of the large discrepancies between the observed and estimated R_{rs} for the Zeebrugge-MOW1 site, where mean R_{rs} was underestimated by ~70%. This is the largest underestimation by any method, across all sites. For this site, which is one of the most turbid sites in the AERONET-OC network, mean observed in-situ R_{rs} in the red band is 0.0155 sr^{-1}, making it the only site with $R_{rs}(655)$

one order of magnitude greater than the mean value of ~0.001 sr^{-1} observed for all 14 AERONET-OC sites. This level of turbidity is common for this site, which is located only ~3.65 km from coastline and receives sediment-rich water inputs from nearby rivers, as also noted by Vanhellemont and Ruddick (2015) [46] and as clearly visible in additional scenes excluded during the match-up exercise. Note that the TOA radiance data were used ‘as is’ without optimizing the vicarious calibration gains (as computed by Pahlevan et al. (2017a) [15]), which might further improve R_{rs} retrievals. Similarly, none of the AC methods, with different configuration capabilities which might improve performance, was optimized as there is no optimal setting that can work for all cases considered in this paper.

3.6.2. Inter-comparison of reflectance spectra at each site

Comparison of mean estimated and observed R_{rs} at each AERONET-OC site (Supplemental Data 3d) shows that all algorithms except SeaDAS generally overestimate R_{rs} across all wavelengths, with the largest and smallest overestimation occurring in the 443 and 665nm wavelengths, respectively. This is further supported by the RMSE and bias results (Figure 3.4). The largest errors (RMSE) and overestimations (bias) are observed in the 443 nm wavelength, probably due to the strong atmospheric scattering in this band. ARCSI has the largest overall positive bias in this wavelength, and indeed the highest overestimation at each site. However, its R_{rs} results across all wavelengths at the Zeebrugge-MOW1 site compare well with R_{rs} estimates from SeaDAS and ACOLITE. This suggests that ARCSI has a low sensitivity to the high concentrations of suspended sediments that dominate this site, as reported by De Maerschalck and Vanlede (2013) [47]. This may also serve as an indication that ARCSI can better deal with turbid conditions than LaSRC, which underestimates R_{rs} by ~45% at this site. The failure of LaSRC in this wavelength is likely due to the fact that it is part of the bands used for validating the accuracy of the aerosol inversion scheme [23].

The best performance from LaSRC across all bands is at Lake Erie (with two match-ups) where all other AC algorithms except ARCSI also have the best match with in-situ R_{rs}. LaSRC outperforms other algorithms in the first three bands. Percentage difference values are 4.5%, -3.2% and -0.3% for the first three bands, respectively. For ACOLITE and SeaDAS, the corresponding values are 28.8/-20.7%, 13.6/-12.8% and -0.4/-6.4%. Indeed, LaSRC has the best R_{rs} estimate of all methods in the 561 nm channel, while ACOLITE has the best R_{rs} estimate in the 655 nm channel, with a percentage difference of -1.3%, whereas both SeaDAS and LaSRC are -18.2% and -30%, respectively. Similar to the estimated R_{rs} by LaSRC in Lake Erie in the 561 nm channel, it also agrees well with in-situ R_{rs} at Zeebrugge-MOW1 site; the percentage difference here is -0.25%. For SeaDAS and ACOLITE, these values are 6.7% and 4.1%, respectively. LaSRC also outperforms other AC algorithms in the 443, 482 and 655 nm channels at the GOT-Seaprism site, with only one match-up. Percentage differences between estimated and in situ R_{rs} are 8.8%, 11.1% and -40.8%, respectively. For ACOLITE and SeaDAS, the corresponding values are 87.7/-79.3%, 60.9/-46.3%, and 96.4/-127.6%. This is the only site where SeaDAS uncharacteristically underestimates R_{rs} across all 4 bands. While any conclusion is tentative as GOT Seaprism (date: 2014026) only has one match-up, the poor performance of SeaDAS here is as a result of algorithm failure (very low R_{rs} in 443, 482 and 561 nm wavelengths, and negative R_{rs} in 655 nm wavelength) which can be attributed to conditions such as residual effects from cloud shadow or overcorrection for aerosol contribution in one or more visible band. Overcorrection typically occurs when water-leaving radiance is non-negligible in the band used to estimate the aerosol contribution [48]. Other instances of failure (as defined above) from one or more algorithms are: ACOLITE (Gloria 2014358: band 4, USC Seaprism 2016222: bands 3 and 4), SeaDAS (GOT Seaprism 2014026: band 4, Helsinki 2013235: band 1, Palgrunden 2013156: band 1, USC Seaprism 2016222: band 4, USC Seaprism 2016334: band 4, Venise 2015221: band 4), LaSRC (WaveCIS: 2013221: bands 1 and 4). The low or negative R_{rs} retrievals from these algorithms indicate a limitation of these algorithms at dealing with the atmospheric and water quality conditions present at those match-ups.

One possible reason for the generally poor performance of ARCSI can be the aerosol contribution removal which relies on estimates from 1) dense dark vegetated surfaces, based on the assumption that reflectance of vegetated pixels is sufficiently dark and a linear relationship between reflectance in the SWIR and blue bands or 2) dark pixels in the blue band, based on the assumption of an invariant aerosol concentration over the entire scene. However, these assumptions can easily be violated: i) finding a vegetated pixel that satisfies this condition may be difficult in scenes acquired over coastal waters, and ii) AOT variations may be sufficiently large such that adjoining pixels may have significantly different AOT. For the blue bands in particular, per-scene AOT estimates may lead to erroneous retrievals. For LaSRC, the generally poor performance may be due to the use of land-based pixels for aerosol estimation, which is typically not appropriate for water surfaces. In addition, for LaSRC, retrieving accurate R_{rs} estimates over water requires the presence of a considerably large land area adjoining the water pixels. The majority of the AERONET-OC sites used in this study only have relatively small nearby land surfaces. This may help explain the few instances of good performances near land masses (e.g. for the Lake Erie, Zeebrugge MOW-1 sites).

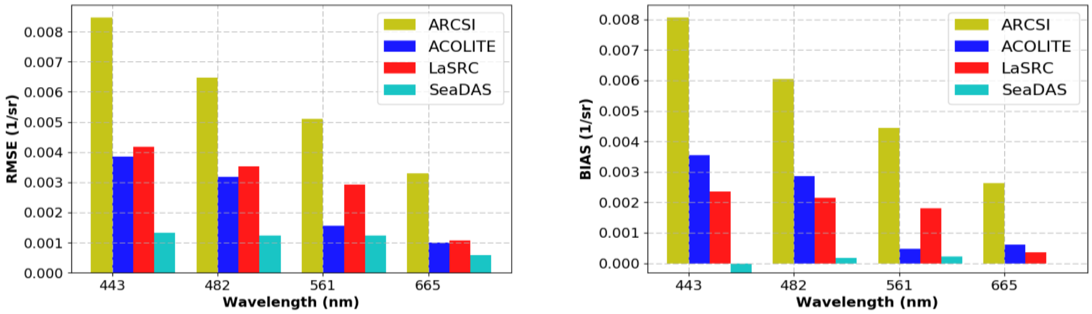

Figure 3.4. Overall band-by-band RMSE and mean bias results for all algorithms.

3.6.3. Influence of environmental factors for SeaDAS and ACOLITE

To understand the impact environmental factors may have on R_{rs} retrieval errors from the water-based AC methods, we investigated the influence of three variables: aerosol optical thickness (AOT) at 869 nm, hereafter referred to as AOT(869), SZA, and hourly wind speed. These three variables are known to influence R_{rs} retrievals [49,50), e.g. AOT(870) and SZA have been found to reduce the quality of water-leaving radiance derived from SeaWiFS and MODIS sensors [51]. Figures 5a-c illustrates the error (x^{est} - x^{mea}) for each match-up point as a function of each environmental parameter, for each AC method. Negative values imply that an algorithm underestimated the observed R_{rs} value, and vice versa. We used tests of the statistical significance (two-tailed, α = 0.05, critical value = 0.2262) of the individual Pearson correlation coefficients to guide this analysis. While ACOLITE consistently overestimated R_{rs} in the 443, 482 nm bands, as also noted by Vanhellemont et al. (2014c) [52] , errors for both SeaDAS and ACOLITE were not significantly influenced by AOT (Figure 5a, no statistically significant correlations). However, SZA was significantly and positively correlated with R_{rs} retrieval errors from SeaDAS for all four bands (i.e., r = 0.495486743, 0.483529464, 0.253699366 and 0.427793365, respectively), and from ACOLITE for the 443 and 482 nm bands (i.e., r = 0.239717715 and 0.228792001, respectively) (Figure 5b). A similar pattern was evident for wind speed, which was significantly positively correlated with R_{rs} retrieval errors from

SeaDAS for all bands except band 3 (for which the positive correlation is present but not statistically significant), and from ACOLITE for the 443 and 482 nm bands (Figure 5c). These patterns, while generally causing only small errors in R_{rs} retrieval, may guide the further development of both AC methods to make them more robust across the spectrum of environmental conditions.

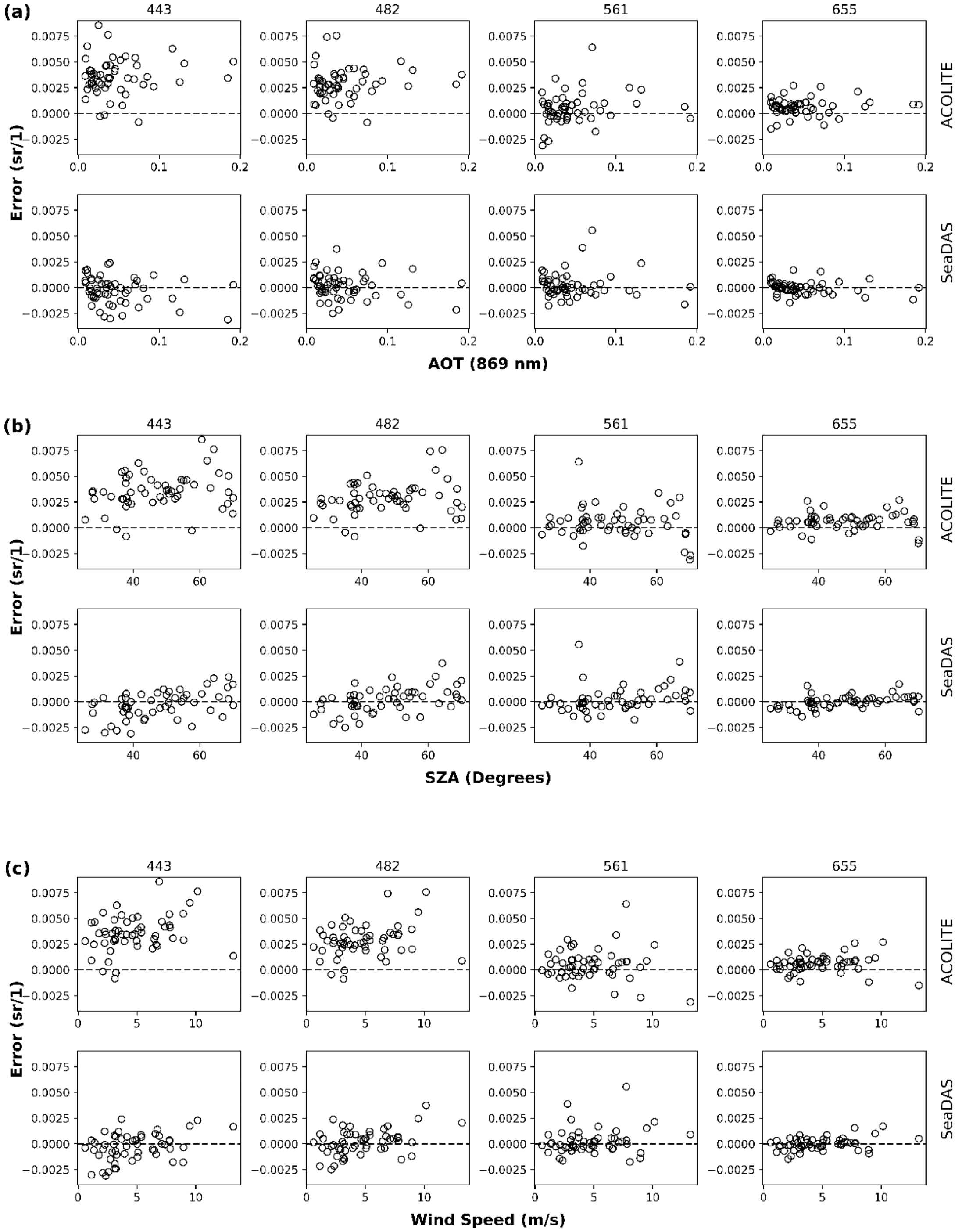

Figure 3.5. Scatterplots of the error (sr^{-1}) showing the dependency of R_{rs} retrieval accuracy from both ACOLITE and SeaDAS on (a) AOT(869), (b) SZA and (c) wind speed. AOT(869) and wind speed were derived from coincident measurements at each AERONET-OC site used in this study, while SZA was obtained by subtracting the sun elevation angle provided in the Landsat 8 metadata from 90°. Each circle represents a match-up data point, for a total of 54 data points across the 14 AERONET-OC site. The 54 match-ups and their corresponding environmental parameter values are tabulated in Supplemental Data 3C.

3.7. Conclusion

This chapter provides an evaluation of four atmospheric correction algorithms (ACOLITE, ARCSI, LaSRC and SeaDAS) for estimating R_{rs}. Fifty-four match-ups were used to test the performance of these algorithms over various coastal sites that form part of the AERONET-OC network. After accounting for spectral band differences in AERONET-OC and OLI measurements/products, the R_{rs} products from all algorithms were compared to AERONET in-situ R_{rs} data. Generic AC methods (ARCSI and LaSRC) are less accurate for deriving R_{rs} in coastal environments than water-based methods (ACOLITE and SeaDAS). Generic AC methods are particularly unreliable in the 443 and 482 nm channels, and performed well at only a few sites located in nearshore and inland waters. SeaDAS produced the best performance overall, while ACOLITE, though it performed better than the two generic AC methods, is less accurate than SeaDAS for R_{rs} retrievals over (mostly) low-to-moderately coastal waters such as those typical of the AERONET-OC sites. Analyses of differences in spectral bands between satellite and in-situ measurements reveal that band adjustment minimizes differences between sensors with different spectral bands. A relationship seems to exist between R_{rs} retrieval accuracy for the two water-based AC methods and two atmospheric variables: SZA and wind speed. Future studies should examine these relationships further, and consider related improvements to the AC methods. Neither of the water-based AC methods can currently be used to process images from commercial sensors such as WorldView-2/3 (which have improved spatial resolution) or previous Landsat missions (though this capability is available in an in-house version of SeaDAS for future public release). Given the usefulness of high spatial resolution data and the understanding that can be gained from time series analysis for aquatic studies, such improvements would be valuable. Our findings are primarily applicable to nearshore coastal waters. Further validation is required over inland waters (i.e., rivers, lakes, reservoirs) - and particularly in stations with few match-up points (e.g., GOT Seaprism and Lake Erie with one and two match-ups, respectively) - to better understand the performance of each AC method for various science and application areas. In future studies, the authors intend to (1) evaluate the performance of these AC algorithms over inland waters such as those found over the GloboLakes sites and (2) compare satellite-derived bathymetry products obtained from using the water-based AC algorithms.

3.8. References

1. Cracknell, A. P.; Newcombe, S.K.; Black, A.F.; Kirby, N.E. The ABDMAP (Algal Bloom Detection, Monitoring and Prediction) Concerted Action. *International Journal of Remote Sensing* **2001,** 22, 205–47. https://doi.org/10.1080/014311601449916.
2. Pe'eri, S.; Parrish, C.; Azuike, C.; Alexander, L.; Armstrong, A. Satellite Remote Sensing as a Reconnaissance Tool for Assessing Nautical Chart Adequacy and Completeness. *Marine Geodesy* **2014,** 37, 293–314. https://doi.org/10.1080/01490419.2014.902880.
3. Dekker, A. G.; Brando, V.E.; Anstee, J.M. Retrospective Seagrass Change Detection in a Shallow Coastal Tidal Australian Lake. *Remote Sensing of Environment* **2005**, 97, 415–33. https://doi.org/10.1016/j.rse.2005.02.017.
4. Mumby, P. J.; Green, E.P.; Edwards, A.J.; Clark, C.D. Coral Reef Habitat Mapping: How Much Detail Can Remote Sensing Provide? *Marine Biology* **1997,** 130, 193–202. https://doi.org/10.1007/s002270050238.
5. Gordon, H. R.; Wang, M. Retrieval of Water-Leaving Radiance and Aerosol Optical Thickness over the Oceans with SeaWiFS: A Preliminary Algorithm. *Applied Optics* **1994a,** 33, 443. https://doi.org/10.1364/AO.33.000443.
6. Antoine, D.; Morel, A. A Multiple Scattering Algorithm for Atmospheric Correction of Remotely Sensed Ocean Colour (MERIS Instrument): Principle and Implementation for Atmospheres Carrying Various Aerosols Including Absorbing Ones. *International Journal of Remote Sensing* **1999**, 20, 1875-1916. https://doi.org/10.1080/014311699212533.
7. Mobley, C. D.; Werdell, J.; Franz, B.; Ahmad, Z.; Bailey, S. Atmospheric Correction for Satellite Ocean Colour Radiometry. *A Tutorial and Documentation of the Algorithms*

Used by the NASA Ocean Biology Processing Group. **2016**, 1-73. https://oceancolor.gsfc.nasa.gov/docs/technical/NASA-TM-2016-217551.pdf

8. IOCCG. *Remote Sensing of Ocean Colour in Coastal, and Other Optically-Complex, Waters.* Sathyendranath, S., Ed.; Reports of the International Ocean-Colour Coordinating Group (IOCCG); IOCCG: Dartmouth, NS, Canada, 2000**.**
9. Siegel, D.A.; Wang, M.; Maritorena, S.; Robinson, W. Atmospheric Correction of Satellite Ocean Colour Imagery: The Black Pixel Assumption. *Applied Optics* **2000**, 39, 3582–91. https://doi.org/10.1364/AO.39.003582.
10. Shi, W.; Wang, M. An Assessment of the Black Ocean Pixel Assumption for MODIS SWIR Bands. *Remote Sensing of Environment* **2009,** 113, 1587–97. https://doi.org/10.1016/j.rse.2009.03.011.
11. Wang, M.; Shi, W. The NIR-SWIR Combined Atmospheric Correction Approach for MODIS Ocean Colour Data Processing. *Optical Express* **2007,** 15, 15722–33. https://doi.org/10.1364/OE.15.015722.
12. Bailey, S. W.; Franz, B. A.; Werdell. P. J. Estimation of Near-Infrared Water-Leaving Reflectance for Satellite Ocean Colour Data Processing. *Optical Express* **2010**, 18, 7521–27. https://doi.org/10.1364/OE.18.007521.
13. Goyens, C.; Jamet, C.; Schroeder, T. Evaluation of Four Atmospheric Correction Algorithms for MODIS-Aqua Images over Contrasted Coastal Waters. *Remote Sensing of Environment* **2013**, 131, 63–75. https://doi.org/10.1016/j.rse.2012.12.006.
14. Jamet, C.; Loisel, H.; Kuchinke, C. P.; Ruddick, K.; Zibordi, G.; Feng, H. Comparison of three SeaWiFS atmospheric correction algorithms for turbid waters using AERONET-OC measurements. *Remote Sensing of Environment* **2011**, 115, 1955–1965. https://doi.org/10.1016/j.rse.2011.03.018
15. Pahlevan, N.; Schott, J.R.; Franz, B.A.; Zibordi, G.; Markham, B.; Bailey, S.; Schaaf, C.B.; Ondrusek, M.; Gren, S.; Strait, C.M. Landsat 8 remote sensing reflectance (Rrs) products: Evaluations, intercomparisons, and enhancements. *Remote Sensing of Environment* **2017**, 190, 289–301.
16. Pahlevan, N.; Lee, Z.; Wei, J.; Schaaf, C.B.; Schott, J.R.; Berk, A. On-orbit radiometric characterization of OLI (Landsat-8) for applications in aquatic remote sensing. *Remote Sensing of Environment* **2014**, 154, 272–284.
17. Hedley, J.; Roelfsema, C.; Koetz, B.; Phinn, S. Capability of the Sentinel 2 Mission for Tropical Coral Reef Mapping and Coral Bleaching Detection. *Remote Sensing of Environment* **2012**, 120, 145–55. https://doi.org/10.1016/j.rse.2011.06.028.

18. Franz, B.A.; Bailey, S.; Kuring, N.; Werdell, P.J. Ocean Colour Measurements with the Operational Land Imager on Landsat-8: Implementation and Evaluation in SeaDAS. *Journal of Applied Remote Sensing* **2015**, 9, 096070. https://doi.org/10.1117/1.JRS.9.096070.
19. Doxani, G.; Vermote, E.; Roger, J.; Gascon, F.; Adriaensen, S.; Frantz, D.; Hagolle, O.; Hollstein, A.; Kirches, G. Atmospheric Correction Inter-Comparison Exercise. *Remote Sensing* **2018**, 10, 1–18. https://doi.org/10.3390/rs10020352.
20. Wei, J.; Lee, Z.; Garcia, R.; Zoffoli, L.; Armstrong, R.A.; Shang, Z.; Sheldon, P.; Chen, R.F. An assessment of Landsat-8 atmospheric correction schemes and remote sensing reflectance products in coral reefs and coastal turbid waters. *Remote Sensing of Environment* **2018**, *215, 18-32. https://doi.org/10.1016/j.rse.2018.05.033.*
21. Clewley, D.; Bunting, P.; Shepherd, J.; Gillingham, S.; Flood, N.; Dymond, J.; Lucas, R.; Armston, J.; Moghaddam, M. A Python-Based Open Source System for Geographic Object-Based Image Analysis (GEOBIA) Utilizing Raster Attribute Tables. *Remote Sensing* **2014**, 6, 6111–35. https://doi.org/10.3390/rs6076111.
22. Vanhellemont, Q.; Ruddick, K. Turbid Wakes Associated with Offshore Wind Turbines Observed with Landsat 8. *Remote Sensing of Environment* **2014a**, 145, 105–15. https://doi.org/10.1016/j.rse.2014.01.009.
23. USGS. Product Guide: Landsat 8 Surface Reflectance Code (LASRC) Product. 2017. https://doi.org/10.1080/1073161X.1994.10467258
24. Vermote, E.F.; Justice, C.; Claverie, M.; Franch, B. Preliminary Analysis of the Performance of the Landsat 8/OLI Land Surface Reflectance Product. *Remote Sensing of Environment* **2016**, 185. Elsevier B.V.: 46–56. https://doi.org/10.1016/j.rse.2016.04.008.
25. Gerace, A. D.; Schott, J.R.; Nevins, R. Increased Potential to Monitor Water Quality in the Near-Shore Environment with Landsat's next-Generation Satellite. *Journal of Applied Remote Sensing* **2013**, 7, 073558. https://doi.org/10.1117/1.JRS.7.073558.
26. Zibordi, G.; Holben, B.; Slutsker, I.; Giles, D.; D'Alimonte, D.; Mélin, H.; Berthon, J.F. AERONET-OC: A Network for the Validation of Ocean Colour Primary Products. *Journal of Atmospheric and Oceanic Technology* **2009**, 26, 1634–51. https://doi.org/10.1175/2009JTECHO654.1.
27. Holben, B. N.; Tanré, D.; Smirnov, A.; Eck, T. F.; Slutsker, I.; Abuhassan, Newcomb, W. W.; Schafer, J.S.; Chatenet, B.; Lavenu, F. An Emerging Ground-Based Aerosol

Climatology: Aerosol Optical Depth from AERONET. *Journal of Geophysical Research* **2001**, 106, 12067. https://doi.org/10.1029/2001JD900014.

28. Holben, B. N.; Eck, T. F.; Slutsker, I.; Tanré, D.; Buis, J. P.; Setzer, A.; Vermote, E.; Reagan, J.A.; Kaufman, T.; Nakajima, F. AERONET - A Federated Instrument Network and Data Archive for Aerosol Characterization. *Remote Sensing of Environment* **1998**, 66, 1–16. https://doi.org/10.1016/S0034-4257(98)00031-5.
29. Thuillier, G.; Hersé, M.; Simon, P.C.; Labs, D.; Mandel, H.; Gillotay, D.; Foujols, T. The Solar Spectral Irradiance from 200 to 2400 nm as Measured by the SOLSPEC Spectrometer from the ATLAS and EURECA Missions. *Solar Physics* **2003**, 214, 1–22. Available online: https://oceancolor.gsfc.nasa.gov/docs/rsr/f0.txt (accessed on 22 December 2018).
30. Bailey, S.; Franz, A.; Werdell, J. A Multi-Sensor Approach for the on-Orbit Validation of Ocean Colour Satellite Data Products. *Remote Sensing of Environment* **2006**, 102, 12–23. https://doi.org/10.1016/j.rse.2006.01.015.
31. Wicks, D. J.; Jarman, M. S2 ARD Project Briefing Document. 2017. Available online: https://media.sa.catapult.org.uk/wp-content/uploads/2017/09/14123619/Sentinel-2-ARD-Project-Summary_final.pdf. (accessed on 22 February 2018).
32. Wilson, R. T. Py6S: A Python Interface to the 6S Radiative Transfer Model. *Computers and Geosciences* **2013**, 51: 166–71. https://doi.org/10.1016/j.cageo.2012.08.002.
33. Vermote, E. F.; Tanré, D.; Deuzé, J.L.; Herman, M.; Morcrette, J.J. Second Simulation of the Satellite Signal in the Solar Spectrum, 6S: An Overview. *IEEE Transactions on Geoscience and Remote Sensing* **1997**, 35, 675–86. https://doi.org/10.1109/36.581987.
34. Vanhellemont, Q.; *Ruddick, K. Landsat-8 As a Precursor to Sentinel-2: Observations of Human Impacts in Coastal Waters*. Proceedings of the Sentinel-2 for Science Workshop. 2014b. ESA Special Publication SP-726.
35. Shettle, E. P.; Fenn, R. W. Models for the Aerosols of the Lower Atmosphere and the Effects of Humidity Variations on Their Optical Properties. *Environmental Research Papers* **1979**, *676*, 89. https://doi.org/10.1109/TR.1987.5222381.
36. Ruddick, K.G.; Ovidio, F.; Rijkeboer, M. Atmospheric Correction of SeaWiFS Imagery for Turbid Coastal and Inland Waters. *Applied Optics* **2000**, 39, OSA: 897–912. https://doi.org/10.1364/AO.39.000897.

37. Vanhellemont, Q.; Ruddick, K. *Acolite for sentinel-2 : Aquatic applications of MSI imagery*. Proceedings of the 2016 ESA Living Planet Symposium. 2016. ESA Special Publication SP-740.
38. Wang, Y.; Liu, L.; Hu, Y.; Li, D.; Li, Z.; Wang, Y. Development and Validation of the Landsat-8 Surface Reflectance Products Using a MODIS-Based per-Pixel Atmospheric Correction Method Atmospheric Correction Method. *International Journal of Remote Sensing* **2016**, 37, 1291–1314. https://doi.org/10.1080/01431161.2015.1104742.
39. Wang, Z.; Erb, A.M.; Schaaf, C.B.; Sun, Q.; Liu, Y.; Yang, Y.; Shuai, Y.; Casey, K.A.; Román, M.O. Early Spring Post-Fire Snow Albedo Dynamics in High Latitude Boreal Forests Using Landsat-8 OLI Data. *Remote Sensing of Environment* **2015**, 185. 71–83. https://doi.org/10.1016/j.rse.2016.02.059.
40. Vuolo, F.; Mattiuzzi, M.; Atzberger, C. Comparison of the Landsat Surface Reflectance Climate Data Record (CDR) and Manually Atmospherically Corrected Data in a Semi-Arid European Study Area. *International Journal of Applied Earth Observation and Geoinformation* **2015**, 42, 1–10. https://doi.org/10.1016/j.jag.2015.05.003.
41. Feng, M.; Sexton, J.O.; Huang, C.; Masek, J.G.; Vermote, E.F.; Gao, F.; Narasimhan, R.; Channan, S.; Wolfe, R.E.; Townshend, J.R. Global Surface Reflectance Products from Landsat: Assessment Using Coincident MODIS Observations. *Remote Sensing of Environment* **2013**, 134. 276–93. https://doi.org/10.1016/j.rse.2013.02.031.
42. Ahmad, Z.; Franz, B.; McClain, C.; Kwiatkowska, E.; Werdell, J.; Shettle, E.; Holben, B. New Aerosol Models for the Retrieval of Aerosol Optical Thickness and Normalized Water-Leaving Radiances from the SeaWiFS and MODIS Sensors over Coastal Regions and Open Oceans. *Applied Optics* **2010**, 49, 5545-556. https://doi.org/10.1364/AO.49.005545.
43. Gordon, H. R.; Wang, M. Influence of Oceanic Whitecaps on Atmospheric Correction of Ocean-Colour Sensors. *Applied Optics* **1994b**, 33, 7754. https://doi.org/10.1364/AO.33.007754.
44. Pahlevan, N.; Smith, B.; Binding, C.; O'Donnell, D. M. Spectral Band Adjustments for Remote Sensing Reflectance Spectra in Coastal/Inland Waters. *Optical Express* **2017b**, 25, 23. 28650–67. https://doi.org/10.1364/OE.25.028650.
45. Mélin, F.; Sclep, G. Band Shifting for Ocean Colour Multi-Spectral Reflectance Data. *Optics Express* **2015**, 23, 2262–79. https://doi.org/10.1364/OE.23.002262.

46. Pahlevan, N., Roger, J.; Ahmad, Z. Revisiting short-wave-infrared (SWIR) bands for atmospheric correction in coastal waters. *Optics Express* **2107c**, 25, 6015-6035. https://doi.org/10.1364/OE.25.006015
47. Vanhellemont, Q.; Ruddick, K. Advantages of high quality SWIR bands for ocean colour processing: Examples from Landsat-8. *Remote Sensing of Environment* **2015**, 161, 89-106. https://doi.org/10.1016/j.rse.2015.02.007.
48. De Maerschalck, B.; Vanlede, J. Zeebrugge Harbour Sediment Transport Model. *Coastal Dynamics* **2013**, 477–86.
49. Amin, R.; Gilerson, A.; Zhou, J.; Gross, B.; Moshary, F.; Ahmed, S. *Impacts of Atmospheric Corrections on Algal Bloom Detection Techniques.* Eighth Conference on Coastal Atmospheric, Oceanic Prediction, Processes, USA, 2009.
50. Mobley, C. D. Estimation of the Remote-Sensing Reflectance from above-Surface Measurements. *Applied Optics* **1999**, 38, 7442. https://doi.org/10.1364/AO.38.007442.
51. Kaufman, Y. J. Aerosol Optical Thickness and Atmospheric Path Radiance. *Journal of Geophysical Research* **1993***,* 98: 2677–92. https://doi.org/10.1029/92JD02427.
52. Zibordi, G.; Mélin, F.; Berthon, J.F. Comparison of SeaWiFS, MODIS and MERIS radiometric products at a coastal site. *Geophysical Research Letters* **2006**, 33, 1–4. https://doi.org/10.1029/2006GL025778.
53. Vanhellemont, Q.; Bailey, S.; Franz, B.; Shea, D. Atmospheric Correction of Landsat-8 Imagery Using Seadas. In Proceedings of the Sentinel-2 for Science Workshop, Frascati, Italy, 20–23 May 2014.

Chapter 4. An approach to minimize atmospheric correction error and improve physics-based satellite derived bathymetry in a coastal environment

This chapter is currently under review in Remote Sensing

Citation details: Christopher O. Ilori and Anders Knudby (2019): An approach to minimize atmospheric correction error and improve physics-based satellite derived bathymetry in a coastal environment.

4.1. Abstract

Physics-based radiative transfer model inversion methods have been developed and implemented for satellite-derived bathymetry (SDB); however, precise atmospheric correction (AC) is required for robust bathymetry retrieval. In a previous study we revealed that biases from atmospheric correction may be related to imaging and environmental factors (such as wind speed, aerosol optical properties and solar zenith angle) that are not considered sufficiently in all atmospheric correction algorithms. Thus, the main aim of this study is to demonstrate how atmospheric correction biases related to environmental factors can be minimized to improve SDB results. To achieve this, we first tested a physics-based inversion method to estimate bathymetry for a nearshore area in the Florida Keys, USA. Using a freely available water-based AC algorithm (ACOLITE), we used Landsat 8 (L8) images to derive per-pixel remote sensing reflectances, from which bathymetry was subsequently estimated. We then quantified known biases in the atmospheric correction using a linear regression that estimated bias as a function of imaging and environmental factors, and applied a correction to produce a new set of remote sensing reflectances. This correction improved bathymetry estimates for seven of the nine scenes we tested, with the resulting changes in bathymetry RMSE ranging from +0.29m (worse) to -0.53m (better). In addition, we showed that an ensemble approach based on multiple images, with acquisitions ranging from optimal to sub-optimal conditions, can be used to estimate bathymetry with a result that is similar to what can be obtained from the best individual scene. This approach can reduce time spent on pre-screening and filtering of scenes. The correction method implemented in this study is not a complete solution to the challenge of atmospheric correction for satellite-derived bathymetry, but can eliminate the effects of biases inherent to individual AC algorithms and thus improve bathymetry retrieval. It may also be beneficial for use with other AC algorithms, and for estimation of seafloor habitat and water quality products, though further validation in different nearshore waters is required.

Keywords: satellite-derived bathymetry; physics-based inversion method; atmospheric correction

4.2. Introduction

Bathymetric information from satellite data is of fundamental importance in optically shallow waters, where the seafloor is visible from space and the water-leaving radiance is influenced by reflection off the seafloor. Such information, in the form of maps of water depth, is essential for a wide variety of purposes including offshore activities (e.g., pipeline laying), resource management (e.g., fishery), and defense operations (e.g., navigation). Traditional bathymetric charts are based on soundings obtained during hydrographic surveys. However, as ship-borne surveys are costly and time-consuming, and many shallow-water environments are highly dynamic, it is impossible to survey all areas of interest, and the difficulty in accessing shallow and remote areas means that in practice up-to-date data are typically only available for limited areas (harbors and main navigation corridors). Airborne LiDAR Bathymetry (ALB) systems, such as SHOALS [1], Section LADS [2], and EAARL [3] can also be used to map water depth. With these techniques, vertical accuracy of about ±15 cm in shallow water is possible [4], although accuracy is affected by turbidity and the LiDAR system. While precise bathymetric mapping of water depth to about 20 - 70 m depth can be achieved with airborne LiDAR [5,6], costs associated with these systems are relatively high, thus limiting their application over large, or remote, areas.

Passive optical satellite remote sensing can also be used to map bathymetry, typically known as satellite-derived bathymetry (SDB), based on the relationship between the colour of a shallow-water area and the depth of water. SDB can be implemented using empirical or physics-based methods. The empirical methods are based on the simple premise that a statistical relationship can be established between water depth and the remotely sensed radiance of a water body, using regression or similar analysis [2,7,8,9,10]. All empirical approaches thus require coincident in-situ data on water depth for calibration; ideally these data should be up to date and have good geographic and depth distribution. Empirical approaches assume that the inherent optical properties (IOPs) of the water, as well as seafloor spectral reflectance, do not vary across the image, and results may therefore contain large errors and require manual editing when this is not the case. A key advantage of empirical approaches is the ability to retrieve water depth relatively easily, but their reliance on calibration from coincident field observations and the need of knowledge about the bottom features mean that they cannot be used for systematic regional and global mapping and monitoring. Physics-based methods instead estimate bathymetry on per-pixel basis through inversion of a radiative transfer model (RTM). As such, they do not assume uniform IOPs and seafloor reflectance, nor do they rely on coincident depth data for calibration. In addition to bathymetry, seafloor reflectance and water IOPs, which can be used to infer substrate and water quality respectively, can be simultaneously retrieved, and per-pixel uncertainties of all these parameters, including water depth, can also be determined. While originally developed for and tested on airborne hyperspectral imagery, physics-based methods for SDB have also been demonstrated for multispectral satellite sensors [11,12,13,14]. Physics-based methods can be implemented using either look-up tables (LUTs) [15,16] or semi-analytical optimization methods [17,18]. In the first case, a database of remote sensing reflectance (R_{rs}) spectra is built from a radiative transfer model provided with a range of values for water depth, spectral seafloor reflectance, water column optical properties (absorption and backscattering coefficients), and known environmental conditions such as sun angle and wind speed. For retrieval of parameters (water depth, water IOPs, and seafloor reflectance) in each image pixel, a search is then performed to find the R_{rs} in the LUT that best matches the one observed in the pixel [15]. With semi-analytical optimization methods, the radiative transfer equation is used to estimate water depth by iterative optimization of the same parameters. In both methods, the best match between modeled and observed reflectance is determined using a least squares or similar matching technique.

Despite the advantages of physics-based methods, a substantial challenge is that they rely on precise estimates of absolute radiometry, typically in the form of R_{rs} or water-leaving radiance (L_w). Unlike other optical remote sensing applications, including the empirical approaches to satellite-derived bathymetry, physics-based retrieval algorithms may perform very poorly if R_{rs} is incorrectly estimated, and high-quality R_{rs} data from a robust atmospheric correction (AC) is essential for accurate physics-based water depth estimation. Accordingly, a variety of AC algorithms have been developed for ocean colour (OC) products retrieval such as bathymetry, and several studies have validated their performance against in-situ data. For example, Pahlevan et al. (2017) [19] validated R_{rs} produced from different AC schemes in the Sea-Viewing Wide Field-of-View Sensor (SeaWiFS) Data Analysis System (SeaDAS) with in-situ data from the AERONET-OC network. Likewise, Doxani et al. (2018) [20] assessed the performance of different AC methods and validated their R_{rs} with match-up datasets over both land and water surfaces in an AC inter-comparison exercise. Warren et al. (2019) [21] evaluated the accuracy of a wide range of freely available AC processors by comparing them to reference R_{rs} data from different coastal and inland waters. Similarly, in a more recent AC exercise, Zhang & Hu (2020) [22] also analyzed an AC algorithm, comparing its R_{rs} images with those measured over few sites from the AERONET-OC stations. Collectively these studies demonstrate that accurate AC remains a challenge for OC remote sensing where precise R_{rs} data are needed. It is therefore important to explore ways by which errors in AC outputs, and their effect on products derived from them, can be minimized. One way to address some of the problems posed by imprecise atmospheric correction is to assess and quantify the impacts of environmental variables on AC accuracy and then account for this in the atmospherically corrected image. In an earlier study [23], four publicly available AC processors (2 land-based and 2 water-based) for deriving the R_{rs} in coastal waters were compared and validated with 54 R_{rs} match-up datasets from AERONET-OC stations. The study revealed that biases from ACOLITE and SeaDAS, two of the state-of-the-art AC algorithms, are influenced by environmental variables. In this study, we demonstrated the potential of Landsat 8 (L8) data for SDB in US coastal waters and assessed the performance of a commonly used and publicly available water-based AC algorithm (ACOLITE: [24]) for physics-based SDB. To minimize the effect of imperfect atmospheric correction on the bathymetry retrieval, we further used a correction factor to improve the original atmospherically corrected image from ACOLITE. Using a set of 9 images, SDB estimates from these two AC procedures were then compared with lidar-derived bathymetry of the area. Lastly, we used an ensemble approach to produce SDB of the study area using all the corrected images.

4.3. Study Sites and Imagery

4.3.1. Study sites

The Florida Keys is a series of islands that extend from the southern end of Florida, USA, to the south-southwest. Their nearshore shallow waters include coral reef tracts, patch reefs, bank reefs, seagrass meadows and unvegetated hard and soft bottom. This site was chosen because of its relatively clear waters, the good knowledge of seabed features and availability of lidar-derived depth data for validating SDB estimates of water depth. The section of the Florida Keys used in this study is presented in Figure 4.1, along with the distribution of bathymetric lidar data for the area.

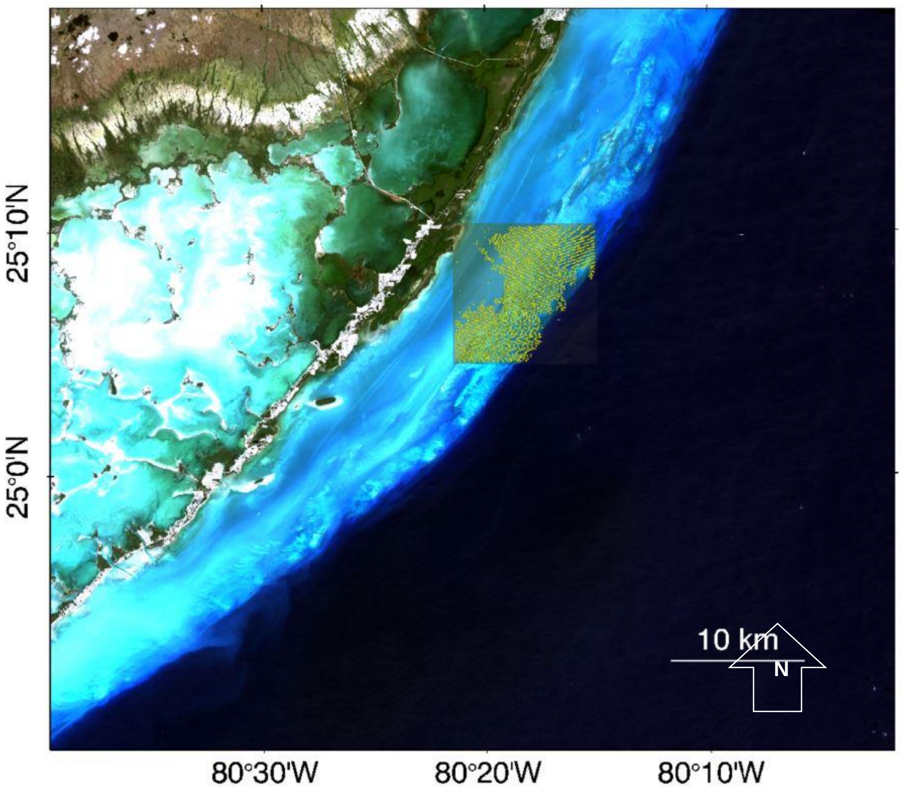

Figure 4.1. Landsat 8 image showing the upper Florida Keys. Bathymetric lidar data used for validation are shown in yellow.

4.3.2. Satellite data

Nine L8 images (Figure 4.2) from the Florida Keys, acquired during both optimal and near-optimal conditions for SDB, were downloaded from the archive of the United States

Geological Survey after visually inspecting all available images from May 2013 to May 2019. L8 OLI (Operational Land Imager) collects visible, NIR and SWIR spectral band imagery at 30 m spatial resolution. In addition to the improved positional accuracy of 14 m, compared to 50 m for its predecessors in the Landsat series, L8 includes coastal and aerosol (433-453 nm) and blue (450-515 nm) bands for coastal and bathymetric mapping [25,26].

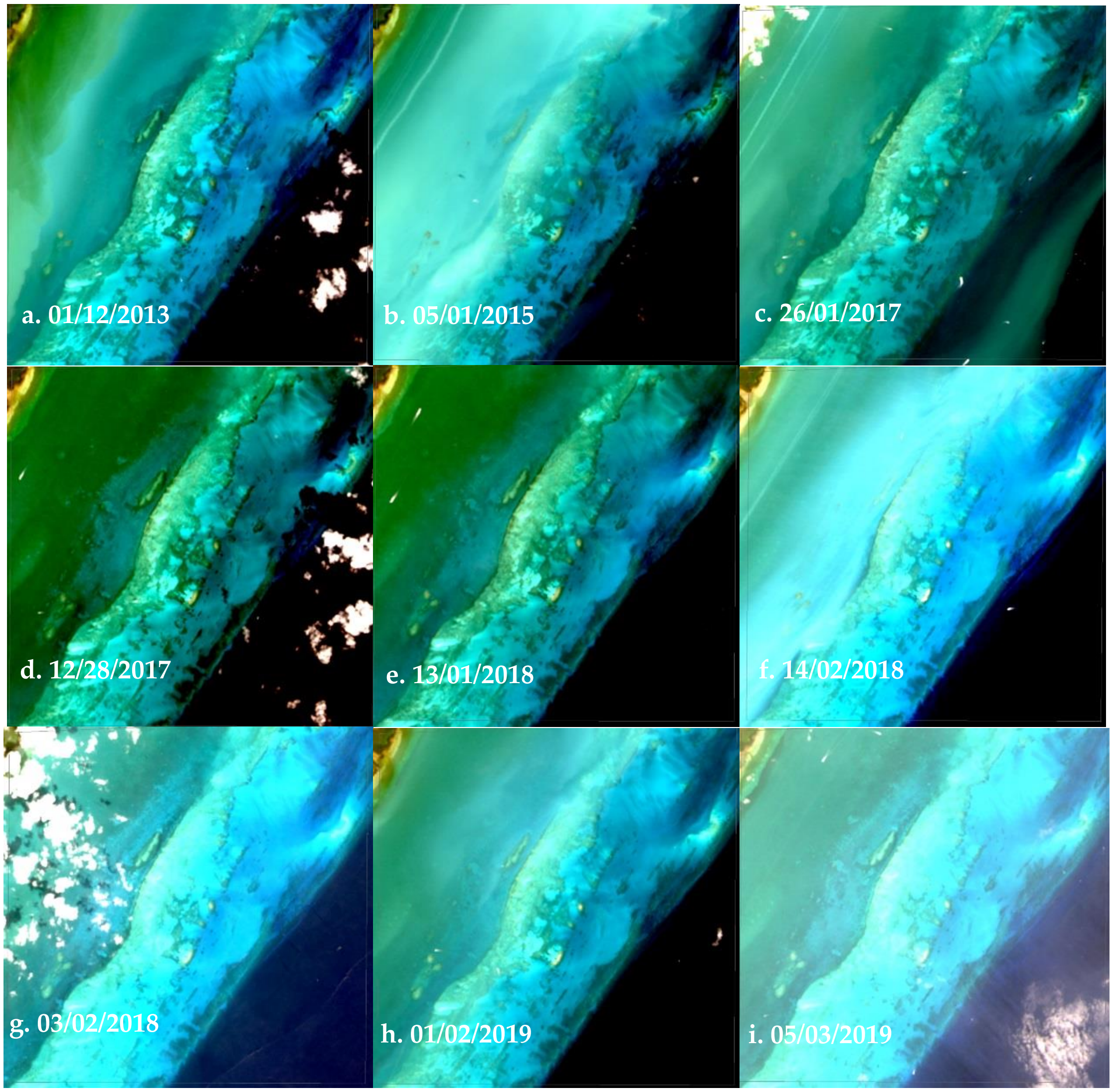

Figure 4.2. **A section of Florida Keys image showing the RGB composite of each image used in this study and the validation area (red square)**

4.3.3. Lidar data

Bathymetric LiDAR data were acquired for the study site from the National Oceanic and Atmospheric Administration (NOAA) Office for Coastal Management's Digital Coast (https://coast.noaa.gov/digitalcoast/), in raster format with a spatial resolution of 0.3 m. A portion of the collection covering the Florida Keys coastal area was referenced to mean sea level and resampled to 30 m to match the spatial resolution of L8 (Figure 4.1).

4.4. Methodology

4.4.1. Data preprocessing

Atmospheric correction

We implemented two types of AC methods for water depth retrieval: (1) we used ACOLITE to process L8 images into R_{rs} values (henceforth Rrs_{raw}), and (2) then applied a correction factor to reduce errors in the original ACOLITE output and create new corrected R_{rs} values (henceforth $Rrs_{corrected}$). ACOLITE [25], specifically designed for AC over water surfaces, is an AC method that estimates water-leaving radiance by simulating contributions from molecular (Rayleigh) and particulate (aerosol) scattering using a 6SV-based look-up table [27]. Based on Ruddick et al. (2000) [28], aerosol reflectance is estimated by determining a per-tile aerosol type (or epsilon) from the ratio of reflectances in two bands over water pixels where water-leaving reflectance can be assumed to be zero. The epsilon is then used to extrapolate the observed aerosol reflectance to the visible bands to remove atmospheric contributions. ACOLITE was originally designed for processing L8 images, but has been modified and updated to also process Sentinel-2 data [29]. Furthermore, the most recent version, which can be adapted to commercial sensors such as Pleiades, contains an additional AC scheme (now the default setting) called the dark spectrum fitting (DSF) algorithm, as well as a sun glint correction scheme [30]. In this study ACOLITE (version 20170113.0) was used to produce all R_{rs} images, which are the direct input into the bathymetry algorithm. The default SWIR option (1609 and 2201 nm band combination) was implemented for all images. This band combination takes advantage of the longest-wavelength SWIR band, where water absorption is the highest. In a previous study [23], in which a range of atmospheric correction algorithms were compared and validated against in-situ water-leaving radiance from 14 AERONET-OC stations, statistically significant relationships were demonstrated between errors in ACOLITE's R_{rs} estimates for L8's 443 nm and 482 nm bands and three environmental variables – Solar Zenith Angle (SZA), Aerosol Optical Thickness (AOT) at 865 nm (AOT_{865}) and wind speed (u_{10}); probable but statistically non-significant relationships were also demonstrated for the 561 nm and 655 nm bands. Using multiple linear regression, we therefore derived a set of coefficients that were used to estimate the error of ACOLITE's R_{rs} estimates for each of those four bands in each image, as a function of SZA, AOT_{865} and wind speed. Each of the four bands used for depth retrieval in this study was then corrected using Equation 1:

$$Rrs_{corrected} = Rrs_{raw} - (a + b*SZA + c*AOT_{865} + d*u10) \tag{4.1}$$

where $Rrs_{corrected}$ and Rrs_{raw} are the R_{rs} images with and without correction respectively; and a, b, c and d are coefficients obtained through fitting a linear model to the data from Ilori et al. (2019) [23]. SZA was obtained from the metadata of each L8 scene. AOT_{865} was processed and obtained using the l2gen processor in the SeaDAS software, and an average value used for each image was calculated by randomly sampling multiple pixels over the area of the study site. Wind speed data was obtained from the National Centers for Environmental Prediction Reanalysis project [31], where 6-hour global wind speed estimates are archived. Table 4.1 presents the value of each environmental parameter for each image used in this study.

Table 4.1. Environmental parameter variables for each image.

Scene date (dd/mm/yyyy)	SZA (degrees)	AOT_{865}	u_{10} (m/s)
01/12/2013	50.36	0.081	5.29
05/01/2015	52.79	0.088	1.07
26/01/2017	50.13	0.083	2.49
28/12/2017	52.98	0.076	6.45
13/01/2018	52.14	0.142	3.11
14/02/2018	45.63	0.12	4.84
02/03/2018	40.66	0.11	3.21
01/02/2019	49.02	0.122	3.74
05/03/2019	39.74	0.143	4.67

Sun glint correction

As sun glint correction is not inherently part of the ACOLITE version used in this study, we implemented the NIR method [32] to remove specular reflection off the sea surface for images where glint was visually obvious. This method assumes that for optically deep areas (where radiation reflected from the seafloor has negligible influence on L_w) any remaining NIR signal after atmospheric correction must be due to sea surface reflection. Glint intensity and removal is thus performed by establishing a linear relationship between the NIR and visible bands over an optically deep area in the image, and that relationship is then used across all water pixels to reduce R_{rs} for the visible bands to its assumed glint-free value.

4.4.2. Estimation of noise equivalent reflectance

Bathymetry model inversion based on least squares optimization techniques is generally sensitive to environmental noise [33,34], thus high $NE\Delta R_{rs}$ may make images unsuitable for bathymetry extraction. Following atmospheric correction, we therefore estimated the noise-equivalent difference in reflectance, $NE\Delta R_{rs}$ (sr^{-1}) [35], based on the methodology of Wettle et al. (2004) [36]. A 33 x 33-pixel window was selected over an optically deep homogeneous area, and the band-wise standard deviation of R_{rs} calculated (Table 4.2). Ideally, the $NE\Delta R_{rs}$ should be lower than 0.00025 sr^{-1} in each of the visible bands, with the exception of the blue band [37], which was the case for all nine images used in this study.

Table 4.2. The noise equivalent difference in reflectance ($NE\Delta R_{rs}$), computed from a kernel of 33 X 33 pixels from optically deep and homogeneous area, for each image used in this study.

Dates	Band 1	Band 2	Band 3	Band 4
01/12/2013	0.000200	0.000154	0.000096	0.000061
05/01/2015	0.000136	0.000108	0.000084	0.000063
26/01/2017	0.000092	0.000072	0.000057	0.000042
28/12/2017	0.000151	0.000105	0.000081	0.000053
13/01/2018	0.000111	0.000103	0.000069	0.000047
14/02/2018	0.000157	0.000129	0.000108	0.000063
02/03/2018	0.000126	0.000110	0.000069	0.000043
01/02/2019	0.000148	0.000127	0.000100	0.000063
05/03/2019	0.000086	0.000081	0.000059	0.000042

4.4.3. Parameterization of environmental properties

To implement the physics-based approach to SDB, values of optical properties and substratum spectral reflectance that are representative of the environment in question are needed. Water IOP (P_{440}, G_{440}, and X_{550}) parameterization for forward modelling for each site was based on assessment from Level 3 OC products from the VIIRS Generalized Inherent Optical Property (GIOP) algorithms [38]. P_{440} is the phytoplankton absorption coefficient at 440 nm, G_{440} is the absorption of gelbstoff and detrital materials coefficient at 440 nm, and X_{550} is the particulate backscattering of suspended particles coefficient at 550 nm. Using parameter values obtained from these OC products, ranges of values for each parameter were determined by observing the lowest and highest parameter values for all dates from GIOVANNI, an online visualization tool for OC products [39]. Values slightly lower and higher than the observed lowest and highest values, respectively, were then chosen (Table 4.3). As part of the inversion model, seafloor reflectance spectra are also needed. We used two seafloor spectra (Figure 4.3), based on the area's benthic description [40].

Table 4.3. Parameter ranges used for forward modelling.

P (mg m^{-3})	G (m^{-1})	X (m^{-1})	Z (m)
0.006 - 0.04	0.004 - 0.04	0.0005 - 0.006	0.1 - 30

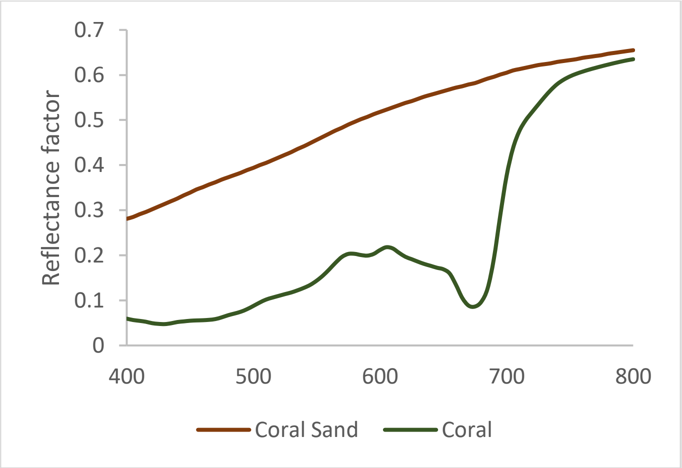

Figure 4.3. Spectra of the seafloor reflectance of Florida Keys.

4.4.4. Forward modelling of remote sensing reflectance

To derive water depth, we applied a modified version of the semi-analytical inversion model of Lee et al. (1988; 1989) [17,18] to the atmospherically corrected images. In this inversion scheme, the sub-surface remote sensing reflectance, r_{rs}, (the ratio of upwelling radiance to downwelling irradiance just below the surface) is related to absorption (a) and backscattering properties (b_b) of the water column, the seafloor reflectance (ρ) and water depth (H). For nadir-viewing satellites, the model can be expressed as:

$$R_{rs} \approx \frac{0.5 r_{rs}}{1-1.5 r_{rs}} \tag{4.2}$$

where r_{rs}, the subsurface remote-sensing reflectance, is expressed as:

$$r_{rs}(a, b_{b,} H, \rho) \approx (0.084 + 0.170u)u\left(1 - exp\left\{-\left[\frac{1}{\cos(\theta_w)} + \frac{1.03\sqrt{1+2.4u}}{\cos(\theta_v)}\right]kH\right\}\right) + \frac{\rho}{\pi} exp\left\{-\left[\frac{1}{\cos(\theta_w)} + \frac{1.04\sqrt{1+5.4u}}{\cos(\theta_v)}\right]kH\right\} \tag{4.3}$$

$$u = \frac{b_b}{\mathrm{a} + b_b} \tag{4.4}$$

$$k = \mathrm{a} + \mathrm{b_b} \tag{4.5}$$

where θ_w and θ_v are the sub-surface solar zenith and sub-surface sensor viewing angles, respectively. Absorption (a) and backscattering coefficients (b_b) are functions of 1) the absorption coefficient of phytoplankton at 440 nm, P; 2) the absorption coefficient of colored dissolved materials at 440 nm, G; and 3) the backscattering coefficient of suspended particles at 550 nm, X. These are expressed as:

$$a = a_w + P{a^*}_{phy} + Ge^{-0.015(\lambda-440)} \tag{4.6}$$

$$b_b = b_{bw} + X\left[\frac{550}{\lambda}\right]^{Y} \tag{4.7}$$

where a_w and b_{bw} are the absorption and backscattering coefficients of pure water respectively [41], $a^*{}_{phy}$ is the specific absorption of coefficient of phytoplankton (normalized to a value of 1.0 at 440 nm), λ is the centre wavelength and Y is the spectral shape that depends on the particulate shape and size.

While Lee's inversion model uses albedo of only one key benthic substrate (sand), our model includes a parameterization to set the seafloor reflectance as a linear mix of the two bottom types. To reduce computing time, forward modelling was performed using the adaptive look-up table (ALUT) method [11,16]. Using realistic extreme values of all environmental parameters, this procedure uses a hierarchically-structured look up table (LUT) to efficiently cover the range of expected R_{rs} values while minimizing over-sampling of spectrally similar regions of environmental space. This look-up-table approach requires bounded ranges for all the modelled parameters, for which we used the value ranges in Table 4.3.

4.4.5. Inversion of remote sensing reflectance

Model inversion was subsequently performed using the binary space partitioning (BSP) approach [11,16], as described in [12]. Briefly, this technique subdivides the LUT created during forward modelling into different nodes. First, the BSP splits the whole LUT into two (left and right child nodes) and subsequently subdivides the nodes into a partitioning tree which facilitates the optimization of the per-pixel LUT search. After model inversion and depth retrieval, water depths were corrected for tidal height at the time of each image acquisition using tidal height estimates obtained from Oregon State University's tide prediction service [42]. Both the forward modelling and inversion were implemented using python codes.

4.4.6. Validation of depth estimates

Validation of depth estimates from the two atmospheric correction procedures was performed by comparing the estimated depths to the LiDAR data. The number of depth estimates used for validation (Table 4.4) varied between the nine images due to differences in the number of pixels for which depth was successfully estimated, as pixels which did not pass the AC's internal quality checks (e.g. due clouds), pixels with negative depths, and pixels that were visually impacted by boats, wake, or cloud shadows, were eliminated prior to validation. Based on the remaining pixels, we used the correlation coefficient (R^2), RMSE (root-mean-squared-error) (Equation 8) and bias (Equation 9) to compare the accuracy of the uncorrected and corrected SDB estimates with the LiDAR datasets. The RMSE is used to measure the accuracy of the estimated depth values; and bias is used to indicate overestimation (positive value) or underestimation (negative value):

$$\text{RMSE} = \sqrt{\frac{1}{n}\sum_{i=1}^{n}(x^{obs} - x^{est})^2} \qquad (4.8)$$

$$\text{bias} = \frac{\sum_{i=1}^{n}(x^{obs}-x^{est})}{n}\frac{\sum_{i=1}^{n}(x^{obs}-x^{est})}{n} \qquad (4.9)$$

where n is the number of observations, and x^{obs} and x^{est} are the measured and estimated depths, respectively. Values closer to zero for both error metrics indicate a better result. SDB obtained with Rrs_{raw} and $Rrs_{corrected}$ are hereafter referred to as SDB_{raw} and $SDB_{corrected}$ respectively.

4.5. Result and discussion

Scatterplots showing water depth estimates produced from both Rrs_{raw} and $Rrs_{corrected}$ images and the LiDAR depth measurements are shown in Figure 4.4, and summary statistics (R^2, RMSE and bias) are listed in Table 4.4. Accuracy decreases for both SDB_{raw} and $SDB_{corrected}$ with depth, particularly beyond ~15 m where the proportion of the measured signal originating from reflection at the seafloor becomes negligible. In general, for depths shallower than 15 m, $SDB_{corrected}$ points cluster more tightly around the 1:1 line than do the SDB_{raw} points.

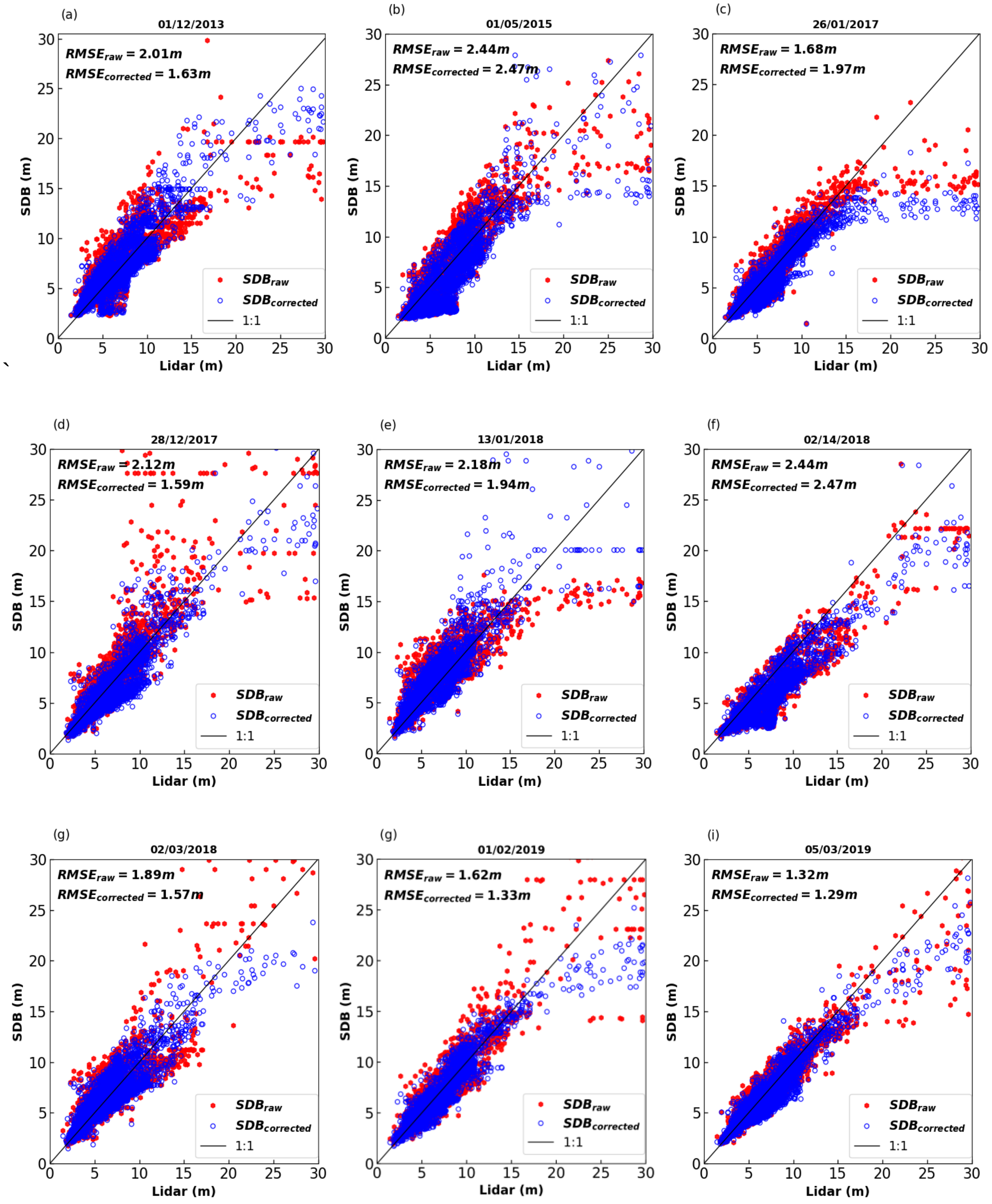

Figure 4.4. **Scatterplots of satellite-derived bathymetry estimates vs LiDAR measurements. Red points show water depth estimates obtained from original ACOLITE outputs; blue points show estimates obtained after applying the correction factor. The 1:1 line is shown in black.**

Table 4.4. Summary validation statistics for SDB estimates (SDB_{raw} and $\text{SDB}_{\text{corrected}}$). Bold letters in the RMSE column indicate where noticeable differences were observed between SDB_{raw} and $\text{SDB}_{\text{corrected}}$ estimates.

Scene date dd/mm/yyyy	**RMSE (m) (SDB_{raw} / $\text{SDB}_{\text{corrected}}$)**	**Bias (SDB_{raw} / $\text{SDB}_{\text{corrected}}$)**	**R^2 (SDB_{raw} / $\text{SDB}_{\text{corrected}}$)**	**Number of validation points**
01/12/2013	2.01 / 1.63	0.13 / 0.11	0.83 / 0.89	3135
05/01/2015	2.44 / 2.47	-1.21 / -1.34	0.83 / 0.80	3351
26/01/2017	1.68 / 1.97	-0.22 / -0.73	0.89 / 0.87	3338
28/12/2017	2.12 / 1.59	0.52 / -0.47	0.86 / 0.90	3148
13/01/2018	2.18 / 1.94	0.58 / 0.66	0.8 / 0.89	2850
14/02/2018	2.11 / 2.04	-1.60 / -1.37	0.93 / 0.91	3351
02/03/2018	1.89 / 1.57	0.21 / 0.07	0.83 / 0.87	3292
01/02/2019	1.62 / 1.33	-0.23 / -0.21	0.91 / 0.94	3303
05/03/2019	1.32 / 1.29	-0.034 / -0.37	0.94 / 0.95	3346

4.5.1. Effects of image conditions on depth accuracy

Turbidity

Out of the nine R_{rs} images we applied the correction factor to, seven corrections resulted in reduced RMSE values, significantly so for six of the images. Two corrections resulted in increased RMSE, one substantially so (the image from 26/01/2017, see Table 4.4) (RMSE values for SDB_{raw} and $\text{SDB}_{\text{corrected}}$ will hereafter be referred to as RMSE_{raw} and $\text{RMSE}_{\text{corrected}}$, respectively). For this image, accurate depth estimates were not possible beyond ~15 m (Figure 4.4c), regardless of correction. A visual inspection of this image shows sediment plumes in the study area (Figure 4.5a), which suggests that turbidity contributed to underestimation of water depth for both SDB_{raw} and $\text{SDB}_{\text{corrected}}$ [14] and the image is of marginal use for SDB regardless of correction. The other image with a slightly increased RMSE (05/01/2015) also has what looks like a silt plume emerging from nearshore channels in the southwestern portion of the area for which depth was calculated (Figure 4.5b).

Glint

With an RMSE value of 2.18 m, the image from 13/01/2018 produces the second-poorest SDB_{raw} estimate out of the nine images. A visual inspection of this image (Figure 4.5c) indicates the presence of moderate glint. Glint correction was not performed as the image did not show any noticeable improvement after the initial testing. Likewise, for the image from 14/02/2018 (Figure 4.5d), the relatively high $RMSE_{raw}$ and $RMSE_{corrected}$ values (and relatively high bias values, Table 4.4) may be attributed to residual sun glint (in addition to light turbidity). While an attempt was made to de-glint this image as described in Section 3.1.2, given that the NIR-based de-glinting method [32] implemented (1) relies on manual selection of deep-water pixels to estimate glint contribution, (2) assumes that there are glint free pixels among those selected [43], and (3) assumes a homogenously low R_{rs}(NIR) across all water pixels, failure to meet these conditions may have resulted in the observed residual glint. For example, R_{rs}(NIR) may be non-negligible in glint-free but very shallow (~1 m) or turbid waters, or where reflective vegetation such as seagrass is close to the upper water column [44]. For these two images, the correction produces slightly reduced RMSE values (Figures 4.4e and 4.4f).

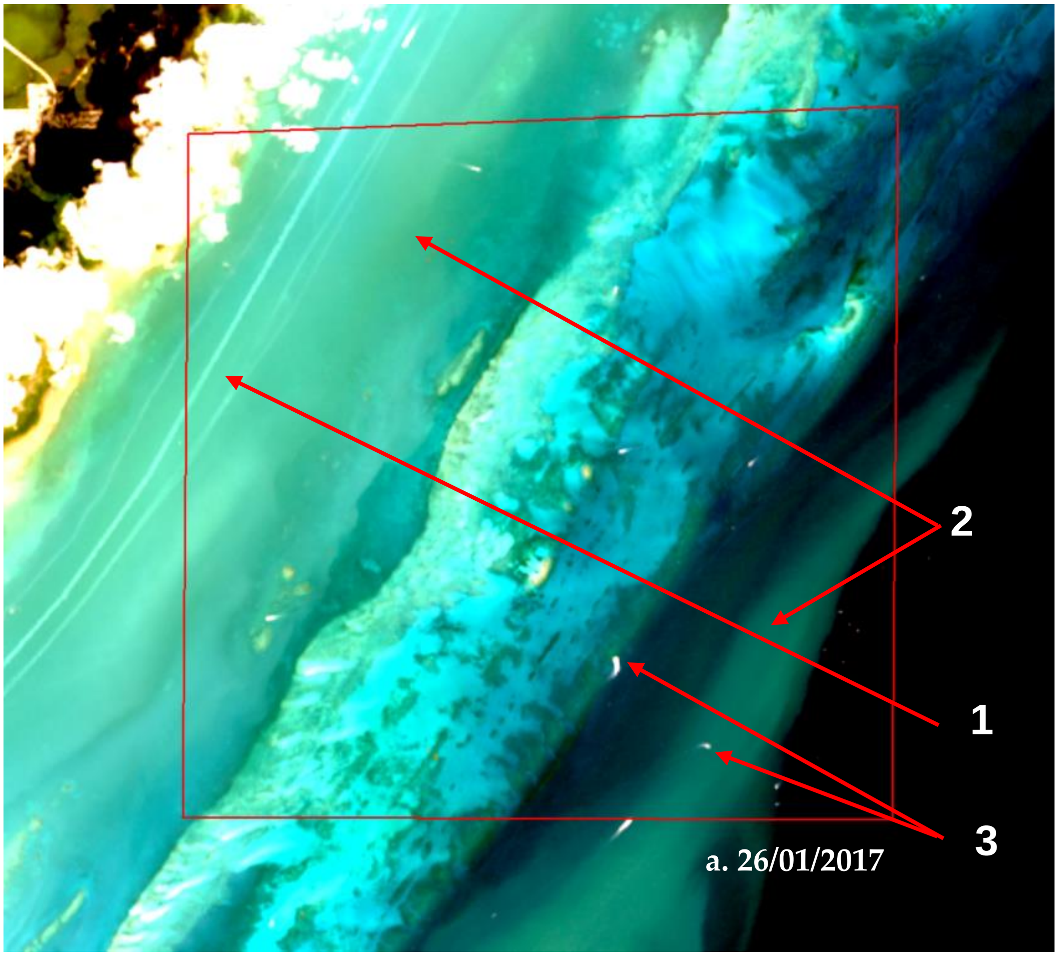
2
1
3
a. 26/01/2017

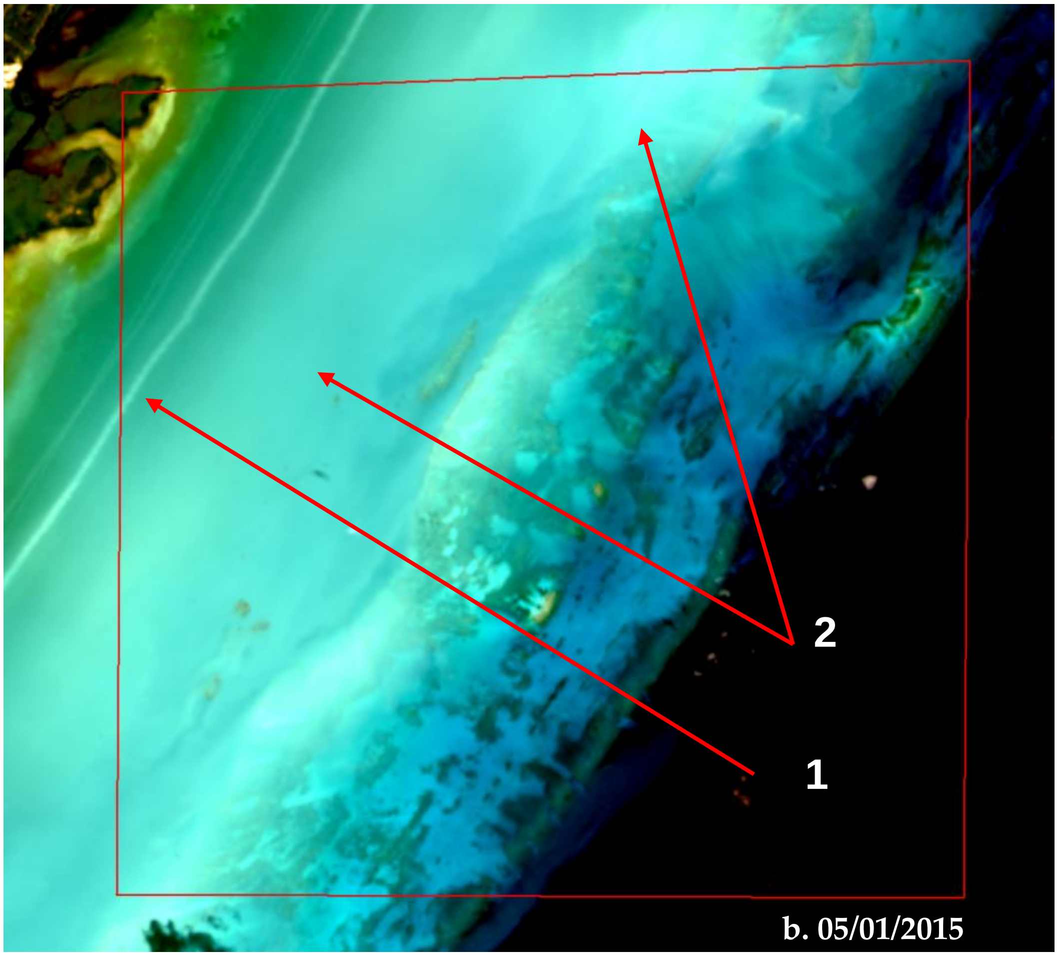
2
1
b. 05/01/2015

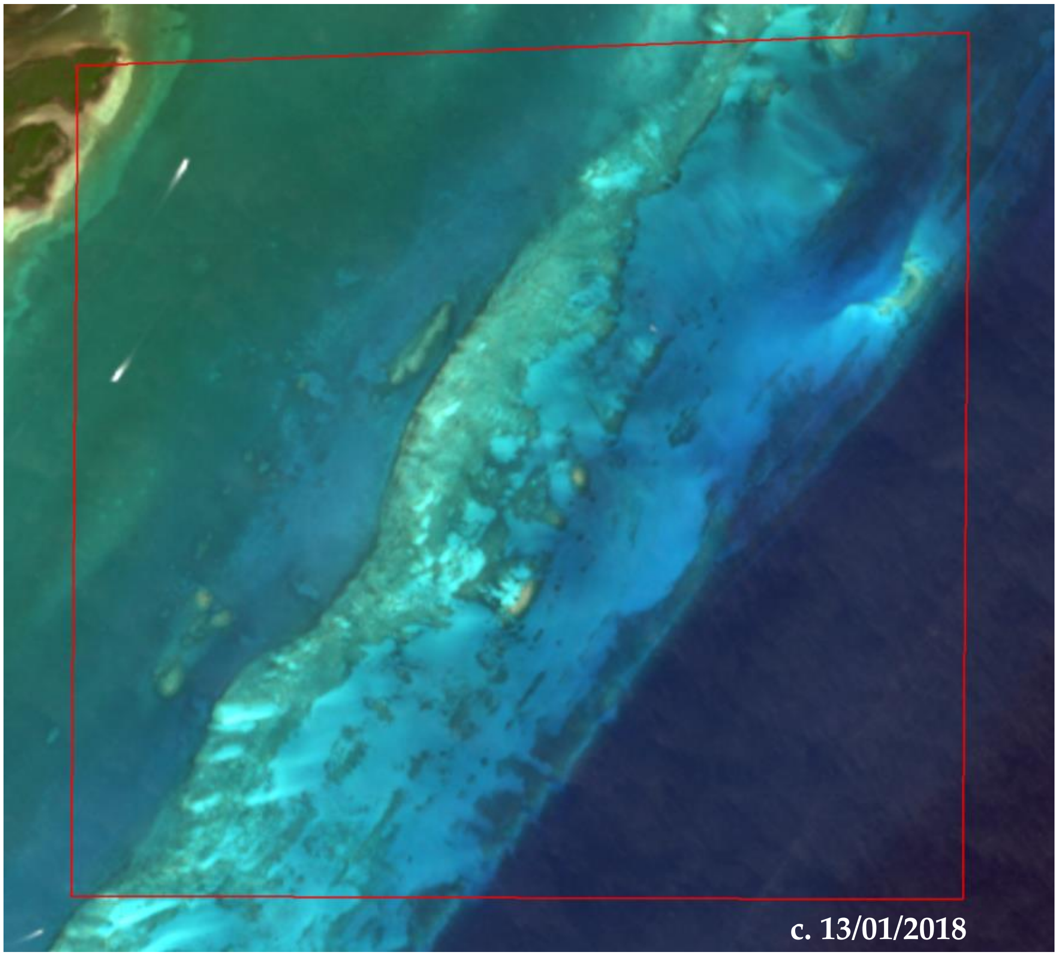
c. 13/01/2018

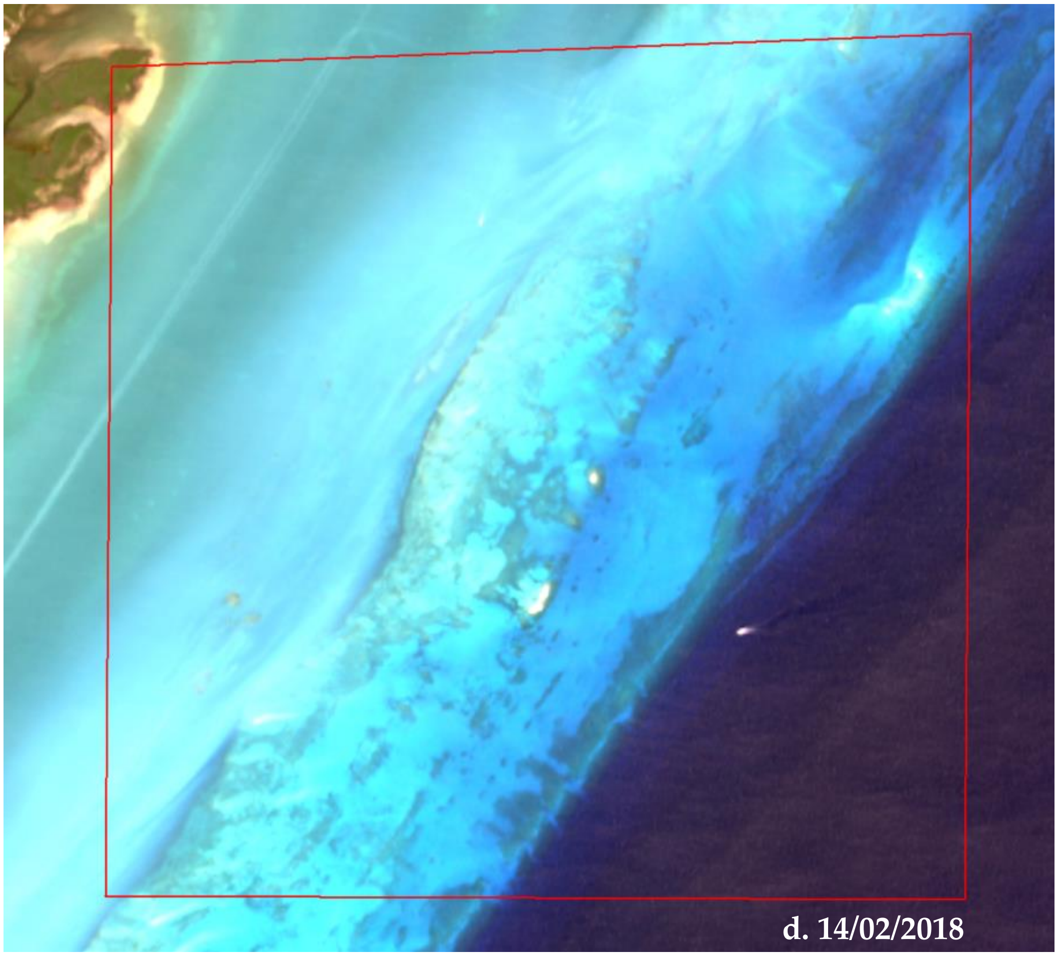

Figure 4.5. **Maps showing different confounding factors that might have affected SDB estimates from some images. (a) and (b) - 1: Boat-generated wake. 2: Plume emerging from a near river discharge. 3: Moving boats. Sun glint can be observed in (c) and (d) as visible texture around the southeastern part of the images.**

4.5.2. Effect of wind speed and SZA on SDB performance

This section discusses the effect of the environmental variables on AC accuracy. It should be noted that only SZA and wind speed are discussed as AOT did not seem to affect AC accuracy.

Out of the seven scenes whose SDB performance improved with the correction, greater corrections were done for five scenes (i.e., Figures 4.4a, d, e, f and h) acquired with SZA > 45° (Table 4.1), and the remaining two scenes (i.e., Figures 4.4g and i) were acquired during high wind speed (3.21 and 4.67 m/s, respectively). The most noticeable RMSE reduction from correction ($RMSE_{raw}$=2.12; $RMSE_{corrected}$=1.59) was observed for the scene with the highest SZA and highest wind speed (Figure 4.4d). This is supporting evidence for the existence of a relationship between ACOLITE's overestimation of R_{rs} in the first two bands of L8 and these two environmental variables (Ilori et al. 2019), and gives an idea of the magnitude of its impact on SDB performance. A recent observation by Estrella et al. (2020) [46] also found a dependecy between AC retrieval accuracy and wind speed in coastal waters. While there is strong evidence to conclude that the correction factor used in this study lowers RMSE values for images with high wind speed, it should be noted that wind speed data used in this study come from 6-hour estimates in reanalysis model, and thus have their own uncertainty. For this reason, more testing may be needed for a firmer conclusion about the relationship between ACOLITE's error and wind speed.

4.5.3. Bathymetry estimates at different depth ranges

Figure 4.6 shows the performance of SDB_{raw} and $SDB_{corrected}$ for each image, binned to 5-m depth increments. The accuracy of SDB estimates decreases with increasing depth for both SDB_{raw} and $SDB_{corrected}$. While higher RMSE values should be expected at deeper depths due to the diminishing signal from seafloor reflectance, it should be noted that the number of LiDAR points for validation is also smaller at deeper depths, leading to increased uncertainty around the RMSE values reported at these depths.

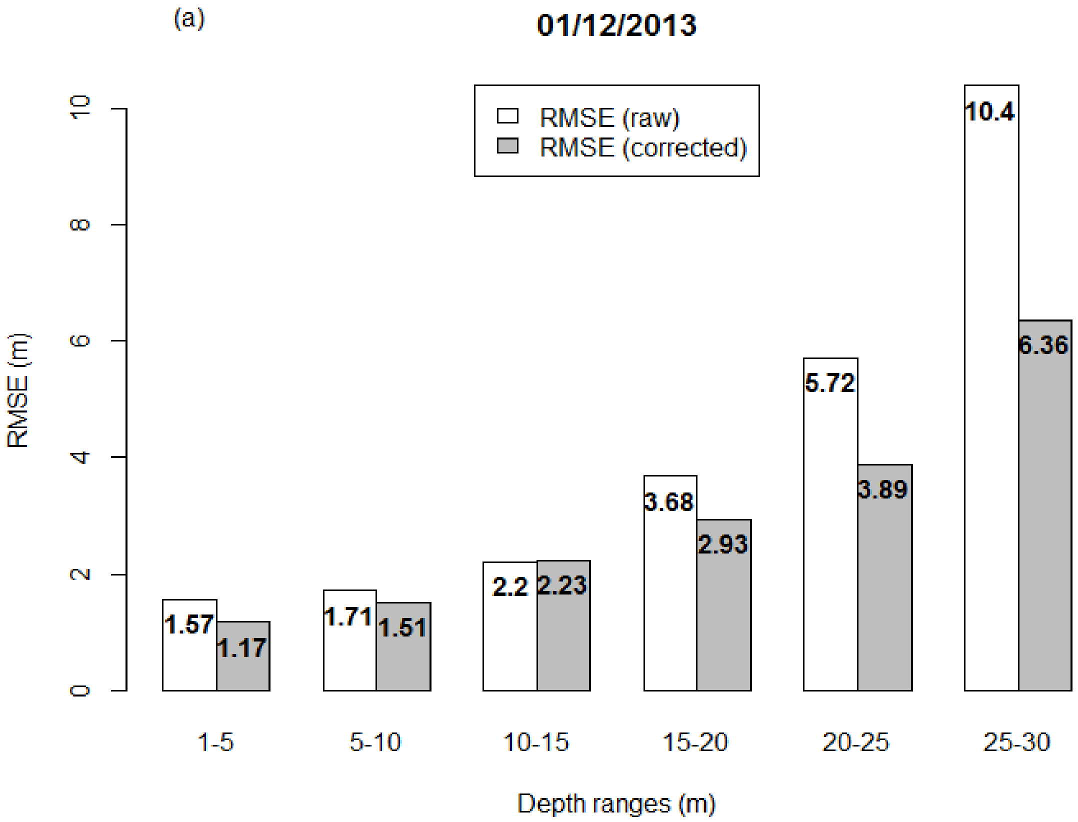
(a)
01/12/2013
RMSE (raw)
RMSE (corrected)
RMSE (m)
0
2
4
6
8
10
1.57
1.17
1.71
1.51
2.2
2.23
3.68
2.93
5.72
3.89
10.4
6.36
1-5
5-10
10-15
15-20
20-25
25-30
Depth ranges (m)

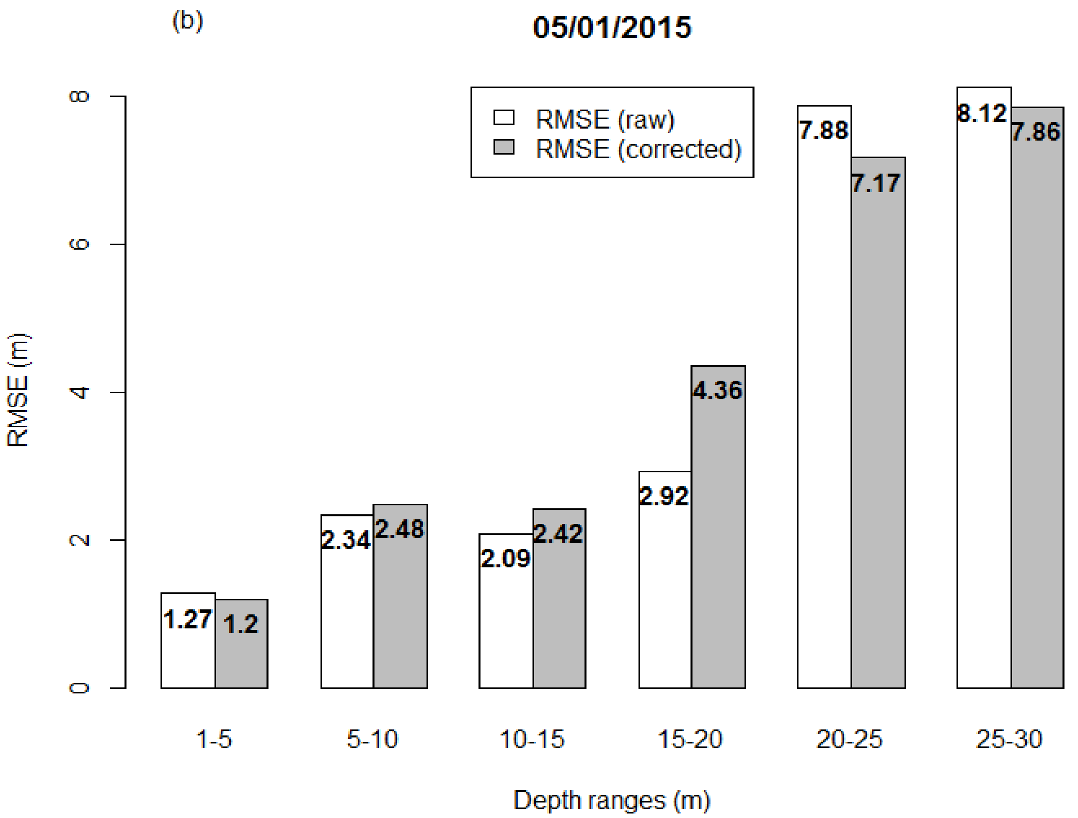
(b)
05/01/2015
RMSE (raw)
RMSE (corrected)
RMSE (m)
0
2
4
6
8
1.27
1.2
2.34
2.48
2.09
2.42
2.92
4.36
7.88
7.17
8.12
7.86
1-5
5-10
10-15
15-20
20-25
25-30
Depth ranges (m)

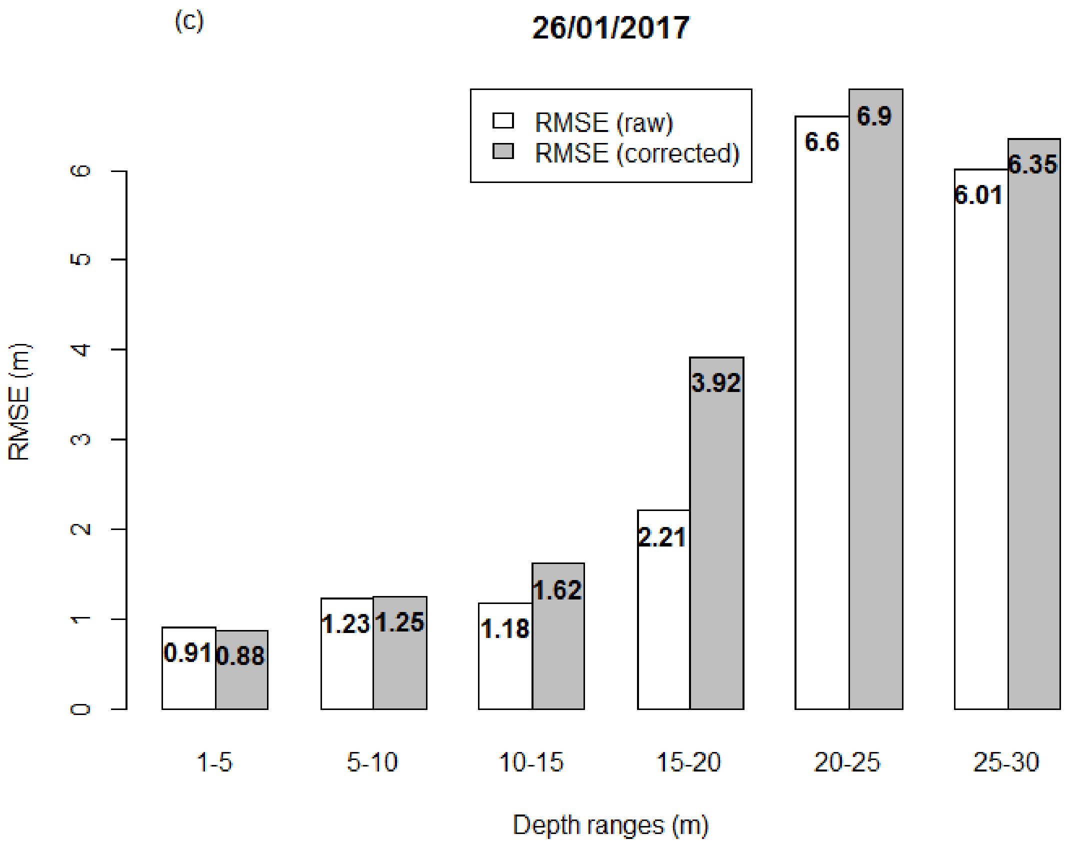
(c)
26/01/2017
RMSE (raw)
RMSE (corrected)
RMSE (m)
0
1
2
3
4
5
6
0.91
0.88
1.23
1.25
1.18
1.62
2.21
3.92
6.6
6.9
6.01
6.35
1-5
5-10
10-15
15-20
20-25
25-30
Depth ranges (m)

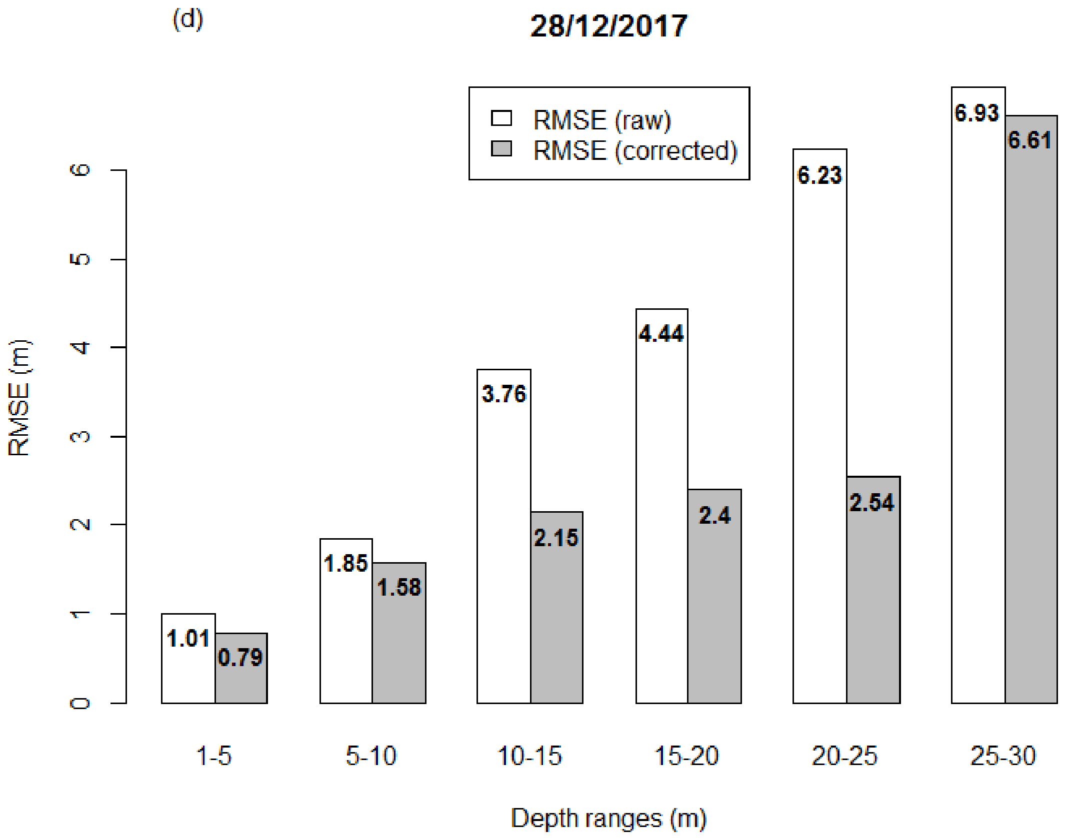
(d)
28/12/2017
RMSE (raw)
RMSE (corrected)
RMSE (m)
0
1
2
3
4
5
6
1.01
0.79
1.85
1.58
3.76
2.15
4.44
2.4
6.23
2.54
6.93
6.61
1-5
5-10
10-15
15-20
20-25
25-30
Depth ranges (m)

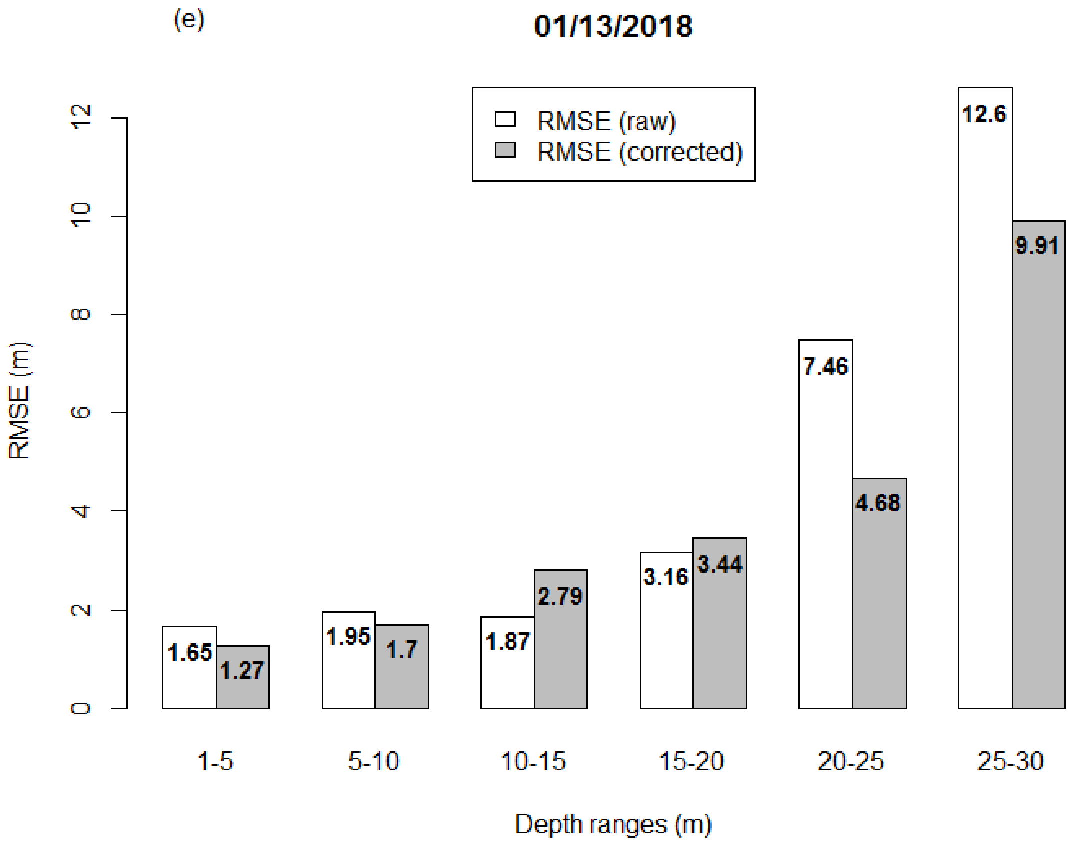
(e)
01/13/2018
RMSE (raw)
RMSE (corrected)
RMSE (m)
0
2
4
6
8
10
12
1.65
1.27
1.95
1.7
1.87
2.79
3.16
3.44
7.46
4.68
12.6
9.91
1-5
5-10
10-15
15-20
20-25
25-30
Depth ranges (m)

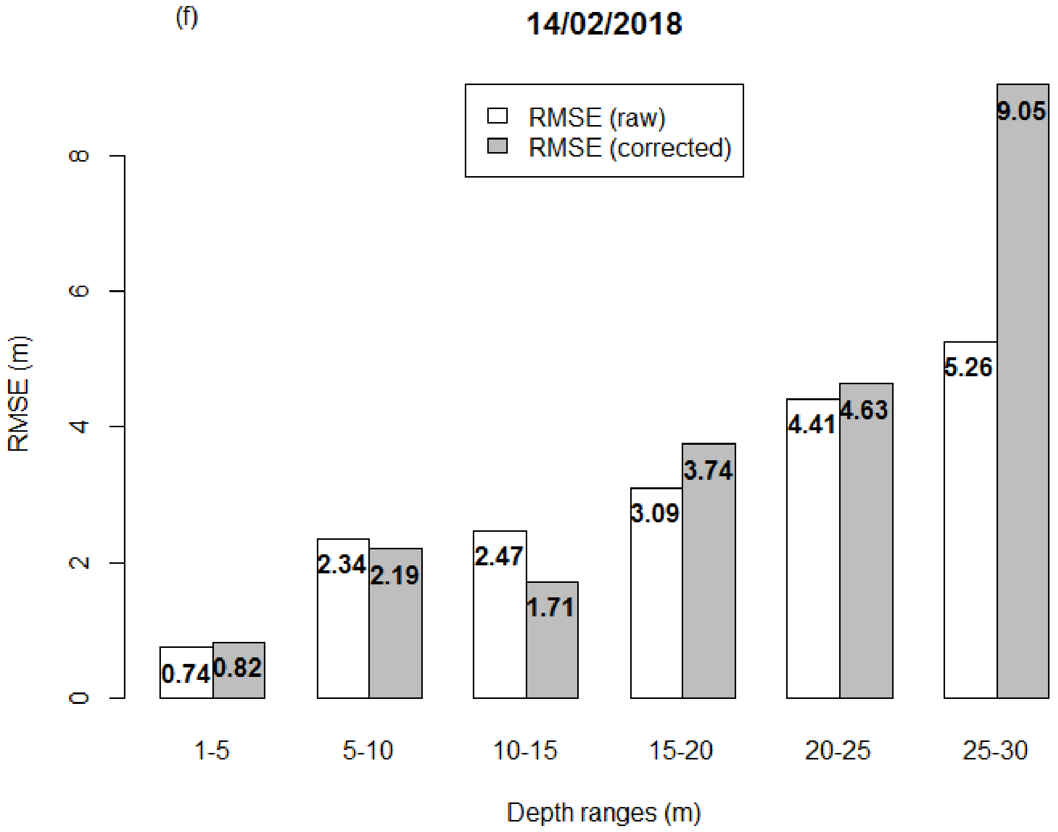
(f)
14/02/2018
RMSE (raw)
RMSE (corrected)
RMSE (m)
0
2
4
6
8
0.74
0.82
2.34
2.19
2.47
1.71
3.09
3.74
4.41
4.63
5.26
9.05
1-5
5-10
10-15
15-20
20-25
25-30
Depth ranges (m)

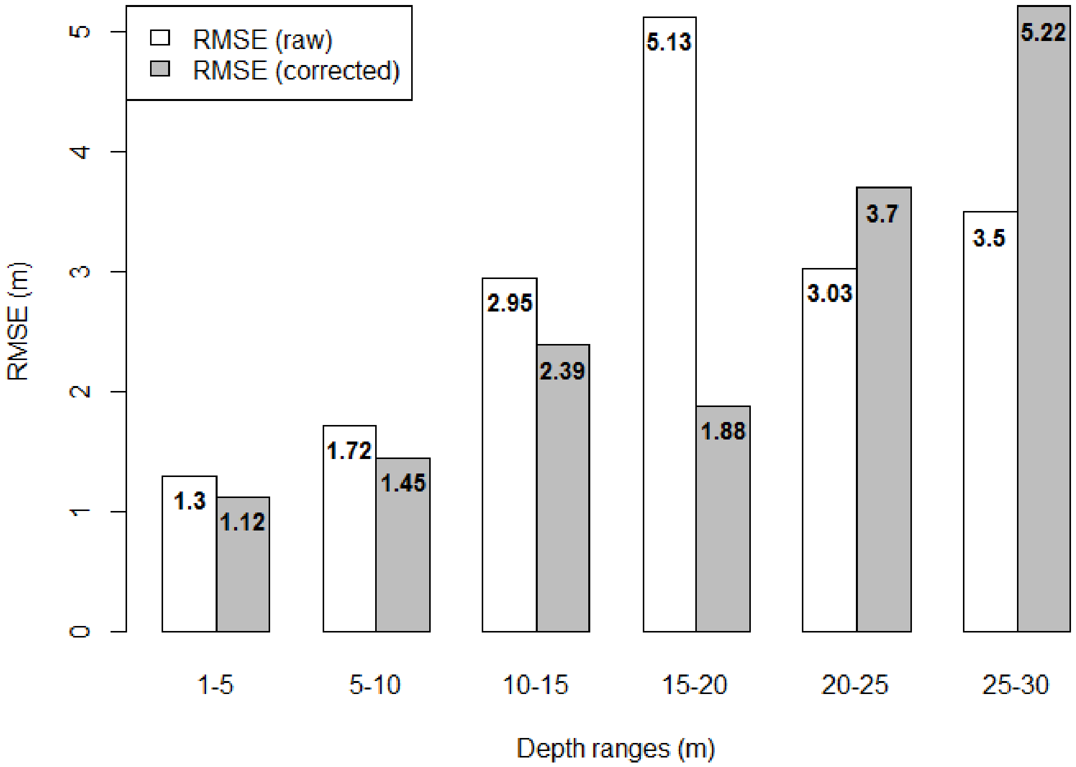

(g)

02/03/2018

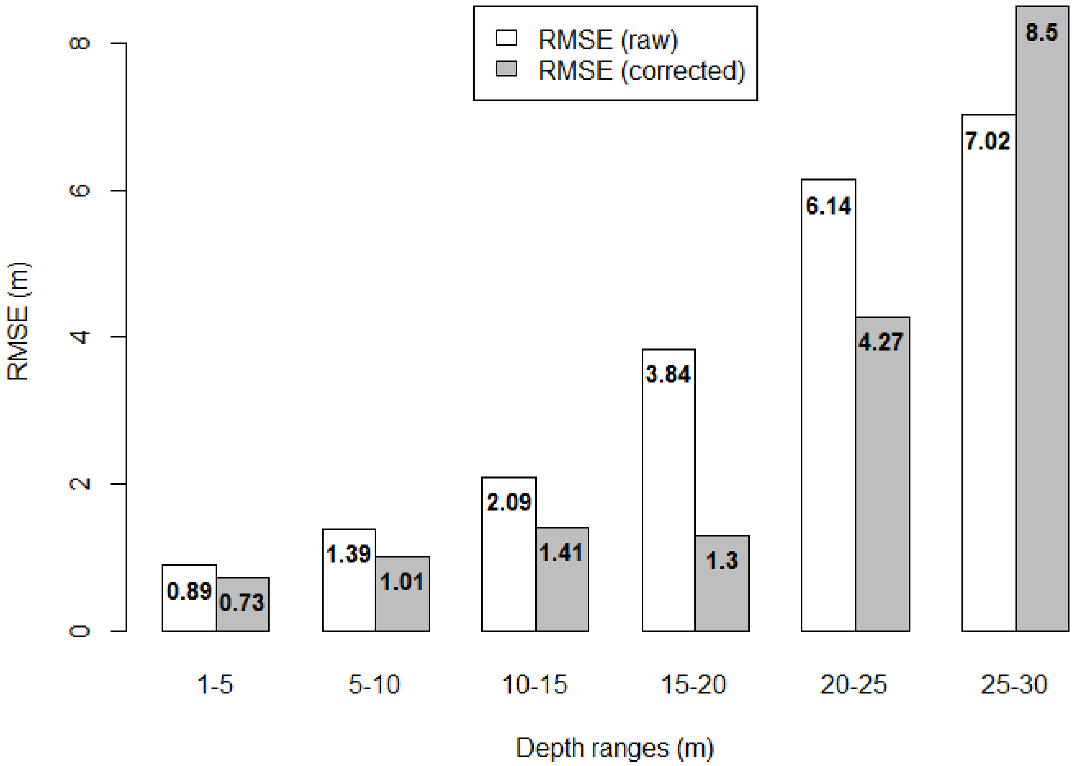

(h)

01/02/2019

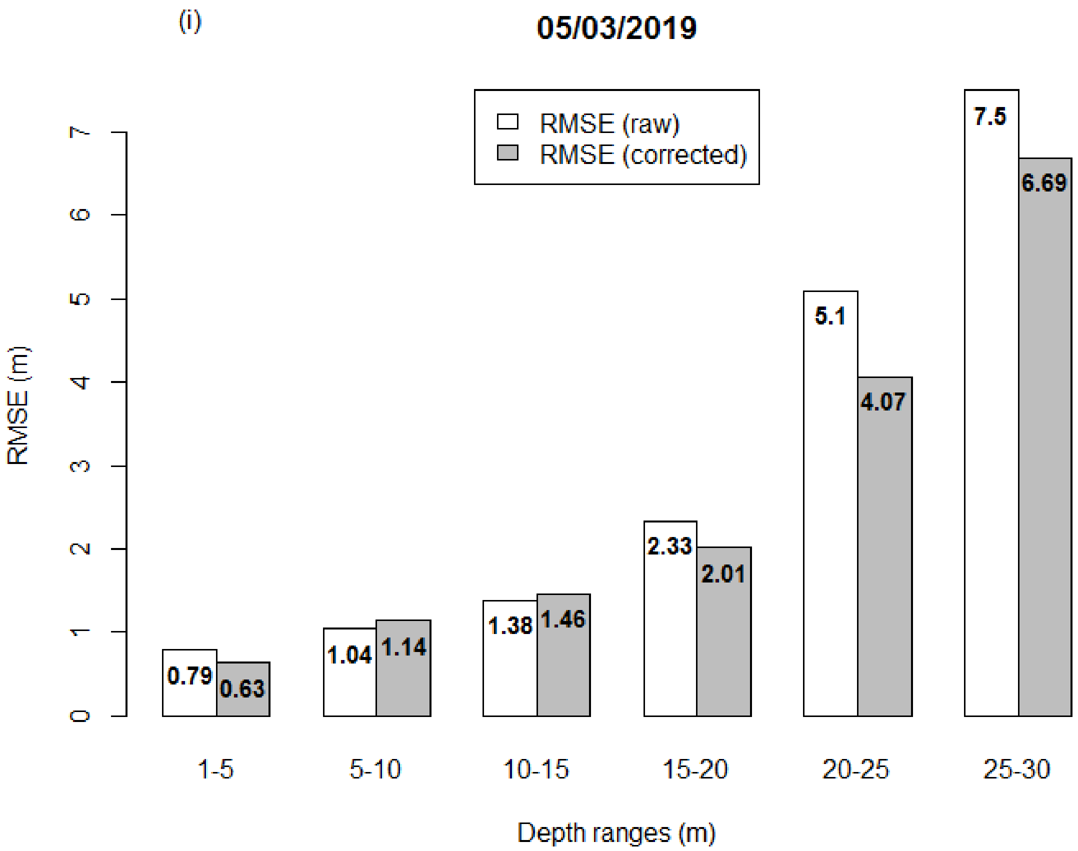

Figure 4.6. **(a-i) RMSE values obtained for SDB_{raw} and $SDB_{corrected}$ estimates at different water depths. Results at higher depth (> 20m) should be interpreted with caution as the number of depth observations for those depth ranges was comparably lower than those available for shallower depth ranges. Depth observation for each depth range is as follows: 1-5 m: ~600, 5-10 m: ~1500, 10-15 m: ~300, 15-20 m: ~40, 30-25 m: ~20 and 25-30 m: ~20. Note that the y-axes have different ranges for each date, to facilitate comparison between $RMSE_{raw}$ and $RMSE_{corrected}$ for each single scene.**

4.5.4. SDB estimates using an ensemble approach

Most SDB studies are based on a single image for each study area, with researchers typically selecting the best available image using visual inspection [14]. Our results indicate that this may not be a robust approach. To illustrate the problem, we invite readers to visually inspect the nine images used in this study (Figure 4.2), and identify the one that looks most suitable for SDB. Then proceed to Table 4.4 to see if it was indeed the one that produced the best results, as measured by RMSE, bias, or R^2. An informal test among our colleagues, all of whom work on ocean colour remote sensing, suggests that it is not easy to identify the best scene. However, a unique advantage of optical remote sensing is repetitive acquisition of images over the same area. This is especially important for SDB, where the suitability of a given image is determined by transient environmental factors, such as cloud and aerosols, sea surface state, and turbidity [47]. We explored one way of taking advantage of the multiple images available for the study area (i.e., all 9 images) by testing an ensemble approach in which we calculated the per-pixel median depth value of all nine corrected images (i.e., $SDB_{corrected}$) used in this study. We then compared the resulting depth estimates with those obtained using the best individual image from the analysis in Section 4.1 (i.e. the image from 05/03/2019, see Table 4.4). Figure 4.7 shows that the results produced by the ensemble are very similar to those obtained with the best individual image (compare to Figure 4.4i). SDB estimates up to ~17m are similar to the $SDB_{corrected}$ estimates from the 05/03/2019 image, as are the RMSE values for the 1-5, 5-10, and 10-15 m depth ranges (Figure 4.8). Outliers are noticeably reduced in the ensemble result when compared to any of the sub-optimal images that were also included in its calculation, suggesting that the use of median depth is effective in eliminating noise in the ensemble. The ensemble approach thus eliminates the need for selection of a single best image, while producing SDB results of similar accuracy. In this context it is noteworthy that the best image is also the one with the lowest $NE\Delta R_{rs}$ in bands 1, 2 and 4, as well as the second-lowest $NE\Delta R_{rs}$ in band 3 (Table 4.2). This suggests that one effective way to pre-screen images, either for a single-best-image approach or to determine which images should be included in an ensemble, could be to estimate $NE\Delta R_{rs}$ and select those images with the lowest values across the visible bands.

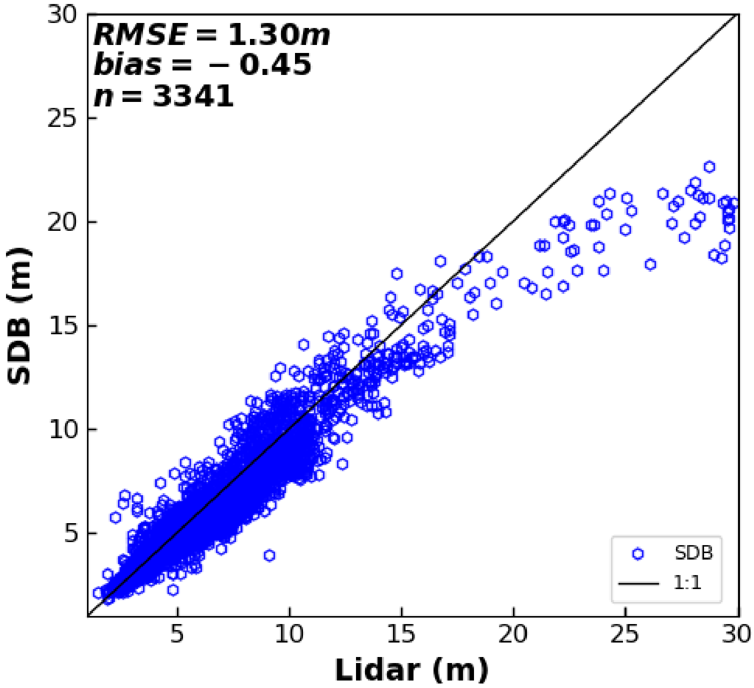

Figure 4.7. **Scatterplots of ensemble-based satellite-derived bathymetry estimates vs LiDAR measurements. Blue dots show estimates obtained after applying a correction to the R_{rs} images. The solid line represents the 1:1 relationship.**

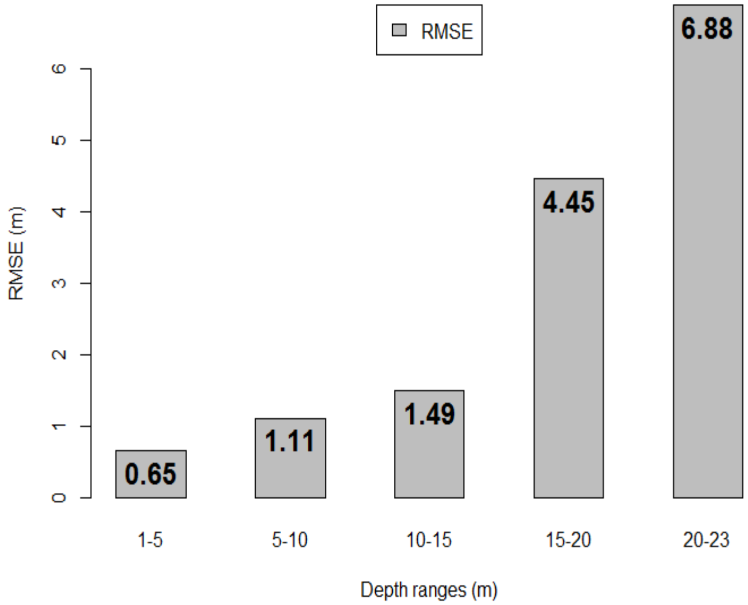

Figure 4.8. **RMSE values obtained for the ensemble based SDB estimates at different water depths.**

4.6. Conclusion

In this study, we demonstrated the use of Landsat 8 data for physics-based SDB in US coastal waters. A state-of-the-art atmospheric correction method (ACOLITE) was used to convert per-pixel radiometric units to R_{rs}, and a radiative transfer model was inverted to estimate water depth, which was compared to airborne lidar validation data. The results showed that ACOLITE can be used to produce SDB from imagery that is free of conditions such as clouds, glint, sediments plumes, boats and wakes, with an accuracy (RMSE 1.32 m) comparable to that reported from empirical and physics-based SDB elsewhere. To account for ACOLITE's known overestimation of R_{rs} for Landsat 8's coastal and blue bands, we applied a correction factor, calculated as a function of solar zenith angle, aerosol optical thickness and wind speed, to obtain a corrected set of R_{rs} images. Using a total of nine Landsat 8 images, we showed that the correction factor improved SDB results, both on average (RMSE reduction of 0.17 m) and for the best single image (RMSE reduction of 0.03 m). SDB improvements from application of the correction factor were greatest for images acquired at high solar zenith angle and at high wind speeds, where ACOLITE is known to have the greatest bias. The correction method demonstrated in this study can be implemented with any appropriate AC algorithm. Finally, we demonstrated that an ensemble approach based on multiple images, with acquisitions ranging from optimal to sub-optimal conditions, can be used to derive bathymetry with a result that is similar to what can be obtained from the best individual image. This is important because it is rarely visually obvious which of several images is best for SDB, and the ensemble approach can be automated to reduce time spent on pre-screening and filtering of scenes, and potentially also reduce the amount of missing pixels caused by clouds and cloud shadows encountered in any single image. Automating SDB will ultimately facilitate the efficient and operational use of the globally available L8 (and other multispectral) data sets.

4.7. References

1. Collin A, Archambault P, Long B. Mapping the shallow water seabed habitat with the SHOALS. In: *IEEE Trans. Geosci. Remote Sens*. **2008**, p. 2947–55.
2. Stumpf RP, Holderied K, Sinclair M. Determination of water depth with high-resolution satellite imagery over variable bottom types. *Limonology Oceanogr*. **2003**, 48:547–56. Available from: http://www.aslo.org/lo/toc/vol_48/issue_1_part_2/0547.html
3. Brock JC, Wright CW, Clayton TD, Nayegandhi A. LIDAR optical rugosity of coral reefs in Biscayne National Park, Florida. Coral Reefs. **2004,** 23(1):48–59.
4. Wozencraft JM. SHOALS airborne coastal mapping: past, present and future*. J Coastal Res* 38:207–216. **2003**.
5. Gao J. Bathymetric mapping by means of remote sensing: methods, accuracy and limitations. *Prog Phys Geogr*. **2009,** 33(1):103–16.
6. Su H, Liu H, Heyman WD. Automated Derivation of Bathymetric Information from Multi-Spectral Satellite Imagery Using a Non-Linear Inversion Model. *Mar Geod*. **2008,** 31(4):281–98. Available from: http://www.tandfonline.com/doi/abs/10.1080/01490410802466652
7. Lyzenga DR. Passive remote sensing techniques for mapping water depth and bottom features. *Appl Opt.* **1978,** 17(3):379–83.
8. Lyzenga DR. Remote sensing of bottom reflectance and water attenuation parameters in shallow water using aircraft and landsat data. *Int J Remote Sens*. **1981,** pp 71-82. https://doi.org/10.1080/01431168108948342
9. Lyzenga DR. Shallow-water bathymetry using combined lidar and passive multispectral scanner data. *Int J Remote Sens.* **1985,** 6(1):115–25.
10. Chénier R, Faucher MA, Ahola R. Satellite-derived bathymetry for improving Canadian Hydrographic Service charts. *ISPRS Int J Geo-Information*. **2018**, *7*(8), 306; https://doi.org/10.3390/ijgi7080306
11. Hedley J, Roelfsema C, Koetz B, Phinn S. Capability of the Sentinel 2 mission for tropical coral reef mapping and coral bleaching detection. *Remote Sens Environ.* **2012,** 120:145–55. Available from: http://dx.doi.org/10.1016/j.rse.2011.06.028
12. Knudby A, Ahmad SK, Ilori C. The Potential for Landsat-Based Bathymetry in Canada. *Can J Remote Sens.* **2016**, 42(4):367–78.

13. Olayinka, Ilori Christopher, and Anders Knudby. 2019. "Satellite-Derived Bathymetry Using a Radiative Transfer-Based Method: A Comparison of Different Atmospheric Correction Methods." in *OCEANS 2019 MTS/IEEE Seattle, OCEANS* ***2019***.
14. Casal G, Hedley JD, Monteys X, Harris P, Cahalane C, McCarthy T. Satellite-derived bathymetry in optically complex waters using a model inversion approach and Sentinel-2 data. *Estuar Coast Shelf Sci*. **2020**, 241:106814. Available from:http://www.sciencedirect.com/science/article/pii/S0272771420302006
15. Mobley CD, Sundman LK, Davis CO, Bowles JH, Downes TV, Leathers RA, et al. Interpretation of hyperspectral remote-sensing imagery by spectrum matching and look-up tables. *Appl Opt*. **2005**, 44(17):3576. Available from: https://www.osapublishing.org/abstract.cfm?URI=ao-44-17-3576
16. Hedley J, Roelfsema C, Phinn SR. Efficient radiative transfer model inversion for remote sensing applications. *Remote Sens Environ*. **2009,** 113(11):2527–32. Available from: http://dx.doi.org/10.1016/j.rse.2009.07.008
17. Lee Z, Carder KL, Mobley CD, Steward RG, Patch JS. Hyperspectral remote sensing for shallow waters. I. A semianalytical model. *Appl Opt*. **1998,** 37(27):6329–38.
18. Lee Z, Carder KL, Mobley CD, Steward RG, Patch JS. Hyperspectral remote sensing for shallow waters. 2. Deriving bottom depths and water properties by optimization. *Appl Opt*. **1999,** 38(18):3831–43. Available from: http://www.ncbi.nlm.nih.gov/pubmed/18319990
19. Pahlevan N, Schott JR, Franz BA, Zibordi G, Markham B, Bailey S, et al. Landsat 8 remote sensing reflectance (Rrs) products: Evaluations, intercomparisons, and enhancements. *Remote Sens Environ*. **2017,** 190:289–301. Available from: http://dx.doi.org/10.1016/j.rse.2016.12.030
20. Doxani G, Vermote E, Roger J, Gascon F, Adriaensen S, Frantz D, et al. Atmospheric Correction Inter-Comparison Exercise. *Remote Sens*. 2018; 10(2):1–18. Comparison Exercise. Remote Sens. **2018**; 10(2):1–18.
21. Warren MA, Simis SGH, Martinez-Vicente V, Poser K, Bresciani M, Alikas K, et al. Assessment of atmospheric correction algorithms for the Sentinel-2A MultiSpectral Imager over coastal and inland waters. *Remote Sens Environ*. **2019**, 225: 267-289. https://doi.org/10.1016/j.rse.2019.03.018.
22. Zhang M, Hu C. Evaluation of Remote Sensing Reflectance Derived From the Sentinel-2 Multispectral Instrument Observations Using POLYMER Atmospheric Correction. *IEEE Trans Geosci Remote Sens*. **2020,** 1–8.

23. Ilori C, Pahlevan N, Knudby A. Analyzing Performances of Different Atmospheric Correction Techniques for Landsat 8: Application for Coastal Remote Sensing. *Remote Sens*. **2019**, 11(4):469. Available from: http://www.mdpi.com/2072-4292/11/4/469
24. Vanhellemont Q, Ruddick K. Advantages of high quality SWIR bands for ocean colour processing: Examples from Landsat-8. *Remote Sens Environ*. **2015,** 161:89–106.
25. Storey J, Choate M, Lee K. Landsat 8 operational land imager on-orbit geometric calibration and performance. *Remote Sens*. **2014,** 6(11):11127–52.
26. Czapla-Myers J, McCorkel J, Anderson N, Thome K, Biggar S, Helder D, et al. The ground-based absolute radiometric calibration of Landsat 8 OLI. *Remote Sens*. **2015**, 7(1):600–26.
27. Kotchenova SY, Vermote EF, Levy R, Lyapustin A. Radiative transfer codes for atmospheric correction and aerosol retrieval : intercomparison study. *Appl Opt*. **2008**, 47(13):2215–26. Available from: http://www.ncbi.nlm.nih.gov/pubmed/18449285
28. Ruddick KG, Ovidio F, Rijkeboer M. Atmospheric correction of SeaWiFS imagery for turbid coastal and inland waters. *Appl Opt.* **2000,** 39(6):897–912. Available from: http://ao.osa.org/abstract.cfm?URI=ao-39-6-897
29. Vanhellemont Q, Ruddick K. Acolite for Sentinel-2 : Aquatic applications of MSI Imagery. **2016**, 9–13.
30. Vanhellemont Q, Ruddick K. Atmospheric correction of metre-scale optical satellite data for inland and coastal water applications. *Remote Sens Environ*. **2018**, 216:586–97. Available from: https://doi.org/10.1016/j.rse.2018.07.015
31. Kalnay E, Kanamitsu M, Kistler R, Collins W, Deaven D, Gandin L, et al. The NCEP/NCAR 40-Year Reanalysis Project. *Bull Am Meteorol Soc*. **1996,** 77(3):437–72. Available from: https://doi.org/10.1175/1520-0477(1996)077%3C0437:TNYRP%3E2.0.CO
32. Hedley JD, Harborne a. R, Mumby PJ. Technical note: Simple and robust removal of sun glint for mapping shallow-water benthos. *Int J Remote Sens*. **2005**, 26 (10):2107–12.
33. Botha EJ, Brando VE, Dekker AG. Effects of per-pixel variability on uncertainties in bathymetric retrievals from high-resolution satellite images. *Remote Sens*. **2016**, 8 (6).
34. Jay S, Guillaume M, Minghelli A, Deville Y, Chami M, Lafrance B, et al. Hyperspectral remote sensing of shallow waters: Considering environmental noise and bottom intra-

class variability for modeling and inversion of water reflectance. *Remote Sens Environ*. **2017**, 200:352–67.

35. Brando VE, Dekker AG. Satellite hyperspectral remote sensing for estimating estuarine and coastal water quality. *IEEE Trans Geosci Remote Sens*. **2003**, 41(6):1378–87. Available from: http://ieeexplore.ieee.org/lpdocs/epic03/wrapper.htm?arnumber=1220246
36. Wettle M, Brando VE, Dekker AG. A methodology for retrieval of environmental noise equivalent spectra applied to four Hyperion scenes of the same tropical coral reef. *Remote Sens Environ*. **2004**, 93(1–2):188–97.
37. Brando VE, Anstee JM, Wettle M, Dekker AG, Phinn SR, Roelfsema C. A physics based retrieval and quality assessment of bathymetry from suboptimal hyperspectral data. Remote Sens Environ. **2009,** 113(4):755–70.
38. Maritorena S, Siegel D a, Peterson AR. Optimization of a semianalytical ocean color model for global-scale applications. *Appl Opt*. **2002**, 41(15):2705–14. Available from: http://www.ncbi.nlm.nih.gov/pubmed/12027157
39. Acker JG, Leptoukh G. Online analysis enhances use of NASA Earth Science Data. Eos, *Trans. Amer. Geophys*. **2007**. Union, 88, 14. doi:10.1029/2007EO020003.
40. NCCOS. Benthic Habitat Mapping of Florida Coral Reef Ecosystems to Support Reef Conservation and Management. **2014**. Available online: https://coastalscience.noaa.gov/project/benthic-habitat-mapping-florida-coral-reef-ecosystems/ (accessed on 22 March 2019).
41. Pope RM, Fry ES. Absorption spectrum (380–700 nm) of pure water II Integrating cavity measurements. *Appl Opt*. **1997**, 36, 8710-8723.
42. Egbert GD, Erofeeva SY. Efficient inverse modeling of barotropic ocean tides. *J. Atmos. Oceanic Technol.* **2002**, 19 (2): 183–204. https://doi.org/10.1175/1520-0426(2002)019%3C0183:EIMOBO%3E2.0.CO;2
43. Harmel T, Chami M, Tormos T, Reynaud N, Danis PA. Sunglint correction of the Multi-Spectral Instrument (MSI)-SENTINEL-2 imagery over inland and sea waters from SWIR bands. *Remote Sens Environ*. **2018**, 204:308–21.
44. Overstreet BT, Legleiter CJ. Removing sun glint from optical remote sensing images of shallow rivers. *Earth Surface Processes and Landforms*. **2017**, https://doi.org/10.1002/esp.4063 (accessed 08 May, 2020)
45. Acker, James G., and Gregory Leptoukh. Online Analysis Enhances Use of NASA Earth Science Data. *Eos. Trans. AGU,* **2007,** *88*(2), pp 14-17.

46. Estrella EH, Grotsch P, Gilerson A, Malinowski M, Ahmed S. Blue band reflectance uncertainties in coastal waters and their impact on retrieval algorithms. In: Hou W “Will”, Arnone RA, editors. Ocean Sensing and Monitoring XII. *SPIE,* **2020,** p. 17–29. Available from: https://doi.org/10.1117/12.2559895
47. Jégat V, Pe S, Freire R, Klemm A, Nyberg J. Satellite-Derived Bathymetry: Performance and Production. *Can Hydrogr Conf.* **2016**, 1–8.
48. (https://coast.noaa.gov/digitalcoast/).

Chapter 5. Conclusions

This thesis consists of three separate, but related studies with the overarching aim of assessing and demonstrating the utility of physics-based SDB in coastal waters of North America. This chapter discusses the key findings and contributions from each chapter.

5.1. Key findings and contributions

Chapter 2 focuses on the utility of multispectral data for physics-based bathymetry using a case study from three Canadian waters – Boundary Bay, Hudson Bay and Baffin Bay. Results indicate that Landsat 8 data can be used for mapping water depths up to ~4.5 m with less than 1 m error at 95% confidence in the relatively clear northern waters, though only up to ~3 m in the more turbid conditions found in Boundary Bay. Notably, a key finding of this chapter is that precise AC is crucial for robust SDB retrievals, and that AC is the primary obstacle to physics-based SDB as observed from the results obtained in this chapter. Also, it was revealed that SDB has limitations when applied to turbid, optically shallow waters. While there is currently no effective way to correct the impact of turbidity, imprecise atmospheric correction can be minimized.

To this end, the focus of chapter 3 was on the evaluation of several freely available atmospheric correction methods to determine the best algorithm that can minimize error when estimating the remote sensing reflectance, from which ocean colour products are estimated. Results revealed that generic AC methods which perform reasonably well over land are not appropriate for ocean color products retrieval. Findings of this chapter will guide the selection of appropriate AC method for estimating ocean colour products. Furthermore, as all AC algorithms contain some form of biases which are related to environmental factors and not accounted for during their implementation, chapter 3 further assessed the effects of three environmental variables (SZA, wind speed and AOT) believed to be affecting AC retrieval accuracy. Analysis with SeaDAS and ACOLITE (two state-of-art, water-based AC methods) showed that SZA and wind speed strongly affect AC retrieval accuracy, especially in Landsat 8’s first two bands, and especially for ACOLITE. This contribution is valuable as it may guide further developments of AC methods to make them more robust across a broader range of environmental conditions.

This will particularly be important for physics-based SDB, which benefits from a special treatment for a correction of the atmospheric and environmental factors.

To show the effects of environmental factors on AC retrieval accuracy and how they can be minimized for robust SDB retrievals, chapter 4 describes an approach to minimize atmospheric correction error and improve physics-based SDB. Drawing on the lessons learned in chapters 2 and 3, ACOLITE - a widely used AC algorithm - was used to estimate bathymetry for an area in the Florida Keys, USA. A correction factor, calculated as a function of solar zenith angle, aerosol optical thickness and wind speed on the basis of data from chapter 3, was applied to nine Landsat 8 images. Results revealed that accounting for AC errors related to SZA and wind speed can lead to improved SDB retrievals, especially for images acquired at high solar zenith angle and at high wind speeds, where ACOLITE is known to have the greatest bias. A similar approach can be used to improve remote sensing reflectance from other biased AC algorithms, and for deriving other ocean colour products such as seafloor habitat and water quality maps. In addition, it was shown that an ensemble approach based on the use of multiple images can be implemented for SDB, thus reducing time spent on identifying optimal images for SDB. Finally, this chapter also highlighted that the $NE\Delta R_{rs}$ can be used to ensure images are fit for purpose for either a single-scene or ensemble SDB.

Given the potential advantages of physics-based SDB (as discussed in chapters 2 and 4), it is increasingly gaining interest among different users. However, issues with uncertainties in depth accuracies - mainly due to AC - still remain, thus prohibiting its full adoption in mainstream bathymetric mapping. Implementing the approach to minimize biases from AC for robust bathymetry estimates as demonstrated in this thesis can further increase interest in the adoption of physics-based SDB by product users such as private companies and hydrographic offices – e.g., the National Oceanic and Atmospheric Administration (NOAA), USA and the Canadian Hydrographic Service (CHS), who have both recently adopted SDB. This will promote the production of regularly updated bathymetric charts, hence facilitating research on nearshore geomorphology, sediment transport, hydrodynamics, and other fields that rely on models of nearshore terrain. Consequently, insights gained from this research can assist the US and Canadian governments, for example, in identifying stable and dynamic seafloor areas along parts of their coast where frequent change in morphology poses a challenge to hydrographers. In the same vein, the CHS will benefit from updating old hydrographic charts in the Arctic, where large parts are currently blank and where maritime transportation is central to people's social and economic activities. At more regional levels, accurate water depth maps can assist in flood management and planning by municipal governments. Such maps may be used to design flood mitigation plans and formulate policies in response to flood safety concerns in cities likely to face future sea-level rise and climate change.

5.2. General conclusion and outlook

This thesis demonstrated that accuracy of SDB estimates derived from physics-based inversion models are highly dependent on the quality of AC. Precise estimates of the R_{rs} produced through application of AC is therefore crucial to reducing errors and uncertainties during the inversion scheme. To this end, a correction method was used to improve SDB accuracy by accounting for known effects of environmental factors in the R_{rs} images. Future studies should consider using the correction approach demonstrated in this study to improve the R_{rs} using more satellite data. Thanks to the 5-day revisit of the Sentinel-2 satellite mission, both Landsat 8 and Sentinel-2 data products offer the potential to support such effort. Likewise, the recent rapid increase in the development of water-based AC algorithms will provide an avenue to obtain per-band correction factors for a given AC algorithm since it can be reasonably assumed that all AC algorithms have some bias. This may improve understanding about sources of errors contributing to retrieval errors, thus guiding further developments of AC algorithms.

Another potential future research focus relates to a correction for adjacency effects, which arise when photons from neighbouring areas are scattered into the path of upwelling radiation detected by the sensor. Adjacency effects can introduce artefacts in the R_{rs} which will lead to error in the inversion and subsequently decrease accuracy of SDB estimates. Such correction, while not considered in this thesis, may further reduce uncertainties in physics-based SDB, especially from lakes, inland waters or coastal waters in close proximity to land. This additional correction will ultimately promote the utility of physics-based SDB for operational usage for shallow water mapping anywhere on Earth.

Statement of contribution

Chapter 1: I wrote this chapter.

Chapter 2: I contributed to the writing of the manuscript and gathering of data, and also provided feedback on the writing of the manuscript.

Chapter 3: I wrote the manuscript and performed majority of the data analysis. Co-authors assisted with supervision; reviewed and provided feedback on the writing of the manuscript.

Chapter 4: I wrote the paper and performed the analysis of data. Co-author assisted with supervision, reviewed and provided feedback on the writing of the paper.

Chapter 5: I wrote this chapter.

Appendix. Supplemental Data for Chapter 3

Supplemental Data 3a.

The root mean squared errors showing the impacts of per-band spectral adjustment on AERONET-OC match-ups. For all AC methods, there is no noticeable effect in the 443 nm channel. Similarly, for the land-based AC methods, there is no observable difference in the 443 and 482 nm channels. Band adjustment improves results for bands 2, 3 and 4 for SeaDAS, decreasing RMSE values by 16.6, 23.9 and 43.8% in the 482, 561 and 655 nm wavelengths, respectively, and also improves results for bands 3 and 4 for ACOLITE by 15.6 and 24.2%, respectively. For SeaDAS, the largest observable difference is in the 655 nm channel. This is by far the largest improvement from band adjustment across all bands and AC methods. Overall, SeaDAS is the most sensitive method to spectral band differences, with the largest difference (improvement) in the 655 nm channel.

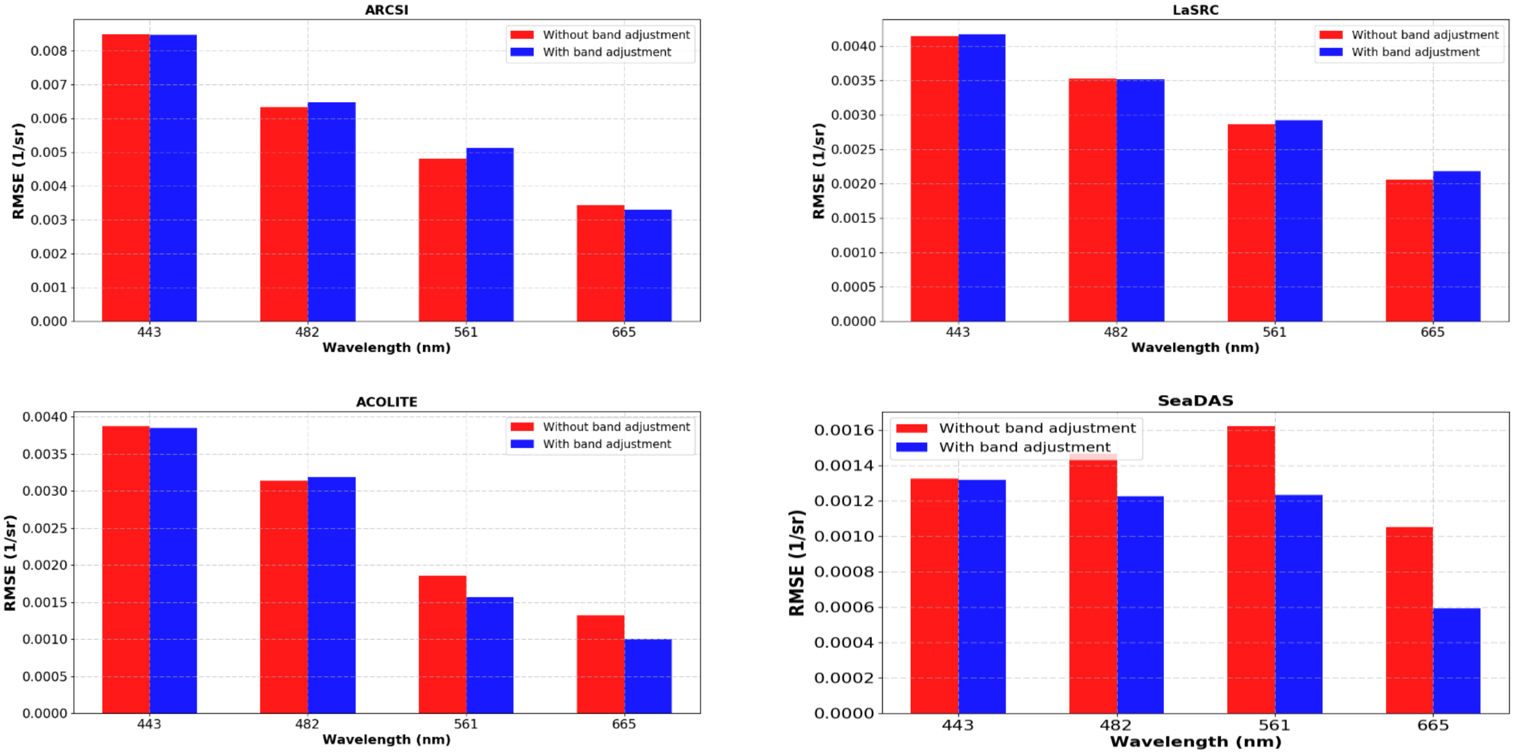

Supplemental Data 3b.

Satellite scenes and their correspondent sites

Landsat Scene ID	Site
['LC81810302014141LGN00'	Galata
['LC81810302014253LGN00'	Galata
['LC81810302015240LGN00'	Galata
['LC81810302015352LGN00'	Galata
['LC81800292014086LGN00'	Gloria
['LC81800292014358LGN00'	Gloria
['LC81800292015041LGN00'	Gloria
['LC81800292015361LGN00'	Gloria
['LC81280542014026LGN00'	GOT_Seaprism
['LC81920192013151LGN00'	Gustav_Dalen_Tower
['LC81880182013235LGN00'	Helsinki_Lighthouse
['LC81880182014190LGN00'	Helsinki_Lighthouse
['LC81880182016180LGN00'	Helsinki_Lighthouse
['LC81880182016228LGN00'	Helsinki_Lighthouse
['LC81880182016260LGN00'	Helsinki_Lighthouse
['LC80200312016219LGN00'	Lake_Erie
['LC80200312016235LGN00'	Lake_Erie
['LC80130322013273LGN00'	LISCO
['LC80130322014004LGN00'	LISCO
['LC80130322015023LGN00'	LISCO
['LC80130322015279LGN00'	LISCO
['LC80130322016266LGN00'	LISCO
['LC80110312013291LGN00'	MVCO
['LC80110312014038LGN00'	MVCO
['LC80110312014150LGN00'	MVCO
['LC80110312015025LGN00'	MVCO
['LC80110312014086LGN00'	MVCO
['LC81950192013156LGN00'	Palgrunden
['LC81950192016165LGN00'	Palgrunden
['LC81990242016129LGN00'	Thornton_C-power
['LC81990242016305LGN00'	Thornton_C-power
['LC80410372014312LGN00'	USC_SEAPRISM
['LC80410372016222LGN00'	USC_SEAPRISM_2
['LC80410372016318LGN00'	USC_SEAPRISM_2
['LC80410372016334LGN00'	USC_SEAPRISM_2
['LC81920292014106LGN00'	Venise
['LC81920292015013LGN00'	Venise
['LC81920292015221LGN00'	Venise
['LC81920292016016LGN00'	Venise
['LC81920292016128LGN00'	Venise

['LC81920292016192LGN00'	Venise
['LC81920292016240LGN00'	Venise
['LC80220402013240LGN00'	WaveCIS_Site_CSI
['LC80220402013320LGN00'	WaveCIS_Site_CSI
['LC80220402014019LGN00'	WaveCIS_Site_CSI
['LC80220402014291LGN00'	WaveCIS_Site_CSI
['LC80220402014323LGN00'	WaveCIS_Site_CSI
['LC80220402015038LGN00'	WaveCIS_Site_CSI
['LC80220402015342LGN00'	WaveCIS_Site_CSI
['LC80220402016009LGN00'	WaveCIS_Site_CSI
['LC80220402016041LGN00'	WaveCIS_Site_CSI
['LC80220402016073LGN00'	WaveCIS_Site_CSI
['LC81990242014091LGN00'	Zeebrugge-MOW1
['LC81990242014219LGN00'	Zeebrugge-MOW1

Supplemental Data 3c.

Values of environmental parameters for each match-up

Station Date	SZA (^{0})	AOT 869 (nm)	Wind Speed (m/s)	Chlorophyll -a (mg/m3)
Galata_2014141	27.68254	0.061308	4.109681	1.15
Galata_2014253	41.58995	0.116449	3.284061	1.10
Galata_2015240	37.50297	0.058537	2.129808	0.73
Galata_2015352	68.64532	0.191727	4.643727	0.62
Gloria_2014086	45.39897	0.039736	1.40709	1.03
Gloria_2014358	69.93295	0.009096	13.20025	2.28
Gloria_2015041	62.24466	0.011158	9.488579	1.64
Gloria_2015361	70.11336	0.01644	8.966497	1.31
Got_2014026	39.26405	0.184762	2.348026	0.81
Gustav_2013151	37.76921	0.045492	7.765895	1.44
Helsinki_2013235	49.6655	0.045049	7.813921	4.11
Helsinki_2014190	38.82244	0.052049	5.058227	5.19
Helsinki_2016180	38.00992	0.036343	3.183139	3.87
Helsinki_2016228	47.29317	0.015965	5.356986	3.00
Helsinki_2016260	58.31484	0.014555	7.385065	3.66
LakeErie_2016219	31.06475	0.036835	4.838009	5.32
LakeErie_2016235	35.04874	0.032271	2.098577	5.84
LISCO_2013273	45.86886	0.02143	6.629846	6.12
LISCO_2014004	65.76056	0.009206	3.691909	3.92
LISCO_2015023	63.25687	0.01911	5.097444	5.36
LISCO_2015279	48.07922	0.025828	6.469751	4.84
LISCO_2016266	43.53788	0.03848	4.592692	4.06
MVCO_2013291	53.30351	0.016554	8.056089	3.24
MVCO_2014038	60.57072	0.025061	6.897844	4.52
MVCO_2014086	43.2755	0.042702	8.934463	4.96
MVCO_2014150	25.55208	0.054678	2.590076	1.50
MVCO_2015025	64.20812	0.036832	10.15678	5.03
Palgrunden_2013156	37.03093	0.01894	3.94127	7.58
Palgrunden_2016165	36.71529	0.013707	0.5948	6.87
Thornton_2016129	36.60009	0.070453	7.756932	16.3
Thornton_2016305	66.8652	0.058625	2.756128	3.24
USCSeaPrism_2014312	52.58024	0.028872	4.974118	0.22
USCSeaPrism_2016222	37.88999	0.074677	3.123159	0.63
USCSeaPrism_2016318	54.05641	0.027335	3.450807	0.30
USCSeaPrism_2016334	57.61152	0.026866	3.217656	0.61
Venise_2014106	37.88999	0.023221	6.324373	3.41
Venise_2015013	68.62708	0.039125	3.700884	1.19
Venise_2015221	33.40939	0.125445	3.092528	0.78

Venise_2016016	68.39465	0.011226	6.740557	0.58
Venise_2016128	31.50274	0.03962	1.123216	1.01
Venise_2016192	27.88954	0.085338	1.76539	1.59
Venise_2016240	38.46594	0.033166	1.342931	1.87
WaveCIS_2013240	28.31299	0.080524	3.036319	2.15
WaveCIS_2013320	50.72926	0.069036	6.575934	2.20
WaveCIS_2014019	54.4896	0.03491	7.112117	3.99
WaveCIS_2014291	42.45005	0.016669	3.183118	1.55
WaveCIS_2014323	51.5107	0.016451	2.907233	1.53
WaveCIS_2015038	50.60994	0.022994	2.271182	1.80
WaveCIS_2015342	55.17512	0.033926	1.131623	3.37
WaveCIS_2016009	56.01941	0.072489	4.151914	3.19
WaveCIS_2016041	49.98228	0.008506	5.38026	3.97
WaveCIS_2016073	39.38958	0.052527	5.027627	2.76
Zeebruge_2014091	49.09826	0.093231	2.259445	3.42
Zeebruge_2014219	37.90776	0.13111	3.071374	4.11

Supplemental Data 3d.

Line graphs showing the R_{rs} spectra of each of the 14 AERONET-OC stations (Results were averaged for each station except GOT Seaprism for which only one match-up is available)

.

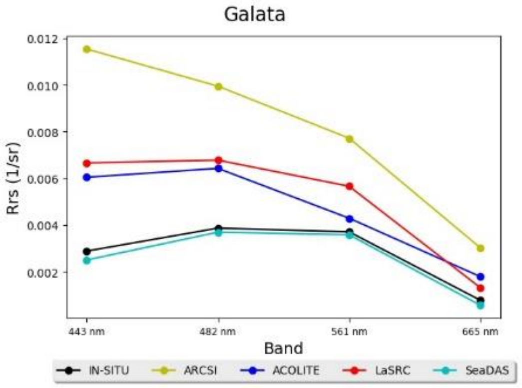

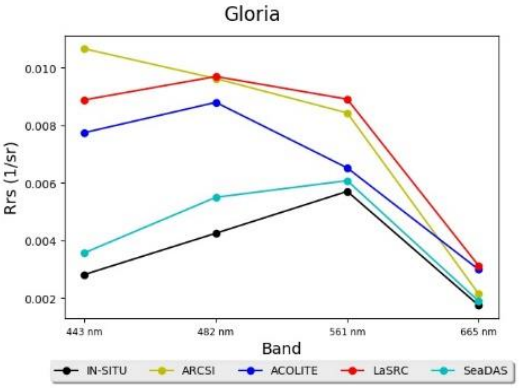

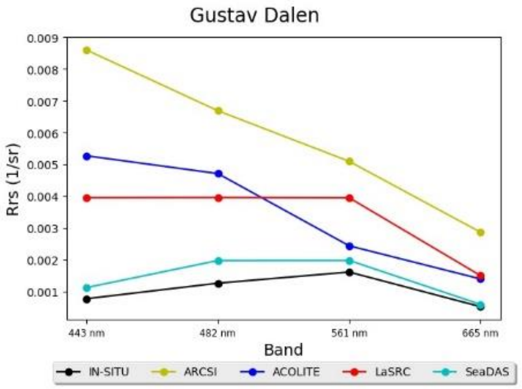

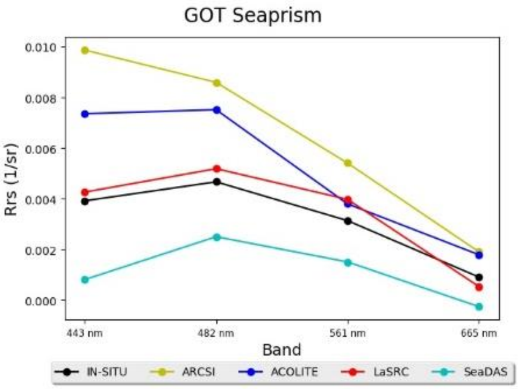

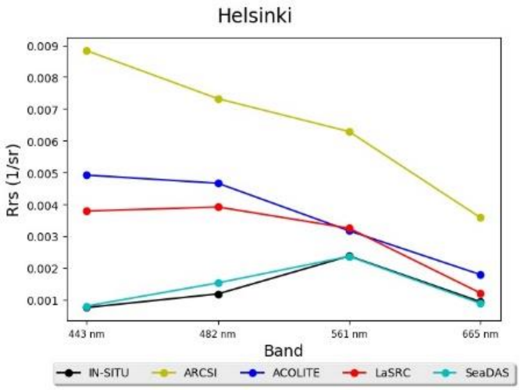

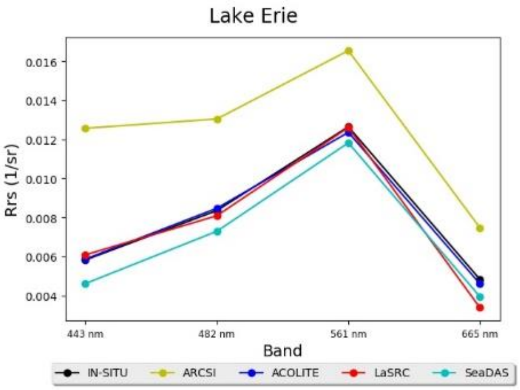

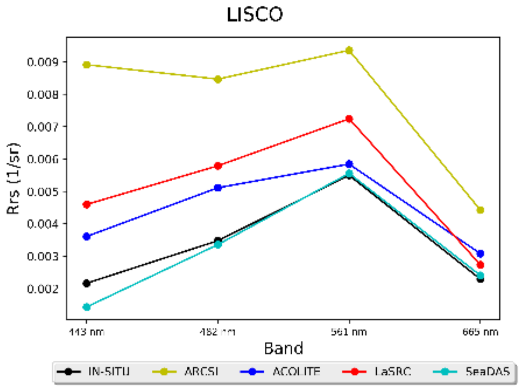
LISCO
Rrs (1/sr)
0.009
0.008
0.007
0.006
0.005
0.004
0.003
0.002
443 nm
482 nm
561 nm
665 nm
Band
IN-SITU
ARCSI
ACOLITE
LaSRC
SeaDAS

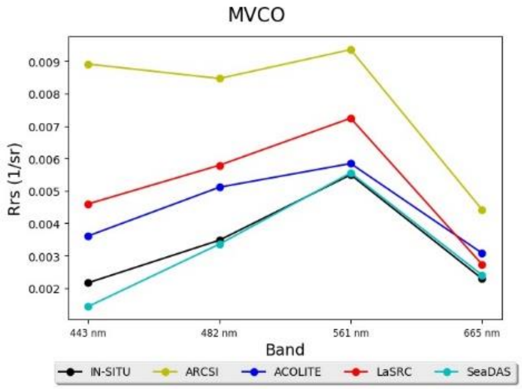
MVCO
Rrs (1/sr)
0.009
0.008
0.007
0.006
0.005
0.004
0.003
0.002
443 nm
482 nm
561 nm
665 nm
Band
IN-SITU
ARCSI
ACOLITE
LaSRC
SeaDAS

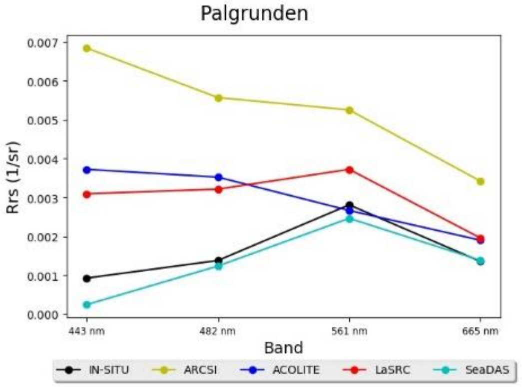
Palgrunden
Rrs (1/sr)
0.007
0.006
0.005
0.004
0.003
0.002
0.001
0.000
443 nm
482 nm
561 nm
665 nm
Band
IN-SITU
ARCSI
ACOLITE
LaSRC
SeaDAS

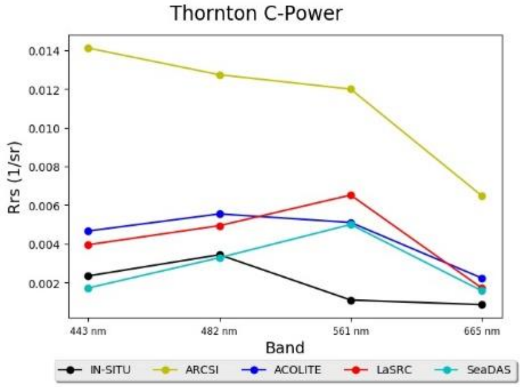
Thornton C-Power
Rrs (1/sr)
0.014
0.012
0.010
0.008
0.006
0.004
0.002
443 nm
482 nm
561 nm
665 nm
Band
IN-SITU
ARCSI
ACOLITE
LaSRC
SeaDAS

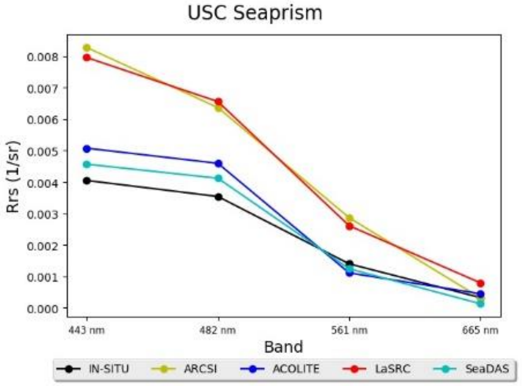
USC Seaprism
Rrs (1/sr)
0.008
0.007
0.006
0.005
0.004
0.003
0.002
0.001
0.000
443 nm
482 nm
561 nm
665 nm
Band
IN-SITU
ARCSI
ACOLITE
LaSRC
SeaDAS

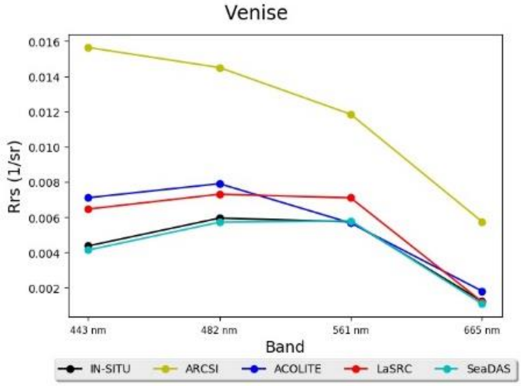
Venise
Rrs (1/sr)
0.016
0.014
0.012
0.010
0.008
0.006
0.004
0.002
443 nm
482 nm
561 nm
665 nm
Band
IN-SITU
ARCSI
ACOLITE
LaSRC
SeaDAS

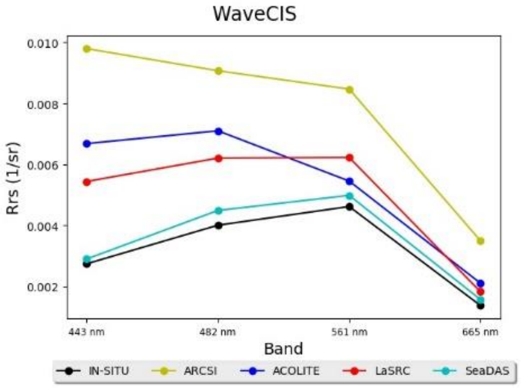
WaveCIS
Rrs (1/sr)
0.010
0.008
0.006
0.004
0.002
443 nm
482 nm
561 nm
665 nm
Band
IN-SITU
ARCSI
ACOLITE
LaSRC
SeaDAS

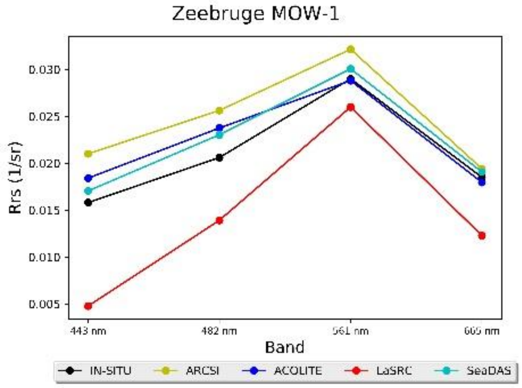
Zeebruge MOW-1
Rrs (1/sr)
0.030
0.025
0.020
0.015
0.010
0.005
443 nm
482 nm
561 nm
665 nm
Band
IN-SITU
ARCSI
ACOLITE
LaSRC
SeaDAS

Supplemental Data 3e.

Cases of negative R_{rs} retrievals from the four AC algorithms

ACOLITE		LaSRC		SeaDAS	
561 nm	USC Seaprism: 2016222	443 nm	WaveCIS: 2013320	443nm	Palgrunden: 2013156
655 nm	Gloria: 2014358 USC Seaprism: 2016222	655 nm	WaveCIS: 2013320 MVCO: 2014150	655nm	GOT Seaprism: 2014026 USC Seaprism: 2016222 Venise: 2015221